Advances in time–domain induced polarisation tomography

Data acquisition, processing and modelling

Olsson, Per-Ivar

2018

Document Version:
Publisher's PDF, also known as Version of record

Link to publication

Citation for published version (APA):
Olsson, P.-I. (2018). *Advances in time–domain induced polarisation tomography: Data acquisition, processing and modelling*. [Doctoral Thesis (compilation), Faculty of Engineering, LTH]. Department of Biomedical Engineering, Lund university.

Total number of authors:
1

LUND UNIVERSITY

PO Box 117
221 00 Lund
+46 46-222 00 00

Advances in time-domain induced polarisation tomography

Data acquisition, processing and modelling

PER-IVAR OLSSON

ENGINEERING GEOLOGY | FACULTY OF ENGINEERING | LUND UNIVERSITY

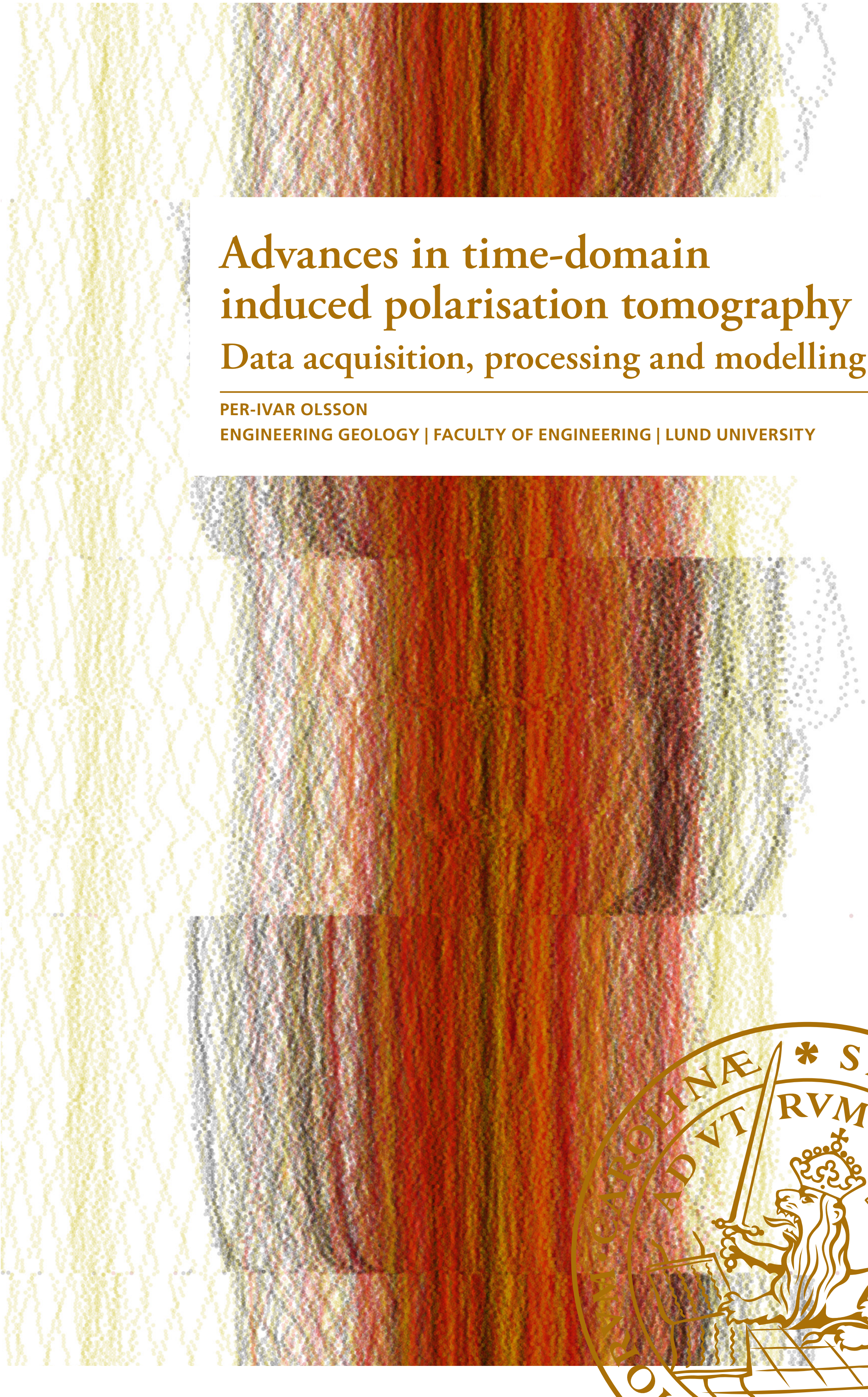

Advances in time–domain induced polarisation tomography

Advances in time–domain induced polarisation tomography

Data acquisition, processing and modelling

Per–Ivar Olsson

DOCTORAL DISSERTATION
by due permission of the Faculty of Engineering, Lund University, Sweden.
To be defended at V–huset, John Ericssons väg 1, Lund, Sweden, Lecture hall V:B,
on November 30, 2018 at 10:15 a.m.

Lund University Faculty opponent
Prof. Myriam Schmutz, Institut Polytechnique de Bordeaux ENSEGID, France

Organisation: LUND UNIVERSITY

Faculty of Engineering

Author: Per–Ivar Olsson

Document name: Doctoral dissertation

Date of issue: 2018-10-23

Sponsoring organisation: –

Advances in time–domain induced polarisation tomography: data acquisition, processing and modelling

What would you find below your feet – how do you find out? Perhaps you could look at a geological map, drill, or dig? That could work, but sometimes the maps are not detailed enough, and digging everywhere to find out is impractical. Imagine if you could develop a method that allows you to see straight through the ground, as x–rays through the body! To some extent, such methods already exist; you can for example send electric current into the ground that tells you what lies beneath when it returns. The current does not see the subsurface as we do–no soil, boulders, water or bedrock – but it can tell us about its view of the underground. Its image is in terms of electrical resistivity and chargeability and can be difficult to understand if it is not translated. The translation is accomplished by comparing the electric image with, for example, geological maps and information from boreholes. With this method, we obtain more reliable and more detailed models of the subsurface. Additionally, electrical surveys can help us to determine where we need more subsurface information and where it would be most interesting to drill or dig.

When we plan and build structures below or above ground, search for suitable places for wells, or remediate contaminated areas, we need good and reliable information about the ground below. Incorrect or incomplete information about the subsurface can lead to unexpected problems. These problems can in turn lead to delays and reduced sustainability in the implementations. One example of such a project is the train tunnel through Hallandsåsen in Southern Sweden, which suffered several delays and took 23 years to complete, and its final price tag was approximately ten times the initial estimate.

This thesis addresses how we can develop and improve the use of electrical current to investigate the subsurface. The method has been used and developed for more than one hundred years, but bottlenecks remain that limit its use. One example is in cities where electrical installations and a complex environment in the subsurface distort the current. We then need to filter the image to make use of the results from the measurements. The method may also be limited by lack of resources needed to conduct the investigations, or to make proper interpretations of its information. By refining and optimising the method, its usefulness can be increased. For example, by enabling its use in urban areas or for projects with limited resources.

This thesis describes how we can process signals from electrical surveys and handle interference from other electrical installations, similar to a pair of noise–cancelling headphones. The processing allows us to retrieve more information about the subsurface and increase the reliability of the results. Another improvement that is introduced is a change of the shape of the current that is sent into the ground. The change of waveform results in a reduction in the time required for a survey, while the magnitude of the signals is increased, similar to completing a podcast in half of the time with better audio quality.

Another way to improve the method is to increase our understanding of what types of responses we can expect from the measurements. This thesis describes how measurement results that were previously considered erroneous can be explained, and that these are actually physically possible. By not rejecting such results, we can obtain more information from the measurements, more reliable models of the subsurface, and post–processing of the measurements is simplified. In addition, it describes how we can compensate for the effects of varying duration of current transmissions. If the effects are not considered properly, different electrical images of the same subsurface are obtained depending on whether the current is sent just one second longer or shorter.

The optimisations of the thesis are exemplified with, among others, results from a major survey that mapped a geologic site in terms of resistance and chargeability down to 200 metres below ground. Such information is important and can help us to take better decisions, for example in connection with infrastructure projects for a more sustainable future. Hopefully, the work in this thesis can increase the use of electrical surveys, ensuring we can make more informed decisions in the future.

Key words: Tomography; Electrical properties; Induced polarisation; Duty–Cycle; Waveform; Signal–to–noise ratio

Classification system and/or index terms (if any): –

Supplementary bibliographical information: –

Language: English

ISSN and key title: –

ISBN: 978–91–7753–850–9

Recipient's notes

Number of pages: 167

Price: Free

Security classification: –

I, the undersigned, being the copyright owner of the abstract of the above–mentioned dissertation, hereby grant to all reference sources permission to publish and disseminate the abstract of the above–mentioned dissertation.

Signature ______________________ Date: 2018-10-18

Advances in time–domain induced polarisation tomography

Data acquisition, processing and modelling

Per–Ivar Olsson

LUND
UNIVERSITY

Cover images by Per–Ivar Olsson

Faculty of Engineering
Department of Engineering Geology

ISBN (print) 978–91–7753–850–9
ISBN (pdf) 978–91–7753–851–6
ISRN LUTVDG/(TVTG–1041)/1–167/(2018)

Printed in Sweden by Media–Tryck, Lund University
Lund 2018

MADE IN SWEDEN

Media-Tryck is an environmentally
certified and ISO 14001 certified
provider of printed material.
Read more about our environmental
work at www.mediatryck.lu.se

Preface

The work presented in this thesis has been carried out at the Division of Engineering Geology, Lund University in Sweden, and in part at the Hydrogeophysics group, Department of Geoscience at Aarhus University in Denmark. It is a continuation on my licentiate thesis (Olsson, 2016), thus parts of the content represent a reappearance of the work presented therein.

Funding for the work presented in this thesis was provided by Formas – The Swedish Research Council for Environment, Agricultural Sciences and Spatial Planning, (ref. 2012–1931), BeFo – Swedish Rock Engineering Research Foundation, (ref. 331) and SBUF – The Development Fund of the Swedish Construction Industry, (ref. 12719). The project is part of the Geoinfra–TRUST framework (http://www.trust–geoinfra.se/). Additional funding for collaboration with Aarhus University was provided by Hakon Hansson foundation (ref. HH2015–0074) and Ernhold Lundström foundation. Furthermore, the work was partly funded by the European Union, Eurostars Programme, together with Innovation Fund Denmark and The Swedish innovation agency Vinnova under the project "Mapping Geology in Cities" (E10096 MAGIC).

This thesis was made possible with the assistance and inspiration of several people and I would like to express my gratitude to one and all who supported me in the work. I am unable to mention everyone in this preface but my main supervisor Torleif Dahlin as well as my assisting supervisors Gianluca Fiandaca and Esben Auken, deserve special thanks for their excellent support, help and guidance throughout the work.

However, I also want to express my gratitude to my past and present colleagues at the Division of Engineering Geology at Lund University who have been supportive with good spirits in and outside of work and for their fruitful discussions. Finally, I want to thank my friends and family for supporting me and giving me the opportunity to conduct the work presented herein.

Per–Ivar Olsson

Malmö, August 2018

Table of Contents

Summary 13

Sammanfattning 15

Appended publications 17

Related publications 19

Nomenclature 21

1. Introduction 23
    1.1. Aims 24
    1.2. Limitations 25

2. The DCIP methodology 27
    2.1. Resistivity 28
    2.2. Chargeability 28
    2.3. Waveforms 30
        2.3.1. Time–domain 31
        2.3.2. Frequency–domain 32
    2.4. Sensitivity 33
    2.5. Inversion 33

3. Results and discussion 35
    3.1. Data quality and reliability 35
        3.1.1. Background drift 36
        3.1.2. Spikes 38
        3.1.3. Harmonic noise 39
        3.1.4. Electromagnetic coupling 40
        3.1.5. Bottleneck reduction 41
    3.2. Acquisition time 42
        3.2.1. Waveform time 43
        3.2.2. Sequence time 43
        3.2.3. Bottleneck reduction 44

3.3. Data post–processing....45
  3.3.1. Bottleneck reduction....46
3.4. DCIP survey example....47
4. Conclusions....49
5. Future research....51
5.1. Data quality and reliability....51
  5.1.1. Anthropogenic DC noise....51
  5.1.2. Electromagnetic coupling....51
  5.1.3. Data reliability at acquisition....52
5.2. Survey time....52
  5.2.1. Hardware....52
  5.2.2. Dynamic waveform and protocol....52
5.3. Data post–processing....53
  5.3.1. Automated data processing....53
6. References....55

Summary

What would you find below your feet – how do you find out? Perhaps you could look at a geological map, drill, or dig? That could work, but sometimes the maps are not detailed enough, and digging everywhere to find out is impractical. Imagine if you could develop a method that allows you to see straight through the ground, as x–rays through the body! To some extent, such methods already exist; you can for example send electric current into the ground that tells you what lies beneath when it returns. The current does not see the subsurface as we do – no soil, boulders, water or bedrock – but it can tell us about its view of the underground. Its image is in terms of electrical resistivity and chargeability and can be difficult to understand if it is not translated. The translation is accomplished by comparing the electric image with, for example, geological maps and information from boreholes. With this method, we obtain more reliable and more detailed models of the subsurface. Additionally, electrical surveys can help us to determine where we need more subsurface information and where it would be most interesting to drill or dig.

When we plan and build structures below or above ground, search for suitable places for wells, or remediate contaminated areas, we need good and reliable information about the ground below. Incorrect or incomplete information about the subsurface can lead to unexpected problems. These problems can in turn lead to delays and reduced sustainability in the implementations. One example of such a project is the train tunnel through Hallandsåsen in Southern Sweden, which suffered several delays and took 23 years to complete, and its final price tag was approximately ten times the initial estimate.

This thesis addresses how we can develop and improve the use of electrical current to investigate the subsurface. The method has been used and developed for more than one hundred years, but bottlenecks remain that limit its use. One example is in cities where electrical installations and a complex environment in the subsurface distort the current. We then need to filter the image to make use of the results from the measurements. The method may also be limited by lack of resources needed to conduct the investigations, or to make proper interpretations of its information. By refining and optimising the method, its usefulness can be increased. For example, by enabling its use in urban areas or for projects with limited resources.

This thesis describes how we can process signals from electrical surveys and handle interference from other electrical installations, similar to a pair of noise–cancelling headphones. The processing allows us to retrieve more information about the subsurface and increase the reliability of the results. Another improvement that is introduced is a change of the shape of the current that is sent into the ground. The change of waveform results in a reduction in the time required for a survey, while the magnitude of the signals is increased, similar to completing a podcast in half of the time with better audio quality.

Another way to improve the method is to increase our understanding of what types of responses we can expect from the measurements. This thesis describes how measurement results that were previously considered erroneous can be explained, and that these are actually physically possible. By not rejecting such results, we can obtain more information from the measurements, more reliable models of the subsurface, and post–processing of the measurements is simplified. In addition, it describes how we can compensate for the effects of varying duration of current transmissions. If the effects are not considered properly, different electrical images of the same subsurface are obtained depending on whether the current is sent just one second longer or shorter.

The optimisations of the thesis are exemplified with, among others, results from a major survey that mapped a geologic site in terms of resistance and chargeability down to 200 metres below ground. Such information is important and can help us to take better decisions, for example in connection with infrastructure projects for a more sustainable future. Hopefully, the work in this thesis can increase the use of electrical surveys, ensuring we can make more informed decisions in the future.

Sammanfattning

Vad står vi på – hur tar man reda på det? Kanske man kan titta på en geologisk karta, borra ett hål eller gräva en grop? Det kan gå bra, men ibland finns det inte tillräckligt detaljerade kartor och att gräva upp allt man är intresserad av är ingen lysande idé. Tänk om man kunde forska fram en metod som gör att man kan se rakt igenom marken, som röntgenundersökningar på sjukhus! På sätt och vis kan man redan det, man kan skicka ner ström i marken som berättar om hur där ser ut när den kommer tillbaka. Ström ser inte marken som vi gör – ingen jord, sten, vatten eller berg men den kan berätta för oss om dess bild av marken. Bilden är i termer av motstånd och uppladdning och kan vara svår att förstå om den inte översätts. Översättningen görs genom att jämföra den elektriska bilden med till exempel geologiska kartor och information från borrhål. Med denna metod får vi totalt sett en säkrare och mer detaljerad modell av marken. De elektriska undersökningarna kan också hjälpa oss att avgöra var vi behöver mer information och var det kan vara som mest intressant att borra eller gräva.

När vi ska planera och bygga konstruktioner ovan eller under mark, hitta lämpliga platser för brunnar eller sanera förorenade områden behöver vi ha bra och säker information om vad marken består av. Felaktig eller ofullständig information om marken kan skapa oväntade problem. Dessa kan i sin tur leda till förseningar och minskad hållbarhet i genomförandet. Ett exempel är tågtunneln genom Hallandsåsen i Skåne som tog 23 år att färdigställa och blev cirka tio gånger dyrare att bygga än vad som först beräknats med en slutnota på över tio miljarder kronor.

Denna avhandling handlar om hur vi kan utveckla och förbättra användningen av ström för att undersöka marken. Metoden har använts och utvecklats sedan förra sekelskiftet men det finns fortfarande flaskhalsar som begränsar dess användning. Ett exempel är i städer där elinstallationer och en rörig miljö i marken förvirrar strömmen. Vi behöver då filtrera dess bild av marken för att kunna utnyttja mätresultaten. Användningen av metoden kan också begränsas av brist på resurser för att utföra undersökningarna eller för göra ordentliga tolkningar av informationen. Genom att förfina och effektivisera metoden kan den alltså vara till större nytta på fler platser och användas för att få information om marken med mer begränsade resurser.

I avhandlingen beskrivs hur man kan filtrera signaler från elektriska markundersökningar och hantera störningar från andra elinstallationer, ungefär som att sätta på den ett par brusreducerande hörlurar. Filtreringen gör att vi kan få ut mer information om marken och ett mer pålitligt mätresultat. En annan förbättring som har utvecklats är att förändra formen på strömmen som skickas ner i marken. Formändringen gör att tiden som krävs för en undersökning halveras samtidigt som man får dubbelt så stark signal, som att lyssna igenom en podcast på halva tiden med bättre ljudkvalitet.

Ett annat sätt att förbättra undersökningarna är att öka vår förståelse för vad strömmen berättar om marken. Avhandlingen beskriver hur mätresultat som tidigare betraktats som felaktiga kan uppkomma och att dessa faktiskt är fysiskt möjliga. Genom att inte förkasta dessa resultat kan vi få ut mer information från mätningarna och säkrare modeller av marken samtidigt som översättningen av mätresultat kan bli enklare. Dessutom beskrivs hur vi kan kompensera för effekter av hur länge strömmen sänds ner i marken. Om effekterna inte hanteras får man olika elektriska bilder av samma mark beroende på om man skickar ström någon sekund längre eller kortare.

Avhandlingens förbättringar och effektiviseringar visas bland annat med resultat från en större undersökning som kartlägger geologi i termer av motstånd och uppladdning ned till 200 meter under markytan. Sådan information är viktig och kan underlätta att ta bättre beslut, till exempel i samband med infrastrukturprojekt, för en mer hållbar framtid. Förhoppningsvis kan avhandlingen öka användandet av elektriska markundersökningar så att vi kan ta mer informerade beslut i framtiden.

Appended publications

The thesis is based on the following appended publications.

Paper I

Olsson, P.–I., Dahlin, T., Fiandaca, G., Auken, E., 2015. Measuring time–domain spectral induced polarization in the on–time: decreasing acquisition time and increasing signal–to–noise ratio. J. Appl. Geophys. 123, 316–321. https://doi.org/10.1016/j.jappgeo.2015.08.009

Paper II

Olsson, P.–I., Fiandaca, G., Larsen, J.J., Dahlin, T., Auken, E., 2016. Doubling the spectrum of time–domain induced polarization by harmonic de–noising, drift correction, spike removal, tapered gating and data uncertainty estimation. Geophys. J. Int. 207, 774–784. https://doi.org/10.1093/gji/ggw260

Paper III

Fiandaca, G., Olsson, P.–I., Maurya, P.K., Dahlin, T., Auken, E., 2018. Non–standard responses in time–domain induced polarization measurements. Geophys. J. Int. (in review)

Paper IV

Olsson, P.–I., Fiandaca, G., Maurya, P.K., Auken, E., Dahlin, T., 2018. Effect of current pulse duration in recovering unbiased, quantitative induced polarization models from time–domain full–response and integral chargeability data. Geophys. J. Int. (in review)

Paper V

Rossi, M., Olsson, P.–I., Johansson, S., Fiandaca, G., Preis Bergdahl, D., Dahlin, T., 2017. Mapping geological structures in bedrock via large–scale direct current resistivity and time–domain induced polarization tomography. Near Surf. Geophys. 15, 657–667. https://doi.org/10.3997/1873–0604.2017058

Publication contributions

The thesis author has conducted the acquisition of all field data used in the papers, in parts or fully, except for paper III. As the main author of papers I, II and IV, he has been leading the writing process. For paper III he wrote the original draft, introduced the IP response classification system and has been leading the writing of the paper except for the "Basic mechanism and synthetic modelling" section. Furthermore, he developed the major parts of the processing schemes for paper I and II as well as necessary visualisation tools for paper III. For paper V, he planned and conducted data acquisition, and critically revised text and figures of a first version of the paper. The thesis author has not contributed to the development of the relevant inversion software.

Related publications

Dahlin, T., Johansson, S., Olsson, P.–I., Rossi, M., Ronczka, M., 2017. DCIP tomografi för kartläggning av jorddjup och strukturer i berg, in: Bergmekanikdagen 2017. Stockholm, Sweden, pp. 1–10.

Johansson, S., Olsson, P.–I., Lumetzberger, M., Dahlin, T., Rosqvist, H., Sparrenbom, C., 2014. Delineation of a free phase chlorinated hydrocarbon plume with resistivity and TDIP, in: Proceedings of the 3rd International Workshop on Induced Polarization, 6 – 9 April 2014. Ile d'Oléron, France.

Johansson, S., Sparrenbom, C., Fiandaca, G., Lindskog, A., Olsson, P.–I., Dahlin, T., Rosqvist, H., 2017. Investigations of a Cretaceous limestone with spectral induced polarization and scanning electron microscopy. Geophys. J. Int. 208, 954–972. https://doi.org/10.1093/gji/ggw432

Olsson, P.–I., 2016. Optimization of time domain induced polarization data acquisition and spectral information content, (Licentiate Thesis). Lund University, Lund, ISBN: 9789176236727.

Olsson, P.–I., Dahlin, T., Auken, E., Fiandaca, G., 2014. Optimizing the acquisition time for time domain spectral IP by measuring during the on–time, in: Proceedings of the 3rd International Workshop on Induced Polarization, 6 – 9 April 2014. Ile d'Oléron, France, pp. 70–71.

Olsson, P.–I., Dahlin, T., Fiandaca, G., Auken, E., 2014. Measuring Time Domain Spectral IP in the On–time – Decreasing Acquisition Time and Increasing Signal–to–noise Ratio, in: Near Surface Geoscience 2014 – 20th European Meeting of Environmental and Engineering Geophysics. https://doi.org/10.3997/2214–4609.20142058

Olsson, P.–I., Jonsson, P., Johansson, S., Johansson, L., 2017. BeFo 382 – Detailed Comparison Study of 3D–characterized Rock Mass and Geophysical Models, in: Near Surface Geoscience 2017 – 23rd European Meeting of Environmental and Engineering Geophysics. Malmö, Sweden. https://doi.org/10.3997/2214–4609.201702005

Olsson, P.–I., Fiandaca, G., Dahlin, T., Auken, E., 2015. Impact of Time–domain IP Pulse Length on Measured Data and Inverted Models, in: Near Surface Geoscience 2015 – 21st European Meeting of Environmental and Engineering Geophysics. https://doi.org/10.3997/2214–4609.201413755

Olsson, P.–I., Fiandaca, G., Larsen, J.J., Dahlin, T., Auken, E., Olsson, P.–I., Auken, E., Larsen, J.J., Maurya, P.K., Dahlin, T., 2016. Doubling the Spectrum of Time–Domain Induced Polarization: Removal of Harmonic Noise and Self–Potential Drift, in:

Proceedings of the 4th International Workshop on Induced Polarization. Aarhus, Denmark, pp. 1–4.

Rossi, M., Dahlin, T., Olsson, P.–I., Günther, T., 2018. Data acquisition, processing and filtering for reliable 3D resistivity and time–domain induced polarisation tomography in an urban area: field example of Vinsta, Stockholm. Near Surf. Geophys. 220–229. https://doi.org/10.3997/1873–0604.2018014

Nomenclature

Symbols and units

ρ – Resistivity	(Ωm)
ρ_a – Apparent Resistivity	(Ωm)
m_0 – Chargeability	(mV/V)
m_{int} – Integral chargeability	(mV/V)
φ_{max} – MPA phase angle	(mrad)
τ – Cole–Cole relaxation time	(s)
τ_{peak} – MPA peak relaxation time	(s)
c – Cole–Cole frequency exponent	(–)

Abbreviations

DC – Direct Current

CPA – Constant phase angle

DCIP – Direct Current resistivity time–domain and Induced Polarisation

EM – Electromagnetic

FD – Frequency–domain

IP – Induced Polarisation

MPA – Maximum phase angle

Rx – Receiver

SNR – Signal–to–Noise Ratio

Tx – Transmitter

TD – Time–domain

1. Introduction

The need for detailed information of the subsurface is increasing, owing to city expansion, infill projects, subsurface construction (such as tunnelling), and environmental projects (such as contaminant remediation). One common method for acquiring this geo–information is the direct current resistivity and time–domain induced polarisation (DCIP) method, which measures the electrical resistivity and chargeability of the subsurface (Dahlin, 2001; Loke et al., 2013). This thesis summarises selected work on developing and increasing the usefulness of the DCIP method by reducing bottlenecks and focusing on the induced polarisation part.

Electrical resistivity tomography (ERT) has been successfully used in a wide range of subsurface applications (Loke et al., 2013) such as environmental and engineering (Auken et al., 2014; Dahlin et al., 1999), hydrogeological (Auken et al., 2006; Fetter, 2001; Leroux and Dahlin, 2005) and archaeological (Argote–Espino et al., 2013; Florsch et al., 2011) projects. However, different subsurface materials can have the same resistivity (Glover, 2015); thus, it is not possible to differentiate them when only using the resistivity information. This makes induced polarisation information especially valuable, because it can be measured simultaneously with the resistivity with little or no extra effort, and materials can have the same value for resistivity but different values of chargeability. Hence, having two parameters reduces the ambiguity when relating the DCIP measurements to processes and geology. This reduction in ambiguity has been demonstrated in several applications, such as landfill mapping (Dahlin et al., 2010; Leroux et al., 2007), lithology mapping (Kemna et al., 2004; Slater and Lesmes, 2002) and microbial activities (Slater et al., 2008),

The induced polarisation phenomenon can be further evaluated by considering its spectral information, meaning its frequency dependency. Frequency dependency is described with different models and, depending on the choice of model, additional parameters can be retrieved from the chargeability measurements to further reduce any potential ambiguity. The use of spectral IP information in engineering applications is still limited, but there are several examples of research studies where the spectral information has proven useful. For example for aquifer characterisation (Fiandaca et al., 2018; Maurya et al., 2018a; Revil et al., 2015; Slater and Glaser, 2003), mapping geochemical changes (Doetsch et al., 2015a), permafrost monitoring (Doetsch et al., 2015b) and landfill mapping (Gazoty et al., 2013, 2012b, 2012a; Maurya et al., 2017). Additionally, the use of spectral IP information in data interpretation has been shown to reduce resistivity equivalences of subsurface models (Madsen et al., 2018).

Even if different levels of chargeability information generally can be retrieved from DCIP surveys, only the resistivity parameters are often evaluated in applied engineering investigations. This has several explanations, for example: older instruments with limited capability of successfully measuring the chargeability are still in use, and knowledge of how to interpret the chargeability information could be lacking.

Another important factor is related to data quality and reliability. Because the induced polarisation measurements have much lower signal–to–noise ratios compared to the resistivity measurements, the data quality can be poor. Hence, using the data would require more time for manual filtering of the chargeability data and require more resources to make use of it. This calls for an assessment on how to improve the general quality of the acquired induced polarisation data, and for developing automated ways of data quality assessment and data filtering. This is especially the case for urban three–dimensional (3D) surveys with larger amounts of data and higher noise levels.

Spectral evaluation demands a wide time–range of chargeability information (from one millisecond to several seconds) and even higher data quality than the regular "one parameter evaluation". Furthermore, knowledge of whether IP responses are to be considered correct or erroneous is lacking. Hence, increased knowledge regarding physically possible IP responses and smart processing of the DCIP data is needed to facilitate more widespread use of the spectral IP method.

Resource efficiency (in terms of time and costs) for spectral DCIP measurements also limits the usefulness of the method. Field measurements can require several thousands of readings, where more data stacking and longer current transmission pulses may be required compared to regular DCIP acquisition. Thus, there is a need for optimising the measurement and post–processing procedures to reduce the bottlenecks that limit the usefulness of the DCIP method.

1.1. Aims

The aim of this study is to increase the usefulness of the DCIP method by developing the data acquisition and data post–processing methodologies, for reducing the usability bottlenecks that limit adoption of the method.

Therefore, the objectives of this study are to reduce field acquisition time and costs, increase the (spectral) data information content, reliability and quality, and reduce the time and costs related to post–processing of data.

1.2. Limitations

There are numerous ways to increase the usefulness of the DCIP method, and some of these are not included in the scope of the work presented in this thesis. This work has not considered any combination with other field surveying or geophysical methods, and only considers the direct current resistivity and time–domain induced polarisation method. This is performed primarily with its pre–existing hardware. Additionally, the handling of electromagnetic coupling has not been considered as a part of this work, except for applying an improved field procedure (Dahlin and Leroux, 2012).

Furthermore, the work has focused on developing the time–domain measurement technique rather than its frequency–domain counterpart.

2. The DCIP methodology

DCIP measurements (Figure 1) are typically carried out by injecting current into the subsurface between two electrodes while measuring the potential between one or several other pairs of electrodes (Fink, 1990; Sumner, 1976; Zonge et al., 2005). The aim of the measurements is to acquire information regarding the electrical resistivity and chargeability of the subsurface. Information from different sub volumes of the subsurface is retrieved by repeating the measurements with different electrode combinations. With electrode combinations arranged along a line, one– or two–dimensional information of the subsurface below the line can be retrieved, depending on what combinations are used. Further, if the electrodes cover a surface area, it is possible to map the electrical properties of a 3D volume (Loke and Barker, 1996).

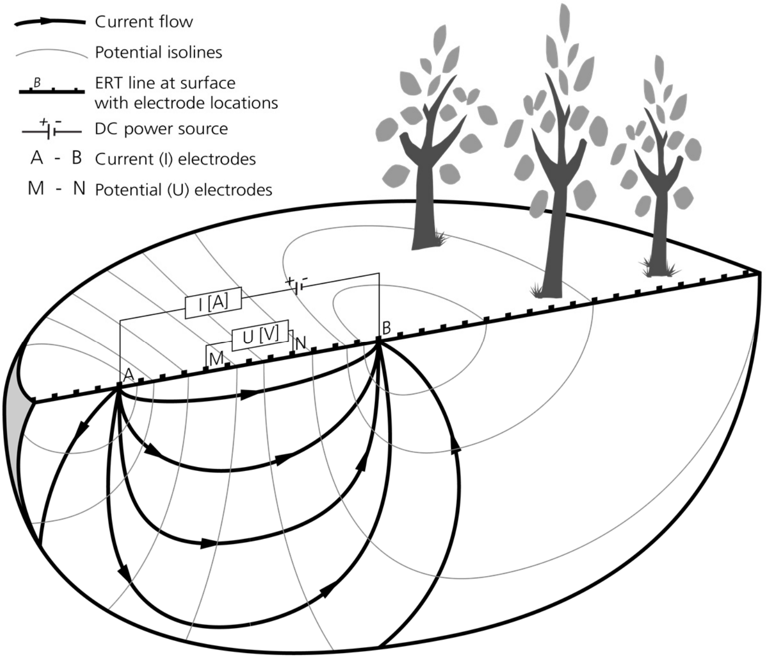

Figure 1. Schematic overview of the DCIP measurement principle for data acquisition along a line on a homogenous subsurface. In the figure, only one pair of potential electrodes (M and N) is indicated, while it is possible to sample the potential surface with multiple potential electrode pairs at the same time. Figure adapted from the original provided by Nijland et al. (2010).

2.1. Resistivity

Resistivity (ρ, unit Ωm) is a material property that quantifies to what extent a material is opposing the flow of electrical current.

From the measurements of the current (*I*) and potential (V_{DC}) (Figure 2), it is possible to calculate the resistance (*R*) of the subsurface using Ohm's law as follows:

$$R = \frac{V_{DC}}{I}$$

By also taking into account the geometry of the electrode placements (geometric factor, *K*), the apparent resistivity (ρ_a) can be retrieved (which only corresponds to the true resistivity of the subsurface if it is homogenous and isotropic) as follows:

$$\rho_a = K\frac{V_{DC}}{I}$$

where

$$K = 2\pi(r_{AM}^{-1} - r_{BM}^{-1} - r_{AN}^{-1} + r_{BN}^{-1})^{-1}$$

and *r* denotes the different distances between current (*A* and *B*) and potential (*M* and *N*) electrodes. If the subsurface has a heterogeneous distribution of resistivity, it is necessary to conduct a more advanced interpretation of the measurements to retrieve the resistivity of the subsurface (see 2.5 Inversion).

2.2. Chargeability

The chargeability (m_0, unit mV/V) is a material property that quantifies the capacity of a material to store energy.

The chargeability is defined as the ratio between the measured voltage following a sudden change in current ($V_{IP,0}$, Figure 2), normalised with the measured potential before the current change (V_{DC}) (Seigel, 1959) from the following:

$$m_0 = \frac{V_{IP,0}}{V_{DC}}.$$

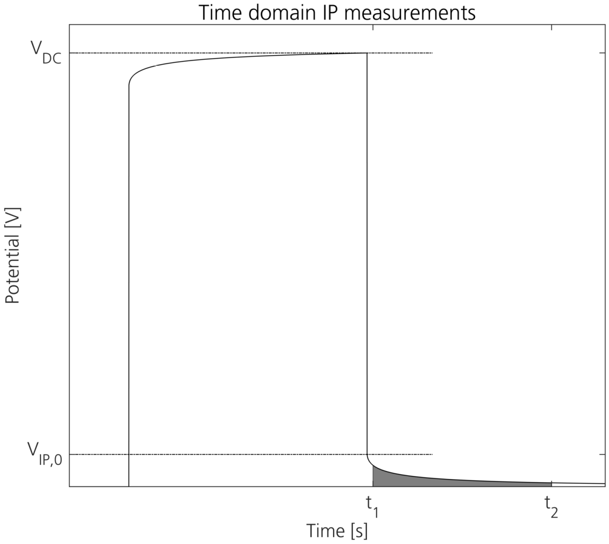

Figure 2. Theoretical full waveform potential for DCIP measurements with indication of parameters important for data evaluation.

The chargeability in the time–domain is determined by considering the transient potential response of the subsurface following a change in the injected current (Figure 2). It can be evaluated in several ways: for chargeability only (definition), for the mean chargeability within a given time interval (integral chargeability, m_{int}):

$$m_{int} = \frac{1}{V_{DC}\Delta t}\int_{t_1}^{t_2} V(t)dt$$

or for normalised integral chargeability (normalised with resistivity, see Slater and Lesmes (2002)) corresponding to surface polarisation (Binley, 2015). Furthermore, the frequency characteristics of the potential response can be considered (spectral chargeability) by using different models for describing the shape (Figure 3) of the IP response (Johnson, 1984; Tombs, 1981), for example the Cole–Cole model in the time–domain is described by (Florsch et al., 2011; Pelton et al., 1978; Revil et al., 2015):

$$V_{IP}(t) = m_0 \sum_{j=0}^{\infty} (-1)^j \left(\frac{t}{\tau}\right)^{jc} \Gamma(1+jc)^{-1}$$

for relaxation time (τ), frequency exponent (c) and Euler's Gamma function (Γ):

$$\Gamma(x) = \int_0^\infty u^{x-1} e^{-u}\, du.$$

Analogous to resistivity and apparent resistivity, it is not possible to retrieve the chargeability model parameters of the subsurface from the DCIP measurements directly, unless it is homogenous in terms of the chargeability parameters. Therefore, inversion is normally needed. The chargeability properties are linear for small current densities used in field surveys, which typically supply less than a few amperes (below ~10^{-2} A/m^2) while non–linear behaviours have been reported for higher current densities, for example in lab measurements (Hallbauer–Zadorozhnaya et al., 2015).

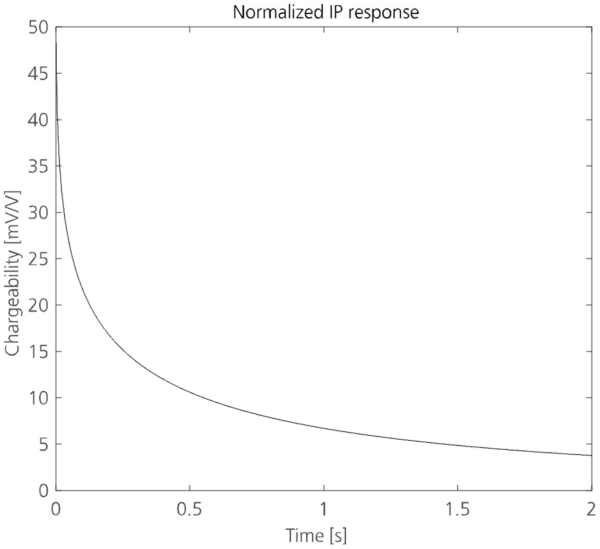

Figure 3. Normalised IP response generated from the modelled measurement seen in Figure 4.

2.3. Waveforms

The current waveform injected into the ground differs depending on whether the measurements are conducted in the time or frequency–domain. Time–domain measurements consider changes with time, while frequency–domain measurements consider at what frequencies the changes take place. The two methods are theoretically equivalent, but differ in terms of measurement and evaluation techniques (Binley, 2015).

2.3.1. Time–domain

Time–domain measurements typically inject a 50% duty cycle square current waveform as pulses of constant amplitude (Figure 4). The polarity of the current is reversed every pulse to remove background potentials superimposed on the signal measured between the receiver electrodes, caused by electrode polarisation effects (Binley, 2015). Thus, at least two pulses with opposite sign are injected. This pulse train can be repeated (stacked) to retrieve multiple readings of the potential response and to reduce the influence of noise.

The potential readings (V_{DC}, Figure 2) for calculating resistivity are taken as an average potential at the end of each current injection so that the potential has had time to stabilise as much as possible and so that the most prominent IP effects have worn off. For IP, the potential readings are taken during the current off–time and the potential is normally averaged within predefined windows, starting at a fixed delay time after the current pulses end. The time windows normally have increasing lengths (Gazoty et al., 2013) and are normally chosen as multiples of the time period of the household power grid frequency (for example 50 Hz and 20 ms in Sweden) to average out harmonic noise. The integral chargeability is determined as a weighted sum of the IP windows while, for spectral IP all windows and timing information are required for the inversion.

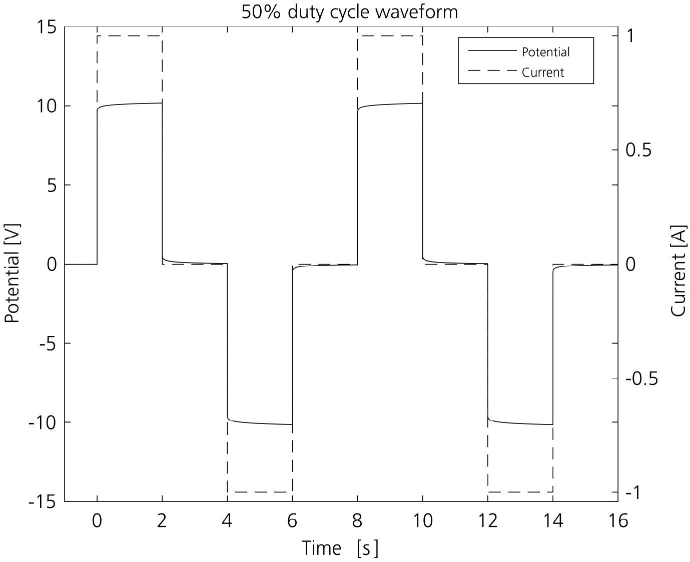

Figure 4. Injected current and modelled measured potential for the 50% duty–cycle waveform used for time–domain DCIP measurements. Two stacks are shown with four pulses and a current on–time of 2 s. The corresponding stacked, averaged and normalised IP response can be seen in Figure 3.

2.3.2. Frequency–domain

In the frequency–domain, current with a sine waveform (Figure 5) of different frequencies is transmitted, while the resistivity and IP information are retrieved as the amplitude and phase shift of the measured potential, respectively (Binley, 2015; Florsch et al., 2011). By applying a narrow passband filter corresponding to the frequency of the current transmitted, it is possible to filter out background drift (~DC), harmonic noise (by avoiding transmissions at harmonic noise frequencies or their harmonics), and partly filter the spikes. However, a recent study based on synthetic modelling and two field surveys demonstrated that it is possible to obtain qualitatively and quantitatively comparable results with the two methods, and that the TD method at present is superior in terms of acquisition time and practical spectral range in the field (Maurya et al., 2018b). The practical spectral range has been further studied in a comparison of the induction–free acquisition range for TD and FD, concluding that TD has a theoretical advantage of up to more than four decades in spectral range (Fiandaca, 2018).

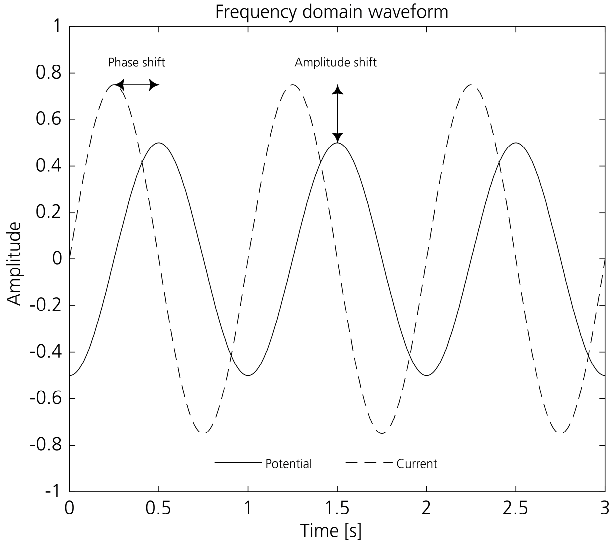

Figure 5. Schematic example of injected current and received potential for frequency–domain resistivity and IP measurements with indications of some relevant quantities. In the figure, it is assumed that the current transmission started well before time zero.

2.4. Sensitivity

Sensitivity (Figure 6) in general describes how changes in model parameters are represented in forward calculations, for example how the change in resistivity in one part of a subsurface model will change the measured apparent resistivity for a specific electrode combination (Binley, 2015). This relationship between model and DCIP data is mathematically given by the Frechet derivative, which can be solved analytically for simple models (such as a homogeneous subsurface), but it does in general require other solution techniques. For example, by parameterising and discretising the model and computing the partial derivatives numerically (McGillivray and Oldenburg, 1990).

Figure 6. Schematic example of 2D–sensitivity distribution for a homogeneous half–space and a specific electrode geometry with current electrodes A and B and potential electrodes M and N. An increase of the parameter value in a positive area (pink) will increase the magnitude of the measured quantity, while the magnitude will decrease if the parameter increase takes place in a negative area (blue).

2.5. Inversion

Inversion (Figure 7) is an iterative process that aims to find a discretised parameter model that produces synthetic measurements (forward responses) that are similar to the measurements observed in reality. During this process, the observed data is compared with the forward responses for a known distribution of model parameters (such as resistivity and chargeability), and the model parameter values are changed until the responses are similar to the real measurements (Binley, 2015; Loke and Barker, 1996; Rücker et al., 2006).

Depending on the type of parameterisation of the inversion, different numbers of parameters are used for describing the model space. For example, with the spectral induced polarisation Cole–Cole model, four parameters are used: resistivity, chargeability, relaxation time, and frequency exponent, where the latter three describe the shape of the IP response (Fiandaca et al., 2013, 2012; Hönig and Tezkan, 2007).

The time–domain resistivity and spectral induced polarisation inversion software described by Fiandaca et al. (2012 and 2013) models the current and potential waveforms, computes the forward response in the frequency–domain and transforms the response into the time–domain for comparing the measured data with the modelled response.

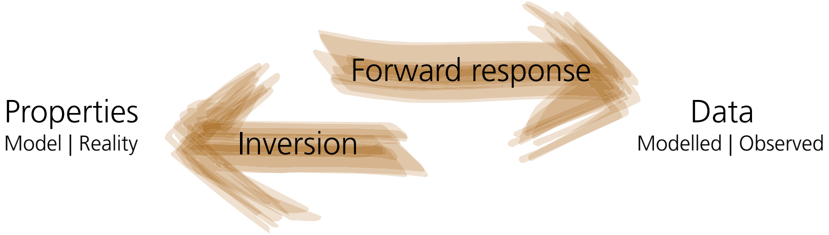

Figure 7. Schematic overview of the relationship between properties (model parameter distribution or real distribution of properties), data (modelled forward responses or observed), forward response and inversion.

3. Results and discussion

Multiple factors are limiting the usability of the DCIP methodology, and many of these are more severe in urban areas. In short, there are three main categories creating bottlenecks for DCIP usability. Firstly, issues with low data quality and reliability limit the successful use of the method in noisy environments. Secondly, the time needed for data acquisition can limit the possibilities for applying the method owing to lack of resources, especially when 3D surveys are needed. Thirdly, the post–processing of acquired data is time consuming and guidelines or knowledge on what is to be considered erroneous IP data are missing because there is a lack of knowledge of what shapes of IP responses are physically possible. This is especially relevant for spectral IP measurements and 3D surveys, both of which require more data; thus requiring more post–processing resources.

3.1. Data quality and reliability

Many technical measurement issues related to different noise sources can be avoided if the measurements are carried out in the frequency–domain instead of in the time–domain. However, frequency–domain measurements are highly time consuming compared to the time–domain (Maurya et al., 2018b) and consequently are rarely used in commercial engineering and environmental applications and are mainly used for research purposes. As this work aims to identify techniques that can be expected to be adapted for routine practical applications, it focuses on developing time–domain measurements and on pushing the limit of the available spectral IP information from direct current resistivity and time–domain induced polarisation measurements.

In field DCIP measurements, the measured potentials can be regarded as a mix of different sources (Figure 8), including the desired ground response of the current injection:

$$u_{measured} = u_{response} + u_{drift} + u_{harmonic\,noise} + u_{spikes} + u_{other}$$

To obtain an accurate determination of the potential response ($u_{response}$), it is essential to reduce or to determine and compensate for as many of the other sources as possible.

Figure 8. Different types of known sources that affect the measured potential and their typical signal characteristics: electrical fence – spikes (top left), power grid – harmonic noise (top right), tram running on DC – anthropogenic background drift (bottom left), DCIP instrument – square pulse train (bottom right).

3.1.1. Background drift

Background drift in DCIP data can originate from multiple sources, for example natural potential differences in the subsurface, natural electrode polarisation (which can be reduced using non–polarisable electrodes), and current induced electrode polarisation (if using the same electrodes for injecting current and measuring potentials). This drift manifests as a slowly changing potential trend in the full waveform potential recording (Figure 9). If not corrected, drift can corrupt both resistivity and chargeability data. However, the tail of the IP response is especially sensitive, owing to its low signal–to–noise ratio. Hence, mainly the spectral IP is affected. The correction for drift is commonly performed with a linear approximation (Dahlin et al., 2002; Peter–Borie et al., 2011).

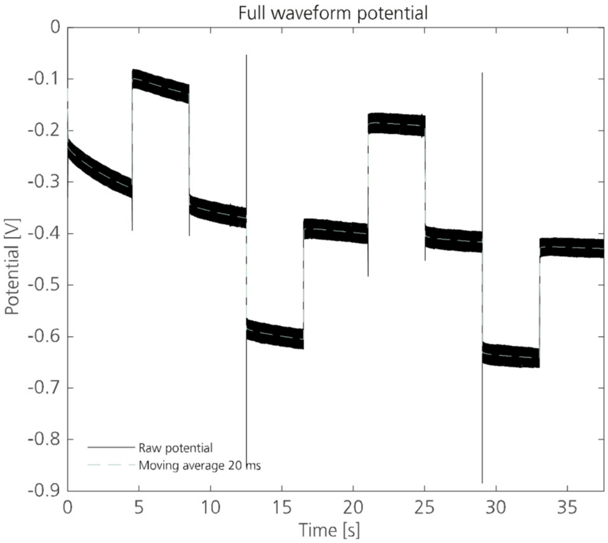

Figure 9. Example of full waveform recording that exhibits a relatively slow background variation mainly caused by current induced electrode polarisation. The full waveform is also shown with a moving average of 20 ms to supress harmonic noise (see 3.1.3 Harmonic noise section).

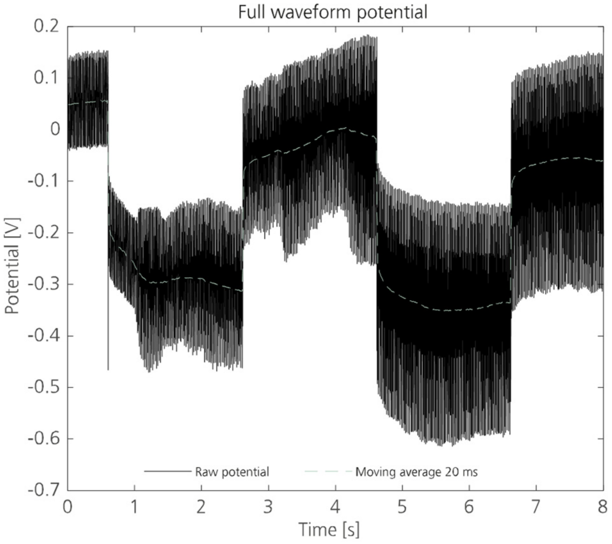

Figure 10. Example of full waveform potential recording (from a 100% duty cycle current waveform, Figure 16) that exhibits a relatively fast variation in background potential, possibly originating from anthropogenic DC noise (metro). The full waveform is also shown with a moving average of 20 ms to supress harmonic noise (see 3.1.3 Harmonic noise section).

Another type of drift originates from anthropogenic DC sources (not related to the DCIP measurements) such as a tram, trolleybus, or metro. Such drifts are characterised by relatively fast variation, in the range of seconds (which is similar to the time range of the DCIP measurement sequence (Figure 10)). This relatively faster variation can corrupt the DCIP potential waveform readings in such a way that they become unusable, and no method has yet been found for filtering and handling such data. At present, the obvious way to deal with the anthropogenic DC noise is to conduct the measurements when the noise rate is low, for example at night, and to identify and remove corrupted measurements from the dataset (Rossi et al., 2018).

3.1.2. Spikes

Spikes originating from anthropogenic sources, such as electrical fences for livestock management, can be registered by DCIP measurements (Figure 11). These spikes can cause problems when extracting DC (resistivity). However, this particularly affects IP information from measured field data, owing to its low signal–to–noise ratio. Additionally, it should be noted that shorter IP gates are more sensitive to spikes because they consist of fewer samples.

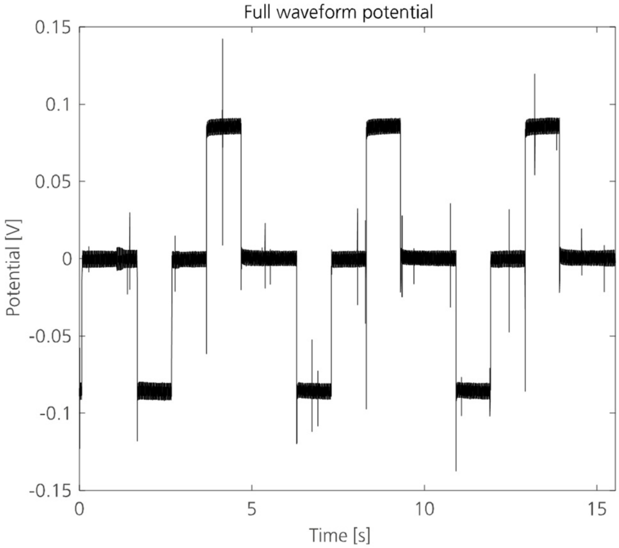

Figure 11. Full waveform potential recording with noise from electrical fences for livestock management (seen as multiple spikes).

3.1.3. Harmonic noise

Harmonic noise originates from power supply sources oscillating at a base frequency (50 Hz or 60 Hz) and its harmonics (Figure 12 and Figure 13). In DCIP processing, this is normally handled by averaging and gating over a full period of the known base frequency (for example 1/50 s or 1/60 s) for suppressing household power supply frequencies at 50 Hz and associated harmonics. However, the requirement for long gates causes a loss of early IP response information close to the current pulse change; making it more difficult to resolve spectral IP parameters (Lajaunie et al., 2016; Madsen et al., 2017). This is especially severe when conducting field measurements close to electric railways in some countries (such as Austria, Germany, Norway, Sweden, Switzerland, and USA) where the frequency of the power supplies for the trains are even lower (16 2/3 Hz or 25 Hz).

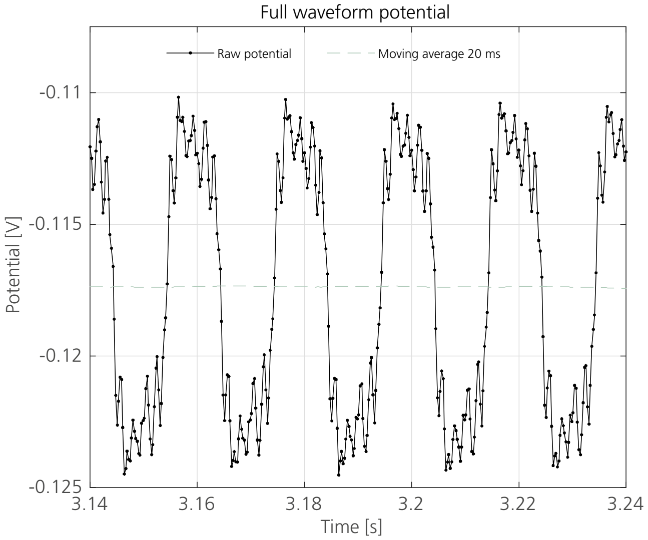

Figure 12. Excerpt of a full waveform potential recording and a moving average (20 ms window) version of the same signal. With this magnification in time, the harmonic oscillations with a main oscillation of a time period of approximately 20 milliseconds are clearly visible.

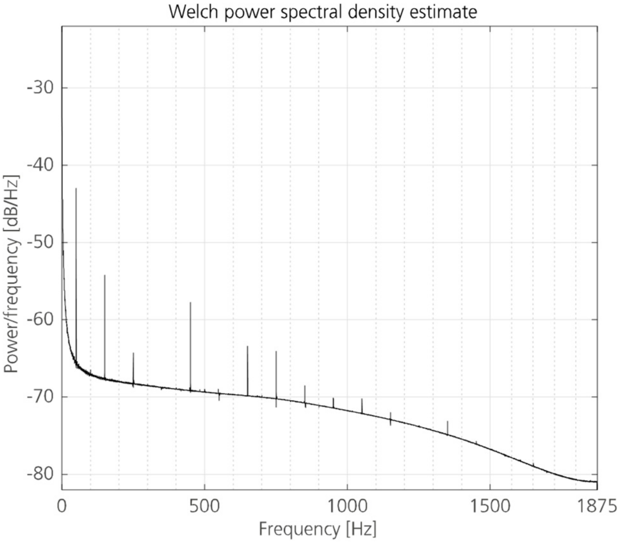

Figure 13. Welch power spectral density estimate for the full waveform potential recording seen in Figure 12 (entire signal). The periodic reoccuring energy peaks at 50 Hz and at (mainly) odd harmonics suggest that noise from a power grid is present in the signal.

3.1.4. Electromagnetic coupling

Field surveys conducted with multicore cables where the potential and current wires are bulked in the same cable (Figure 1 and Figure 14) generally suffer from different forms of electromagnetic (EM) coupling (Dahlin and Leroux, 2012). Handling of EM coupling is not a focus of this work, hence only a very brief overview is given here, but it should be noted that the coupling generally increases for longer arrays, lower resistivity, and higher frequencies (Butler, 2005).

Capacitive coupling can be defined as current leaks from high–potential surfaces or conductors to low–potential surfaces or conductors (Dahlin and Leroux, 2012). With a single multicore cable, three main capacitive couplings can occur (Dahlin and Leroux, 2012; Radic, 2004): coupling between current and potential wires, coupling between the different current wires (*A* and *B*) and coupling between the current wire and the subsurface. The main coupling effect is the one occurring between current and potential wires (Radic, 2004). One method to reduce this coupling is to increase the distance between the current and potential wires by using two multicore cables (Figure 14, top), one for current transmission, and the other for potential measurements (Dahlin and Leroux, 2012).

Inductive coupling operates through magnetic fields and thus differs in origin from capacitive coupling. It is possible to compensate for this coupling by means of modelling and by including it in the inversion (Fiandaca, 2018; Ingeman–Nielsen and Baumgartner, 2006; Kang and Oldenburg, 2018), but because the focus of this work is elsewhere, this has not been considered in this work.

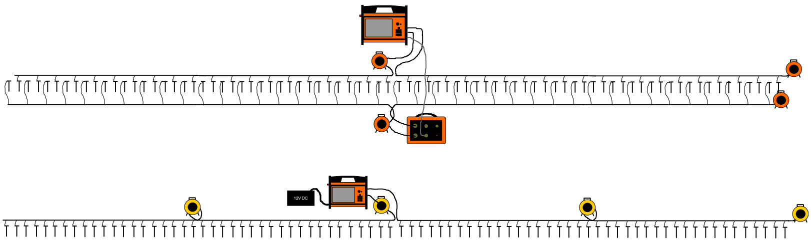

Figure 14. Example of measurement setup with two multicore cables (top). One cable and every second electrode are used for current injection while the remaining cable and electrodes are used for measuring potential. By increasing the distance between the current and potential wires, the capacitive coupling between the two is reduced. An example of the traditional setup is provided for comparison (bottom). Image adapted from original by Torleif Dahlin.

3.1.5. Bottleneck reduction

In this work, reduction of data quality bottlenecks has been achieved in two main forms. Firstly, signal levels have been increased through waveform optimisations and secondly, noise levels have been reduced by signal processing schemes. Data reliability bottlenecks have been reduced in the same manner, and with a method for data driven error estimates in terms of standard deviation (STD) (Paper II).

Specifically, the IP signal levels are increased by up to a factor of two by switching from a 50% to a 100% duty cycle waveform (Figure 16), and taking the IP measurements during the current injection. This causes a superposition of the IP charge–up and discharge and a theoretical doubling of the signal levels.

The noise levels are further supressed by signal processing of recorded full waveforms (Paper II). This processing reduces bottlenecks by improving the handling of spikes, harmonic noise, and slower background drifts. Further, it also increases the overall SNR by introducing the use of tapered and overlapping IP gates. These improvements also double the spectral information content of DCIP data by enabling shorter gates close to the current switch as a result of removing the need for gates to be multiples of the time period of the harmonic noise (Figure 15) and by recovering a more accurate IP response shape at later times. The processing scheme also includes methods for data–driven estimation of the individual uncertainty for each IP gate based on contributions from the different noise sources and the data variability within each gate.

Apart from the surveys presented in the appended papers, these improvements have been successfully applied in several other field surveys (for example Fiandaca et al., 2018; Johansson et al., 2017; Maurya et al., 2018; Olsson et al., 2017). However, the signal–processing scheme is applied after the DCIP acquisition; therefore, it is not possible to use the reliability measures during field acquisition. With real time processing (with more advanced or cloud connected instruments) it could be possible to use the data quality and reliability measures to repeat failed measurements automatically, or to alert DCIP operators to possible issues, to further enhance data quality and reliability. Additionally, issues remain with faster varying background potential, such as the one generated by anthropogenic DC sources (for example metro and trams).

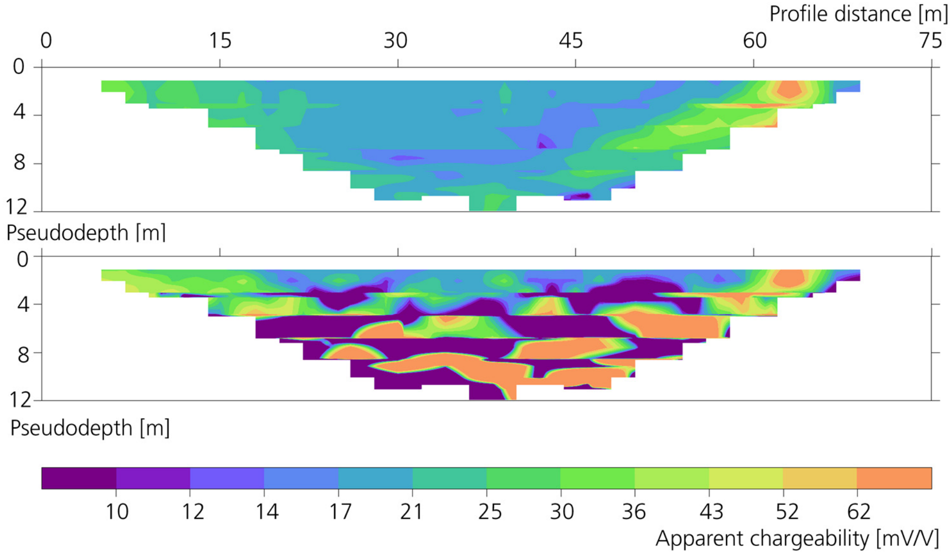

Figure 15. Pseudosections for IP gate 9 (width of approximately 5 ms, center gate time at approximately 16 ms) exemplifying the effect on data quality from full waveform processing (top) and the corresponding pseudosection with standard processing (bottom). Note that pseudosections with smooth transitions in apparent magnitude generally indicate data of good quality.

3.2. Acquisition time

The time needed for a DCIP survey can generally be divided into two parts, excluding the time related to logistics for personnel and equipment. The first part is hardware related, including time spent on positioning and aligning the equipment, installing electrodes, connecting cables, ensuring good electrode contact, and the reverse procedure at the end of the survey. The second part relates to the acquisition of the

DCIP data, where the measurement instruments inject a specific current waveform into the ground and measure potentials in a predefined sequence of electrode combinations. The focus in this work is on the second part.

For a given DCIP instrument, the time needed for the acquisition of a DCIP dataset mainly depends on two factors: the time needed for a full current injection waveform, and how many times this waveform needs to be repeated. This refers to how many and what combinations of electrodes for injecting current and measuring potentials are to be included in the dataset.

3.2.1. Waveform time

For the 50% duty–cycle waveform, the time needed for a full current injection sequence (positive and negative pulses, off–time and stacking), scales linearly with both the pulse duration and the number of stacks. For example, with 2 s pulses and two stacks, the total waveform time is 16 s (Figure 2). Doubling the stacks or the pulse duration to four would double the waveform time (32 s). Furthermore, for a given instrument, the acquisition time scales approximately linearly with the waveform time, neglecting overhead time related to instrument relay switching and transmitter setup. Some instruments, such as the ABEM Terrameter LS series, are capable of employing adaptive stacking within some predefined bounds based on the V_{DC} variance, and attempt to reduce it below a specified threshold. However, owing to superposition of potential responses from previous pulses, the theoretical V_{DC} and especially V_{IP} values are different for each pulse (Fiandaca et al., 2013, 2012). Thus, such adaptive stacking possibilities are not considered in this work.

3.2.2. Sequence time

For a specific waveform and DCIP instrument with a given number of Tx– and Rx–channels, switching capacity, and other factors, the time needed for acquiring the full measurement sequence only depends on the measurement protocol used. The measurement protocol describes which current and potential electrode pair combinations are to be measured for the dataset. The protocol is typically predefined prior to a survey and is generally optimised for resolution, SNR, lateral and vertical data density based on homogeneous half–space modelling, and on its efficiency for multi Rx–channel use (Dahlin and Zhou, 2006). Some reduction in sequence time is achieved by measuring multiple potentials with several Rx–channels, for example up to 12 for the ABEM Terrameter LS2 instrument, or by transmitting current with several Tx channels, for example up to three for the Syscal Multi–Tx instrument. The multiple Tx–technique places special demands on the transmitted waveforms, where using code–division multiple–access for separating the signals requires that any waveform pair must be mutually orthogonal (having scalar products equal to zero) (Yamashita et al., 2014).

3.2.3. Bottleneck reduction

In this work, reduction in acquisition time has been achieved by means of reducing the waveform time. Specifically, with the typically used 50% duty cycle current waveform, only half of the waveform time is available for resistivity and IP measurements. In contrast, the 100% duty cycle waveform (Figure 16) and taking the IP measurements while the current is being transmitted the full duration of the waveform are used for measurements. With numerical modelling of current waveforms with 50% and 100% duty cycles, Paper I also demonstrates that the waveforms have comparable sensitivity regarding the spectral Cole–Cole parameters. Furthermore, inversion of field data acquired with both waveforms confirms the modelling results and confirms that it is possible to retrieve similar spectral Cole–Cole inversion models if the waveform of the injected current is included in the forward computations.

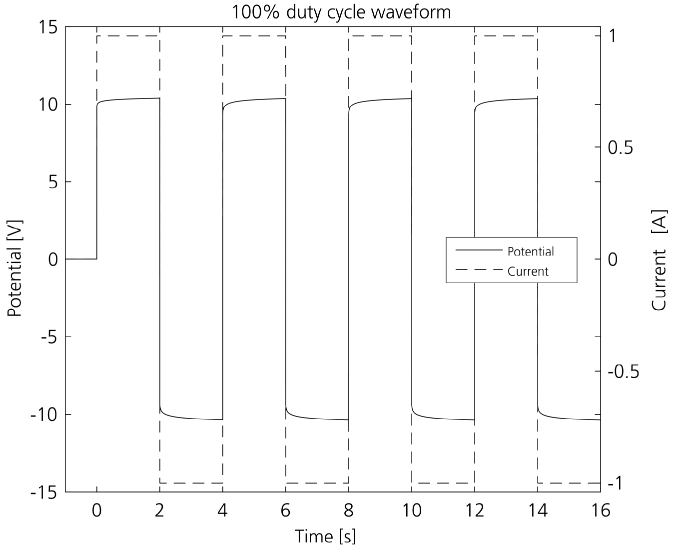

Figure 16. Injected current and modelled measured potential for a 100% duty–cycle waveform. With a pulse duration of 2 s, four stacks are achieved in 16 s compared to two stacks with the 50% duty–cycle (Figure 4). For the same number of stacks, the 100% duty–cycle would require 8 s.

Another aspect of the waveform time is related to the pulse duration and number of stacks, where the effects of varying pulse duration are discussed in Paper IV. For short waveforms and thus acquisition time, it is desirable to use short pulse durations (and few stacks). On the other hand, it is desirable to use longer pulses (and more stacks) to improve data quality and spectral information content. Thus, there is a trade–off between data quality and acquisition time, though Paper IV shows that it is possible to obtain similar inversion models independent of pulse duration, within almost one order of magnitude in pulse duration difference, if noise and geological conditions are favourable. Furthermore, for field surveys, the waveform is typically fixed by the operator (at best), after considerations regarding expected noise conditions, chargeability magnitudes, and available resources for time spent in the field. Instead, it may be possible to determine the noise and spectral IP conditions continuously, to dynamically optimise the waveform throughout the survey based on noise levels and on the required subsurface information to decrease the acquisition time further.

The acquisition time bottleneck reductions can have a significant impact on DCIP surveys in general. This is especially true for surveys where time (and cost) efficiency and reliable data quality are important factors. Specifically, the findings are of value for DCIP surveys conducted in urban areas where the heterogeneous subsurface demands time–consuming 3D acquisitions. However, bottleneck reductions in this work have only considered waveform optimisations, while there are also possibilities for further optimisation based on sequence time. This can be achieved by reducing protocol size, or dynamically adapting it to estimated subsurface conditions instead of to a homogeneous half space (Stummer et al., 2002) or by improved hardware, for example by increasing the number of Tx/Rx channels.

3.3. Data post–processing

Here, data post–processing refers to processing of DCIP data after the measurements, but before the inversion. Such processing involves visual inspection of the acquired data; meaning plotted as pseudosections or IP responses as magnitude–vs–time plots. The purpose of post–processing is to determine which data should be forwarded to the inversion routine, and which should be considered as outliers or measurement errors. Currently, this is essentially a manual process, and it is also based on the experience and knowledge of the individual or individuals managing the processing without general scientifically based guidelines. However, recent studies have presented methods for semi–automated IP processing for integral chargeability and strictly decaying full IP responses (Flores Orozco et al., 2018; Rossi et al., 2018).

For data of excellent quality, manual post–processing can be relatively fast but post–processing of larger full IP response datasets for spectral inversion can take several days to complete. Additionally, post–processing involves largely manual labour requiring experienced and skilled personnel. Thus, practitioners may be unable to successfully use the DCIP method owing to lack of resources for post–processing, especially in low resource applications or for spectral induced polarisation inversions that require additional data post–processing.

3.3.1. Bottleneck reduction

In this study, data post–processing bottlenecks are reduced by improving the data quality and estimating its reliability, as previously described (see 3.1 Data quality and reliability section), and by increasing the knowledge on what types of IP responses are physically possible. Specifically, a basic mechanism (Figure 17) for previously disregarded IP responses is described in Paper IV. Furthermore, a classification system based on the temporal development of the IP response magnitude and its derivative is introduced for seven different types. This novel knowledge and classification will facilitate decisions in the manual processing work and could reduce the required resources for this type of task. Furthermore, it could lay the foundation towards semi–automated post–processing steps to reduce the need for manual work significantly. Such improvements would be very beneficial for DCIP post–processing in general. This is especially true for large 3D datasets or data acquired in low SNR conditions (or both), as discussed in a recent study (Rossi et al., 2018) for inversion of integral chargeability data. Corresponding semi–automated processing for full response IP data could encourage and increase the use of spectral full IP response inversions.

Solely considering the integral chargeability can be misleading, and probably makes it more ambiguous when trying to relate IP models to processes and geology, or previously reported integral chargeability values. Furthermore, if the full waveform is not included in the inversion, care needs to be taken to make certain that the same acquisition settings are used when making complimentary, verification, or time–lapse measurements. This ensures that different data sets will be comparable in both the data and the model space.

Figure 17. Schematic description of the basic mechanism for the superposition of individual IP responses (from IP anomaly regions ℓ_1 and ℓ_2) and the origin of non–standard IP responses ($\ell_1+\ell_2$). Superposition of contribution from positive (pink) and negative (blue) sensitivity regions with different IP response shapes gives a total IP response crossing zero mV/V.

3.4. DCIP survey example

A large–scale DCIP survey was carried out close to Dalby municipality in Southern Sweden to map geological structures and the depth to the bedrock (Paper V). Four profiles, up to one kilometre in length, were acquired in the survey, which enabled the retrieval of subsurface information to approximately 200 metres below the surface. Furthermore, the inferences from Papers I, II and IV were used in the survey to reduce the acquisition time and to improve the data quality and reliability: 100% duty–cycle current waveform with 4 s pulses and full waveform signal processing. The results from the survey are presented in detail in Paper V. In general, the survey was able to map depth to bedrock and main features related to a major geological deformation zone (the Tornquist zone, trending south–east to north–west), and larger weathering zones.

Another DCIP acquisition of smaller scale (Olsson et al., 2017) which also made use of the results from Papers I, II and IV was carried out in a quarry just north of the large scale survey. Six parallel profiles, approximately 160 metres in length (Figure 18), were acquired in the vicinity of the active quarry, which enabled detailed documentation of the bedrock in quasi–3D space as the quarry operation progressed further into the subsurface volume investigated with geophysics. The geological interpretation of the documentation shows the presence of granitic gneiss, amphibolite and diabase as well as faults, brecciated zones, clay weathering and mineralisation within the investigated volume. An amphibolite unit, which also coincides with a vertical fault and weathered zone, is seen in Figure 18 as a slightly darker area at around 30 metres from the right hand side of the profile.

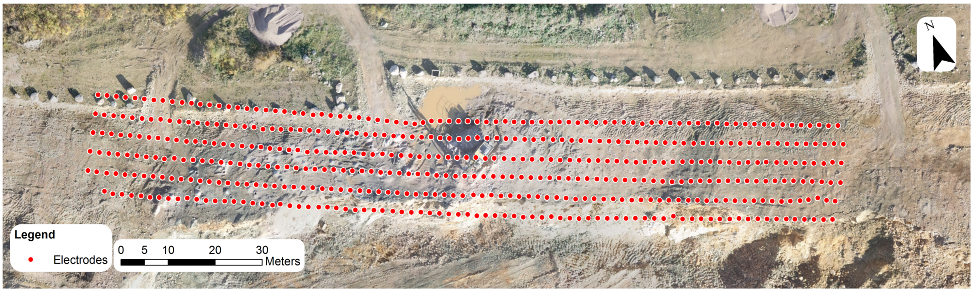

Figure 18. Overview of electrode positions together with an aerial photo taken approximately half a year after the geophysical field survey. Note that the overburden that was present during the field survey has been excavated and the slightly darker structure at approximately 30 metres from the right hand side of the profile shows the presence of amphibolite rock.

With these dense 2D DCIP profiles, it is viable to conduct a full 3D inversion of all profiles simultaneously. However, 3D inversion software that handles spectral IP, and models the transmitter and receiver waveform, is not available. Consequently, the

DCIP data was inverted with standard 3D inversion software (Res3Dinv, version 3.11.62) for resistivity and integral chargeability and thus the retrieved IP parameters will not correspond to a quantitative material property (see Paper III). However, the IP parameter distribution will still show qualitative differences in chargeability magnitude.

Figure 19 shows parts of the models from the 3D inversion as resistivity (top) and integral chargeability (bottom) together with a textured terrain model based on structure–from–motion and drone photography. The low–resistive zone with slightly lower integral chargeability (below 5 mV/V) on the right hand side extends to the full depth of the model, and coincides with the previously mentioned vertical fault and weathered zone next to the amphibolite. The lower resistivity in this area corresponds well with what is interpreted as weathered fracture zones in Paper V, though the orientation of the geophysical anomaly (south–west to north–east) suggests that it is related to another deformation zone (such as the Protogine zone).

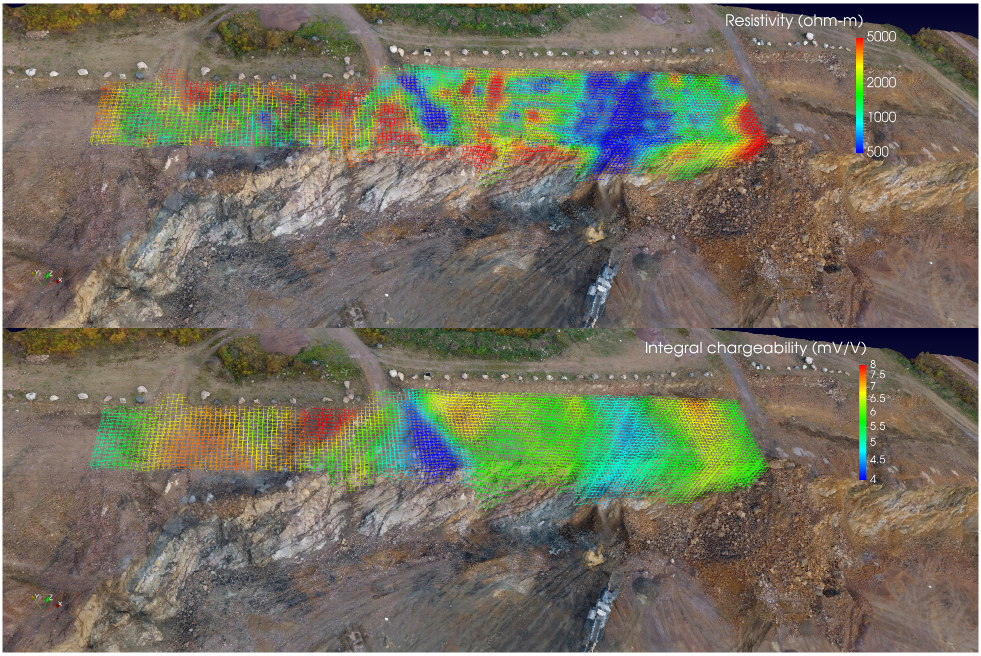

Figure 19. Visualisations of resistivity (top) and integral chargeability (bottom) inversion models together with a textured terrain model based on structure–from–motion drone photography. In the figure, most top parts of the inversion models are visible because the overburden that was present during the field survey was removed before acquiring the data for the terrain model.

4. Conclusions

The work presented in this thesis demonstrates that many usability bottlenecks of the DCIP method can be reduced. Specifically, field resource efficiency is increased by means of current on–time IP measurements and waveform optimisation, which speed up IP measurements and increases the SNR by up to a factor of two. Additionally, resources needed for data post–processing are reduced by improvements in data quality through a comprehensive full waveform signal–processing scheme. Data post–processing is further facilitated by increasing the data reliability through data driven error estimates, and by improving our basic understanding of physically possible responses. Furthermore, the available spectral information from DCIP surveys is substantially increased by enabling extraction of the IP response closer to the pulse than was previously possible. In combination with more accurate removal of background drift potential that can handle non–linear drift cases, the data quality is improved at late times and the spectral information content is further increased.

This work has provided tools and demonstrated their applicability for substantially increasing data quality of the spectral IP, and increasing the understanding of possible responses. However, extensive work regarding manual quality assurance and filtering of the IP response data is still required to enable successful interpretations and spectral IP inversions. Hence, there is scope for further development related to data acquisition, quality, and post–processing.

However, this work adds small but substantial contributions to the advancement and scientific understanding of the DCIP method. As such, after implementation and dissemination, it can contribute to and increase the use of the method for acquiring detailed subsurface information in applications such as construction projects, hydrogeological mapping and environmental projects. This information can hopefully lead to a more sustainable society, by enabling more informed decisions regarding the subsurface, leading to more efficient resource use and reduced risks in terms of economy, society, and the environment.

5. Future research

As indicated in previous sections, there remain many issues to be resolved for making spectral DCIP interpretation a standard tool in applied engineering applications.

5.1. Data quality and reliability

5.1.1. Anthropogenic DC noise

There are some field cases where noise sources that have a large effect on the measured potential cannot be handled by the processing routine described in Paper II. Specifically, such a noise source could be electrical vehicles running on DC (for example trams), generating a slowly varying DC offset with similar time–scale as the IP responses. Another problematic noise source can be trains running on AC passing close to a field survey, generating harmonic noise with a fast varying amplitude and phase, possibly too fast to be modelled with the current implementation of harmonic de–noising described by Paper II.

One possible approach to this issue could be to use differential measurements by separately measuring and compensating accordingly for these noise sources. This reference technique has been successfully applied in previous research, but only for few electrode combinations (Halverson et al., 1989; Radic, 2014).

5.1.2. Electromagnetic coupling

Electromagnetic coupling limits how close to the current switching point it is possible to use the DCIP data, limiting the spectral information content. Hardware improvements (such as cables or instruments) could possibly reduce some of the coupling effect. Other coupling sources (for example inductive) could be handled by keeping the affected data and by including the inductive coupling in the forward response and processing it in the inversion routine.

5.1.3. Data reliability at acquisition

The signal–processing scheme presented in this work is applied after the DCIP acquisition; thus, it is not possible to use the reliability measures during field acquisition. With real time processing (using more advanced or cloud connected instruments), it may be possible to use the data quality and reliability measures to automatically repeat failed measurements or to alert DCIP operators to possible issues, further enhancing the final data quality and reliability. This would possibly increase the survey time, but could also result in a more reliable and complete dataset after removal of erroneous data, increase the usefulness of the DCIP results, and reduce the time needed for data post–processing.

5.2. Survey time

5.2.1. Hardware

Instrumentation with more Tx and Rx channels would reduce the survey time further. Additionally, the possibility of using distributed (galvanically–separated) Tx and Rx instrumentation could facilitate logistics regarding deployment of measurement equipment at sites with restricted areas, for example surveys at different sides of major roads. Distributed systems would also increase the degree of freedom for electrode placements.

5.2.2. Dynamic waveform and protocol

The waveform time could possibly be further optimised regarding the pulse duration by dynamically adapting it to the desired subsurface information (spectral IP or only resistivity) and field conditions, such as noise and spectral response. Similarly, protocols could be dynamically optimised in the field for maximising SNR, sensitivity, lateral and vertical resolution for a predefined volume–of–interest, based on estimated electrical properties instead of based on a homogeneous half–space. With such a system, one or several subsurface volumes (or areas for 2D) could be defined for investigation, instead of defining a measurement protocol. Furthermore, additional electrode positions could be suggested in the field for further improving the information in the volume–of–interest.

5.3. Data post–processing

5.3.1. Automated data processing

Generally, spectral IP evaluation still demands large amounts of manual processing and filtering of erroneous data points before inversion is possible. With increasing data sets, and with typically thousands of electrode combinations and (for example) 40 IP gates per response, there is a need for automatic processing and filtering of the IP response data. Furthermore, recently developed methods only consider positive, strictly decaying IP responses as non–erroneous data, although other types of IP responses are physically possible. This calls for more advanced processing schemes, and could possibly be achieved by means of artificial intelligence. For example, machine learning together with continued research on what types of responses are physically possible.

6. References

Argote–Espino, D., Tejero–Andrade, A., Cifuentes–Nava, G., Iriarte, L., Farías, S., Chávez, R.E., López, F., 2013. 3D electrical prospection in the archaeological site of El Pahñú, Hidalgo State, Central Mexico. J. Archaeol. Sci. 40, 1213–1223. https://doi.org/10.1016/j.jas.2012.08.034

Auken, E., Doetsch, J., Fiandaca, G., Christiansen, A.V., Gazoty, A., Cahill, A.G., Jakobsen, R., 2014. Imaging subsurface migration of dissolved CO2 in a shallow aquifer using 3–D time–lapse electrical resistivity tomography. J. Appl. Geophys. 101, 31–41. https://doi.org/10.1016/j.jappgeo.2013.11.011

Auken, E., Pellerin, L., Christensen, N.B., Sørensen, K., 2006. A survey of current trends in near–surface electrical and electromagnetic methods. Geophysics 71, 249–260. https://doi.org/10.1190/1.2335575

Binley, A., 2015. Tools and Techniques: Electrical Methods, in: Treatise on Geophysics. Elsevier, pp. 233–259. https://doi.org/10.1016/B978–0–444–53802–4.00192–5

Butler, D.K., 2005. Near–surface geophysics. Society of Exploration Geophysicists Tulsa, ISBN: 1560801301.

Dahlin, T., 2001. The development of DC resistivity imaging techniques. Comput. Geosci. 27, 1019–1029.

Dahlin, T., Bjelm, L., Svensson, C., 1999. Use of electrical imaging in site investigations for a railway tunnel through the Hallandsås Horst, Sweden. Q. J. Eng. Geol. Hydrogeol. 32, 163–173.

Dahlin, T., Leroux, V., 2012. Improvement in time–domain induced polarization data quality with multi–electrode systems by separating current and potential cables. Near Surf. Geophys. 10, 545–656. https://doi.org/10.3997/1873–0604.2012028

Dahlin, T., Leroux, V., Nissen, J., 2002. Measuring techniques in induced polarisation imaging. J. Appl. Geophys. 50, 279–298. https://doi.org/10.1016/S0926–9851(02)00148–9

Dahlin, T., Rosqvist, H., Leroux, V., 2010. Resistivity–IP mapping for landfill applications. First Break 28.

Dahlin, T., Zhou, B., 2006. Multiple–gradient array measurements for multichannel 2D resistivity imaging. Near Surf. Geophys. 4, 113–123. https://doi.org/10.3997/1873–0604.2005037

Doetsch, J., Fiandaca, G., Auken, E., Christiansen, A.V., Cahill, A.G., 2015a. Field–scale time–domain spectral induced polarization monitoring of geochemical changes induced by injected CO2 in a shallow aquifer. Geophysics 16, 10294. https://doi.org/10.1190/geo2014–0315.1

Doetsch, J., Ingeman–Nielsen, T., Christiansen, A. V., Fiandaca, G., Auken, E., Elberling, B., Adamson, K., Lane, T., Elberling, B., 2015b. Direct current (DC) resistivity and induced polarization (IP) monitoring of active layer dynamics at high temporal resolution. Cold Reg. Sci. Technol. 119, 16–28. https://doi.org/10.1016/j.coldregions.2015.07.002

Fetter, C.W., 2001. Applied hydrogeology. Prentice Hall, Upper Saddle River N.J., ISBN: 0131226878.

Fiandaca, G., 2018. Induction–free acquisition range in spectral time– and frequency–domain induced polarization at field scale. Geophys. J. Int.

Fiandaca, G., Auken, E., Christiansen, A.V., Gazoty, A., 2012. Time–domain–induced polarization: Full–decay forward modeling and 1D laterally constrained inversion of Cole–Cole parameters. Geophysics 77, E213–E225. https://doi.org/10.1190/geo2011–0217.1

Fiandaca, G., Maurya, P.K., Balbarini, N., Hördt, A., Christiansen, A. V., Foged, N., Bjerg, P.L., Auken, E., 2018. Permeability Estimation Directly From Logging–While–Drilling Induced Polarization Data. Water Resour. Res. 54, 2851–2870. https://doi.org/10.1002/2017WR022411

Fiandaca, G., Ramm, J., Binley, A., Gazoty, A., Christiansen, A.V., Auken, E., 2013. Resolving spectral information from time domain induced polarization data through 2–D inversion. Geophys. J. Int. 192, 631–646. https://doi.org/10.1093/gji/ggs060

Fink, J.B., 1990. Induced polarization: applications and case histories. Soc of Exploration Geophysicists, ISBN: 0931830893.

Flores Orozco, A., Gallistl, J., Bücker, M., Williams, K.H., 2018. Decay curve analysis for data error quantification in time–domain induced polarization imaging. Geophysics 83, E75–E86. https://doi.org/10.1190/geo2016–0714.1

Florsch, N., Llubes, M., Téreygeol, F., Ghorbani, A., Roblet, P., 2011. Quantification of slag heap volumes and masses through the use of induced polarization: application to the Castel–Minier site. J. Archaeol. Sci. 38, 438–451. https://doi.org/10.1016/j.jas.2010.09.027

Gazoty, A., Fiandaca, G., Pedersen, J., Auken, E., Christiansen, A.V., 2013. Data repeatability and acquisition techniques for time–domain spectral induced polarization. Near Surf. Geophys. 11, 391–406. https://doi.org/10.3997/1873–0604.2013013

Gazoty, A., Fiandaca, G., Pedersen, J., Auken, E., Christiansen, A. V., Pedersen, J.K., 2012a. Application of time domain induced polarization to the mapping of lithotypes in a landfill site. Hydrol. Earth Syst. Sci. 16, 1793–1804. https://doi.org/10.5194/hess–16–1793–2012

Gazoty, A., Fiandaca, G., Pedersen, J., Auken, E., Christiansen, A. V, 2012b. Mapping of landfills using time–domain spectral induced polarization data: The Eskelund case study. Near Surf. Geophys. 10, 575–586. https://doi.org/10.3997/1873–0604.2012046

Glover, P.W.J., 2015. Geophysical Properties of the Near Surface Earth: Electrical Properties, Treatise on Geophysics. Elsevier B.V., ISBN: 9780444538024. https://doi.org/10.1016/B978–0–444–53802–4.00189–5

Hallbauer–Zadorozhnaya, V., Santarato, G., Abu Zeid, N., 2015. Non–linear behaviour of electrical parameters in porous, water–saturated rocks: A model to predict pore size distribution. Geophys. J. Int. 202, 871–886. https://doi.org/10.1093/gji/ggv161

Hönig, M., Tezkan, B., 2007. 1D and 2D Cole–Cole–inversion of time–domain induced–polarization data. Geophys. Prospect. 55, 117–133. https://doi.org/10.1111/j.1365–2478.2006.00570.x

Ingeman–Nielsen, T., Baumgartner, F., 2006. Numerical modelling of complex resistivity effects on a homogenous half–space at low frequencies. Geophys. Prospect. 54, 261–271. https://doi.org/10.1111/j.1365–2478.2006.00532.x

Johansson, S., Sparrenbom, C., Fiandaca, G., Lindskog, A., Olsson, P.–I., Dahlin, T., Rosqvist, H., 2017. Investigations of a Cretaceous limestone with spectral induced polarization and scanning electron microscopy. Geophys. J. Int. 208, 954–972. https://doi.org/10.1093/gji/ggw432

Johnson, I.M., 1984. Spectral induced polarization parameters as determined through time–domain measurements. Geophysics 49, 1993–2003. https://doi.org/10.1190/1.1441610

Kang, S., Oldenburg, D.W., 2018. Time domain electromagnetic–induced polarisation: extracting more induced polarisation information from grounded source time domain electromagnetic data. Geophys. Prospect. 66, 74–86. https://doi.org/10.1111/1365–2478.12600

Kemna, A., Binley, A., Slater, L., 2004. Crosshole IP imaging for engineering and environmental applications. Geophysics 69, 97–107. https://doi.org/10.1190/1.1649379

Lajaunie, M., Maurya, P.K., Fiandaca, G., 2016. Comparison of Cole–Cole and Constant Phase Angle modeling in Time–Domain Induced Polarization, in: Proceedings of the 4th International Workshop on Induced Polarization. Aarhus, Denmark.

Leroux, V., Dahlin, T., 2005. Time–lapse resistivity investigations for imaging saltwater transport in glaciofluvial deposits. Environ. Geol. 49, 347–358. https://doi.org/10.1007/s00254–005–0070–7

Leroux, V., Dahlin, T., Svensson, M., 2007. Dense resistivity and induced polarization profiling for a landfill restoration project at Härlov, Southern Sweden. Waste Manag. Res. 25, 49–60. https://doi.org/10.1177/0734242X07073668

Loke, M.H., Barker, R.D., 1996. Practical techniques for 3D resistivity surveys and data inversion1. Geophys. Prospect. 44, 499–523. https://doi.org/10.1111/j.1365–2478.1996.tb00162.x

Loke, M.H., Chambers, J.E., Rucker, D.F., Kuras, O., Wilkinson, P.B., 2013. Recent developments in the direct–current geoelectrical imaging method. J. Appl. Geophys. 95, 135–156. https://doi.org/10.1016/j.jappgeo.2013.02.017

Madsen, L.M., Fiandaca, G., Auken, E., Christiansen, A.V., 2017. Time–domain induced polarization – an analysis of Cole–Cole parameter resolution and correlation using Markov Chain Monte Carlo inversion. Geophys. J. Int. 211, 1341–1353. https://doi.org/10.1093/gji/ggx355

Madsen, L.M., Fiandaca, G., Christiansen, A.V., Auken, E., 2018. Resolution of well–known resistivity equivalences by inclusion of time–domain induced polarization data. Geophysics 83, E47–E54. https://doi.org/10.1190/geo2017–0009.1

Maurya, P.K., Balbarini, N., Møller, I., Rønde, V., Christiansen, A. V, Bjerg, P.L., Auken, E., Fiandaca, G., 2018a. Subsurface imaging of water electrical conductivity, hydraulic permeability and lithology at contaminated sites by induced polarization. Geophys. J. Int. 213, 770–785. https://doi.org/10.1093/gji/ggy018

Maurya, P.K., Fiandaca, G., Christiansen, A. V, Auken, E., 2018b. Field–scale comparison of frequency– and time–domain spectral induced polarization. Geophys. J. Int. 214, 1441–1465. https://doi.org/10.1093/gji/ggy218

Maurya, P.K., Rønde, V.K., Fiandaca, G., Balbarini, N., Auken, E., Bjerg, P.L., Christiansen, A.V., 2017. Detailed landfill leachate plume mapping using 2D and 3D electrical resistivity tomography – with correlation to ionic strength measured in screens. J. Appl. Geophys. 138, 1–8. https://doi.org/10.1016/J.JAPPGEO.2017.01.019

McGillivray, P.R., Oldenburg, D.W., 1990. Methods for calculating frechet derivatives and sensitivities for the non–linear inverse problem: a comparative study1. Geophys. Prospect. 38, 499–524. https://doi.org/10.1111/j.1365–2478.1990.tb01859.x

Nijland, W., van der Meijde, M., Addink, E.A., de Jong, S.M., 2010. Detection of soil moisture and vegetation water abstraction in a Mediterranean natural area using electrical resistivity tomography. CATENA 81, 209–216. https://doi.org/10.1016/j.catena.2010.03.005

Olsson, P.–I., 2016. Optimization of time domain induced polarization data acquisition and spectral information content, (Licentiate Thesis). Lund University, Lund, ISBN: 9789176236727.

Olsson, P.–I., Jonsson, P., Johansson, S., Johansson, L., 2017. BeFo 382 – Detailed Comparison Study of 3D–characterized Rock Mass and Geophysical Models, in: Near Surface Geoscience 2017 – 23rd European Meeting of Environmental and Engineering Geophysics. Malmö, Sweden. https://doi.org/10.3997/2214–4609.201702005

Pelton, W.H., Ward, S.H., Hallof, P.G., Sill, W.R., Nelson, P.H., 1978. Mineral discrimination and removal of inductive coupling with multifrequency IP. Geophysics 43, 588–609. https://doi.org/10.1190/1.1440839

Peter–Borie, M., Sirieix, C., Naudet, V., Riss, J., 2011. Electrical resistivity monitoring with buried electrodes and cables: noise estimation with repeatability tests. Near Surf. Geophys. 9, 369–380. https://doi.org/10.3997/1873–0604.2011013

Radic, T., 2004. Elimination of Cable Effects while Multi–Channel SIP Measurements, in: Near Surface 2004 – 10th EAGE European Meeting of Environmental and Engineering Geophysics. Utrecht, The Netherlands, pp. 1–4.

Revil, A., Binley, A., Mejus, L., Kessouri, P., 2015. Predicting permeability from the characteristic relaxation time and intrinsic formation factor of complex conductivity spectra. Water Resour. Res. 51, 6672–6700. https://doi.org/10.1002/2015WR017074

Rossi, M., Dahlin, T., Olsson, P.–I., Günther, T., 2018. Data acquisition, processing and filtering for reliable 3D resistivity and time–domain induced polarisation tomography in an urban area: field example of Vinsta, Stockholm. Near Surf. Geophys. 220–229. https://doi.org/10.3997/1873–0604.2018014

Rücker, C., Günther, T., Spitzer, K., Rücker, C., Spitzer, K., 2006. Three–dimensional modelling and inversion of dc resistivity data incorporating topography – I. Modelling. Geophys. J. Int. 166, 495–505. https://doi.org/10.1111/j.1365–246X.2006.03011.x

Seigel, H.O., 1959. Mathematical formulation and type curves for induced polarization. Geophysics 24, 547–565. https://doi.org/10.1190/1.1438625

Slater, L., Ntarlagiannis, D., Yee, N., O'Brien, M., Zhang, C., Williams, K.H., 2008. Electrodic voltages in the presence of dissolved sulfide: Implications for monitoring natural microbial activity. Geophysics 73, F65–F70. https://doi.org/10.1190/1.2828977

Slater, L.D., Glaser, D.R., 2003. Controls on induced polarization in sandy unconsolidated sediments and application to aquifer characterization. Geophysics 68, 1547. https://doi.org/10.1190/1.1620628

Slater, L.D., Lesmes, D., 2002. IP interpretation in environmental investigations. Geophysics 67, 77–88. https://doi.org/10.1190/1.1451353

Stummer, P., Maurer, H., Horstmeyer, H., Green, A.G., 2002. Optimization of DC resistivity data acquisition: real–time experimental design and a new multielectrode system. IEEE Trans. Geosci. Remote Sens. 40, 2727–2735. https://doi.org/10.1109/TGRS.2002.807015

Sumner, J.S., 1976. Principles of induced polarization for geophysical exploration. Elsevier, ISBN: 0444599878.

Tombs, J.M.C., 1981. The feasibility of making spectral IP measurements in the time domain. Geoexploration 19, 91–102. https://doi.org/10.1016/0016–7142(81)90022–3

Yamashita, Y., Lebert, F., Gourry, J.C., Bourgeois, B., Texier, B., 2014. Time–domain Induced Polarization Profile with Multiple–current Transmission, in: Near Surface Geoscience 2014 – 20th European Meeting of Environmental and Engineering Geophysics. Athens, Greece, pp. 1–5. https://doi.org/10.3997/2214–4609.20141985

Zonge, K., Wynn, J., Urquhart, S., 2005. 9. Resistivity, Induced Polarization, and Complex Resistivity, in: Near–Surface Geophysics. Society of Exploration Geophysicists, pp. 265–300. https://doi.org/10.1190/1.9781560801719.ch9

Paper I

Journal of Applied Geophysics 123 (2015) 316–321

Contents lists available at ScienceDirect

Journal of Applied Geophysics

journal homepage: www.elsevier.com/locate/jappgeo

Measuring time-domain spectral induced polarization in the on-time: decreasing acquisition time and increasing signal-to-noise ratio

Per-Ivar Olsson [a],*, Torleif Dahlin [a], Gianluca Fiandaca [b], Esben Auken [b]

[a] Engineering Geology, Lund University, Sweden
[b] Department of Geosciences, Aarhus University, Denmark

ARTICLE INFO

Article history:
Received 16 April 2015
Received in revised form 28 July 2015
Accepted 26 August 2015
Available online 2 September 2015

Keywords:
Spectral
Induced polarization
Signal-to-noise ratio
SNR
Waveform
Duty cycle
Cole–Cole

ABSTRACT

Combined resistivity and time-domain direct current induced polarization (DCIP) measurements are traditionally carried out with a 50% duty cycle current waveform, taking the resistivity measurements during the on-time and the IP measurements during the off-time. One drawback with this method is that only half of the acquisition time is available for resistivity and IP measurements, respectively. In this paper, this limitation is solved by using a current injection with 100% duty cycle and also taking the IP measurements in the on-time. With numerical modelling of current waveforms with 50% and 100% duty cycles we show that the waveforms have comparable sensitivity for the spectral Cole–Cole parameters and that signal level is increased up to a factor of 2 if the 100% duty cycle waveform is used. The inversion of field data acquired with both waveforms confirms the modelling results and shows that it is possible to retrieve similar inversion models with either of the waveforms when inverting for the spectral Cole–Cole parameters with the waveform of the injected current included in the forward computations. Consequently, our results show that on-time measurements of IP can reduce the acquisition time by up to 50% and increase the signal-to-noise ratio by up to 100% almost without information loss. Our findings can contribute and have a large impact for DCIP surveys in general and especially for surveys where time and reliable data quality are important factors. Specifically, the findings are of value for DCIP surveys conducted in urban areas where anthropogenic noise is an issue and the heterogeneous subsurface demands time-consuming 3D acquisitions.

1. Introduction

Combined direct current (DC) resistivity and time-domain (TD) induced polarization (IP) measurements are traditionally carried out using a 50% duty cycle waveform for current injection, taking the resistivity measurements during the on-time and the IP measurements during the off-time. Recently, however, developments in time-domain hardware have made it possible to perform detailed monitoring and analysis of the measuring procedure of DCIP acquisition. As a result of this development, it has been suggested that a 100% duty cycle waveform could be used in time-domain IP, with the IP (spectral) information retrieved from the on-time (Dahlin and Leroux 2010). Furthermore, in frequency-domain, a 100% duty cycle waveform has been successfully used for measuring IP, although retrieving limited spectral information (Zonge et al. 2005, Zonge et al. 1972).

Alongside the hardware improvement, a corresponding development on the software side has taken place. Inversion algorithms that use the current waveform and the full IP decays for extracting the spectral IP content from TD data have been proposed (Fiandaca et al. 2012, 2013), with applications for landfill characterization (Gazoty et al. 2013, Gazoty et al. 2012a, Gazoty et al. 2012b) and for mapping CO2 transport (Doetsch et al. 2015a) and permafrost seasonal variations (Doetsch et al. 2015b).

For these applications, as well as for others, the use of a 100% duty cycle waveform for DCIP measurements will have substantial advantages compared with the traditionally used 50% duty cycle regarding acquisition time efficiency and signal level. These benefits are highly relevant for the applied DCIP surveys conducted by commercial companies where time and reliable data quality are important factors. In addition, DCIP surveys conducted in urban areas where anthropogenic noise sources are present and the heterogeneous subsurface demands time-consuming 3D acquisitions will have extra benefit from the 100% duty cycle waveform and on-time measurements of IP. To date, it has not been shown whether the 100% duty cycle waveform can be successfully used in TDIP measurements, nor if spectral information can be retrieved in the inversion.

This paper demonstrates that the use of a 100% duty cycle waveform and on-time measurements of the spectral IP information is possible for both synthetic and field DCIP cases. The aforementioned hardware and software developments are used for comparing 50% and 100% duty

---

* Corresponding author at: Teknisk Geologi, Lunds Tekniska Högskola, P.O. Box 118, SE-22100 Lund, Sweden.
E-mail address: per-ivar.olsson@tg.lth.se (P.-I. Olsson).

http://dx.doi.org/10.1016/j.jappgeo.2015.08.009
0926-9851/

cycle waveforms, both in terms of IP spectral information and signal to noise ratio. Section 2 introduces the 100% duty cycle waveform in details, followed by sections presenting results and discussion on the synthetic modelling and a field comparison. The paper ends with a brief conclusion.

2. 100% duty cycle

A step-response for an exemplary homogenous half-space Cole–Cole model was generated with the spectral forward response and inversion code Aarhusinv (Auken et al. 2014) and used for creating synthetic full-waveform data of the 50% and 100% duty cycle waveforms (Fig. 1) by the principle of superposition (Fiandaca et al. 2012).

It can be noted that for the 50% duty cycle waveform with IP measurements during the off-time, the measured IP response decays with time, while for the 100% duty cycle waveform with IP measurements during the on-time, the potential increases during the acquisition. For an easier comparison between the 50% and 100% signals, this paper uses the $V_{DC(j)}$ value (retrieved from a time period at the end of each pulse j) for defining the 100% IP decay for pulse j, $V_{IP100\%(j)}$, as the difference between the $V_{DC(j)}$ value and the measured IP response $V_{response(j)}$ (Eq. (1)):

$$V_{\mathrm{IP100\%}(j)}=V_{\mathrm{DC}(j)}\text{-}V_{\mathrm{response}(j)}. \tag{1}$$

The individual 100% IP decays derived with Eq. (1), $V_{IP100\%(j)}$, are averaged according to Eq. (2), making use of the negative or positive sign of the decays:

$$V_{\mathrm{IP100\%,average}}=\frac{1}{n_{\mathrm{pulses}}}\sum_{j=1}^{n_{\mathrm{pulses}}}(-1)^{j+1}\cdot\ V_{\mathrm{IP100\%}(j)}. \tag{2}$$

For the 50% duty cycle, a normalization of the IP response is traditionally achieved by dividing the IP response potential with the VDC value (VIP/VDC) and presenting the IP response in mV/V (note that this normalization does not define the “normalized chargeability” described for instance by Slater and Lesmes (2002), but is a common unit change). A corresponding normalization for the 100% duty cycle is also suggested in this paper through Eq. (3):

$$V_{\mathrm{IP100\%,normalized}}=\frac{V_{\mathrm{IP100\%,average}}\cdot n_{\mathrm{pulses}}}{V_{\mathrm{DC,average}}\cdot\left(2\cdot n_{\mathrm{pulses}}-1\right)} \tag{3}$$

where $V_{DC,\text{average}}$ represents the DC value averaged over all the pulses in analogy to Eq. (2). The normalization of Eq. (3) differs from the standard IP normalization by the presence of the $\frac{n_{\mathrm{pulses}}}{(2\cdot n_{\mathrm{pulses}}-1)}$ factor, which has been introduced in order to facilitate the numerical comparison of 50% and 100% IP duty cycles normalized data.

In fact, as can be seen in Fig. 2A, the magnitude of the chargeability for the 100% duty cycle waveform is initially almost twice the magnitude of the 50% duty cycle waveform if compared without normalization (presented in volt). This doubling is due to the superposition of the off-time IP decay of the 50% duty cycle waveform and the corresponding on-time IP build-up. With the 100% duty cycle waveform, these two responses are superimposed on each other and measured as one. Another way to look at this is to consider that the change in current causing the IP response is doubled when using the 100% duty cycle waveform instead of the 50% waveform for all the pulses except the first, which is initiated from the same current level (i.e. zero ampere, see Fig. 1). Considering that $V_{IP100\%,\ \text{normalized}}$ is computed from the IP responses averaged over all the pulses, the $\frac{n_{\mathrm{pulses}}}{(2\cdot n_{\mathrm{pulses}}-1)}$ factor in Eq. (3) standardizes the 100% duty cycle response to the current changes of the 50% duty cycle response.

As a result, with the normalization suggested in this paper (Eq. (3)), expressing the decays in terms of mV/V shows more similar starting and averaged magnitudes for the 50% and 100% IP decays (Fig. 2B). Despite the fact that the normalization proposed in Eq. (3) simplifies the comparison of the 50% and 100% signal levels, the shape of the IP curves differs significantly. In particular, the 100% IP decays defined through Eqs. (1), (2) and (3) are forced to small or negative data values at late times (Fig. 2), depending on the selected integration time for the V_{DC}-value and the last IP gate respectively, even though the corresponding 50% IP responses have not reached their minimum. In this paper, this effect is accounted for by the modelling/inversion software, which includes the current waveform, the definition of the DC integration time and the full IP decays in the computations (Fiandaca et al. 2013, Fiandaca et al. 2012).

When looking at the comparison of non-normalized 100% and 50% duty cycle data a final consideration can be drawn about the signal-to-noise ratio. In fact, the noise in IP data depends on the non-normalized signal level (Gazoty et al. 2013), and the almost doubled signal of the 100% duty cycle data can increase the signal-to-noise ratio by up to 100%.

3. Synthetic modelling

Forward modelling and sensitivity analysis of resistivity and the Cole–Cole parameters for both the 50% and the 100% duty cycle waveforms were carried out on a 1D synthetic model (Fiandaca et al. 2013, Fiandaca et al. 2012). The sensitivity, s, is computed through the covariance of the estimator error for linear mapping described by Tarantola

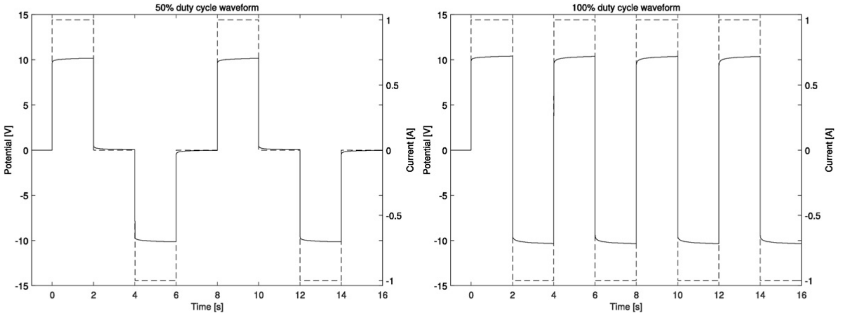

Fig. 1. Modelled waveform for the 50% (A) and 100% (B) duty cycle waveforms showing measured potential (solid line) and injected current (dashed line). Twice as many stacks are achieved with the 100% duty cycle compared with the 50% duty cycle with the same acquisition time.

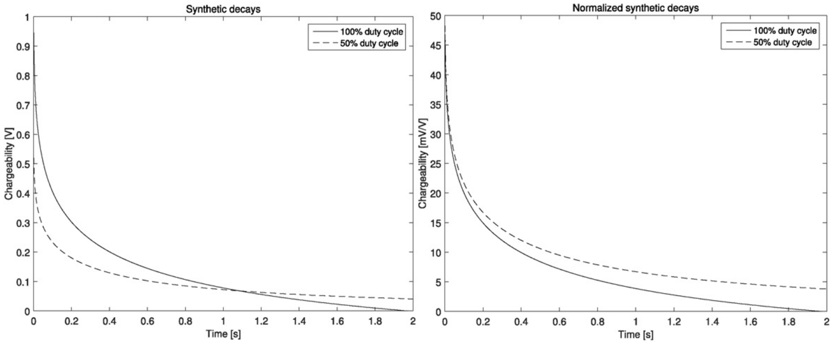

Fig. 2. Modelled IP decays for the 50% (dashed line) and 100% (solid line) duty cycle waveform shown with (B) and without (A) normalization. The normalization of the 100% duty cycle decay was done according to Eq. (3) and $n_{\text{pulses}} = 8$, corresponding to the number of modelled pulses (see Fig. 1B). The decays are modelled with Cole–Cole parameters: rho = 50 Ωm, $m_0 = 100$ mV/V, $\tau = 0.5$ s and $C = 0.3$.

and Valette (1982) and represents the relative uncertainty on the model parameters p (because the analysis is performed on the logarithm of the model parameters):

$$p/s \le p \le p \cdot s.$$

A synthetic three layer subsurface model (Table 1), with parameter ranges/contrasts similar to the ones found in the field example described in the next section, was used for the forward modelling of a Schlumberger vertical sounding with log-increasing electrode spacing and IP gate lengths. To emulate field conditions, a noise model identical to the one characterizing the field data was chosen for the sensitivity analysis. In particular, a relative standard deviation of 2% for the DC data and 10% for the IP data were used, together with a voltage dependent noise (Gazoty et al. 2013; Zhou and Dahlin 2003) that better describes the effect of the signal level on the data uncertainty. The voltage dependent noise model was controlled by a nominal voltage noise threshold V_{noise}, defined for a nominal integration time $Nominal_{\text{gatelength}}$ and stack size n equal to one, and defined as:

$$\sigma_{DC} = \frac{V_{\text{noise}}}{V_{DC}} \cdot \sqrt{\frac{Nominal_{\text{gatelength}}}{DC_{\text{gatelength}}} \cdot \frac{1}{n}} \tag{4}$$

$$\sigma_{IP} = \frac{V_{\text{noise}}}{V_{IP}} \cdot \sqrt{\frac{Nominal_{\text{gatelength}}}{IP_{\text{gatelength}}} \cdot \frac{1}{n}}. \tag{5}$$

A voltage threshold $V_{noise} = 0.2$ mV with $Nominal_{\text{gatelength}} = 0.01$ s was used in the simulations.

The forward modelling and 1D sensitivity analysis was carried out by means of both of the waveforms and four different acquisition cases: two cases with the same on-time ($T_{\text{on}} = 4$ s) and amount of stacks ($n = 4$) but with different waveforms (50% and 100% duty cycles) and two other cases where either the on-time either the stacks were doubled for the 100% duty cycle waveform. In theory, the latter two cases give the same total duration of the acquisition as for the 50% duty cycle waveform (Table 2). Table 2 shows that the sensitivity for all model parameters is comparable for all four acquisition cases, except for the relaxation time of layer two ($\tau - 2$) for which the first (50% duty cycle, $T_{\text{on}} = 4$ s, $n = 4$) and that the second last (100% duty cycle, $T_{\text{on}} = 8$ s, $n = 4$) cases are more sensitive compared with the others.

Table 1
Layer parameters used for the 1D subsurface model.

Layer	Thickness (m)	ρ (Ωm)	m_0 (mV/V)	τ (s)	c (−)
1	8	250	40	1	0.3
2	14	500	100	2	0.5
3	∞	500	40	1	0.5

4. Field example

The field data were acquired at a farmland with Quaternary deposits of clayey till overlaying a bedrock of Silurian shale. A known dolerite dike intruding the shale provided a chargeable IP structure for the experiment. The DCIP profile (157.5 m, 64 electrodes with a spacing of 2.5 m) was centred on top of the known IP anomaly and retrieved using a multiple gradient array protocol (Dahlin and Zhou 2006) with acid grade stainless steel electrodes and the Abem Terrameter LS instrument. This instrument continuously adapts the output voltage to keep a constant current with an accuracy of 0.4% (Abem 2011), and together with its capability of full-waveform acquisition is particularly well suited for this experiment. Separated cables were used for transmitting current and measuring potentials to reduce the effect of capacitive coupling and improve the IP data quality (Dahlin and Leroux 2012). The electrode contact resistance was measured for all electrodes with a mean value of 220 Ω and a variation coefficient of approximately 45%.

Both the 50% and the 100% duty cycle waveforms were used for DCIP measurements on the field setup. Except for the waveform duty cycle, all other settings were kept equal for the acquisitions: 1015 quadrupoles, 4 s on-time of current injection and 3 full stacks. This resulted in a total acquisition time of 154 min for the 50% duty cycle and 88 min for the 100% duty cycle, a reduction in acquisition time of approximately 43% for the 100% duty cycle waveform. The reason for the reduction not reaching the theoretical 50% (only considering the duration of the waveforms) is that the instrument performs a number of test pulses prior to each current injection. These test pulses are part of the system that enables the instrument to maintain a constant current throughout the injection. In this study, these test pulses were not included in the full waveform modelling.

To get an accurate estimation of the IP response, the background potential variation during a current injection sequence needs to be accounted for. This is also essential for DC resistivity measurement and is commonly handled by measuring and averaging data from a positive–double negative–positive type duty cycle which acts as a filter that removes linear variation (Dahlin 2000), but it should be noted that a higher degree approach may be required in order to recover the more subtle spectral IP information. In this paper, a second order polynomial was adapted to the V_{DC}-values of the stacks and the non-constant terms

Table 2
Sensitivity analysis for both waveforms with same on-time and doubled on-time for the 100% duty cycle. Relaxation time of layer two ($\tau-2$) for the first and third acquisition cases are indicated with bold font.

Duty cycle	T_{on} (s)	n $(-)$	$\rho-1$ (Ωm)	$\rho-2$ (Ωm)	$\rho-3$ (Ωm)	m_0-1 (mV/V)	m_0-2 (mV/V)	m_0-3 (mV/V)	$\tau-1$ (s)	$\tau-2$ (s)	$\tau-3$ (s)	$c-1$ $(-)$	$c-2$ $(-)$	$c-3$ $(-)$
50%	4	4	1.015	1.052	1.014	1.40	1.15	1.13	1.54	**1.16**	1.16	1.40	1.12	1.13
100%	4	4	1.015	1.052	1.014	1.47	1.17	1.16	1.54	1.27	1.17	1.47	1.14	1.16
100%	8	4	1.014	1.051	1.014	1.39	1.14	1.12	1.58	**1.14**	1.18	1.39	1.11	1.12
100%	4	8	1.015	1.052	1.014	1.47	1.17	1.16	1.54	1.27	1.16	1.47	1.14	1.15

of this polynomial was used to correct the full waveform recording of measured potential.

Fig. 3 shows field data for both waveforms as apparent resistivity (Fig. 3A and C) and apparent chargeability (IP gate number 5, Fig. 3B and D) pseudosections. The resistivity data show comparable, in terms of spatial distribution and apparent resistivity values, pseudosections for both waveforms. The apparent chargeability pseudosections also have similar spatial distribution but the apparent chargeability section for the 100% duty cycle waveform shows slightly lower values than the 50% duty cycle waveform, when expressed as mV/V. The difference in magnitude of the apparent chargeability, which is also visible in the synthetic IP responses (Fig. 2B), can be explained by the different shapes of the 100% duty cycle waveform at late times, as discussed in Section 2.

Inversion of the field data shown in Fig. 3 were preformed for the spectral Cole–Cole parameters using the Aarhusinv code. The inversions were carried out with L1 model weights using the same inversion settings (noise model and vertical/horizontal weights) for both waveforms. This gave a final data misfit of 1.5 and 1.4 for the 50% and 100% duty cycle data respectively, when using a relative standard deviation of 2% for the DC data, 10% for the IP data and a voltage noise threshold of 0.2 mV.

Fig. 4 shows that the inversion models for the field data acquired with the two waveforms have comparable values for all model parameters and similar data misfit. The geometry of the parameter value distribution in the final inversion models is quite simple but the performance of the 50% and 100% duty cycle waveforms is expected to be comparable also when applied at environments with a more complex subsurface geometry. Similarly, are the performance of the waveforms expected to be comparable also in noiseier field conditions or possibly have better performance with the 100% duty cycle waveform due to higher signal-to-noise ratio? (See Section 2).

Fig. 5 shows the data fit for the quadrupoles with lateral focus (i.e. horizontal position of median sensitivity) corresponding to the middle of the profile (Fig. 4). Similar to what is shown by the synthetic decays (Fig. 2), the acquired field data for the 100% duty cycle waveform are closer to zero for the later gates compared with the 50% duty cycle waveform.

The data acquired from the field tests (Figs. 3 and 5) generally show that the IP decays for the 50% and 100% duty cycle waveforms are different. As discussed above, this difference is in accordance with the synthetic modelling and depends on how the 100% duty cycle IP decay is defined. With an inversion software that includes the injected current waveform and the definitions for the 100% duty cycle IP decay, it is still possible to retrieve an inversion model from the 100% duty cycle data (Fig. 4B) that is similar to the inversion model from the 50% duty cycle waveform data (Fig. 4A).

5. Conclusions

Our results support that the approach of using a 100% duty cycle square waveform for current injection and measuring the IP response during the current on-time is practically applicable. We also show that the measuring time can be substantially reduced by the use of this method and that the signal-to-noise ratio will generally increase.

The results contribute to the usage of commercial IP measurements within areas where the time pressure on projects due to economic constraints is dominant. This is usually the case in engineering and environmental projects but decreasing the total measurement time and improving signal-to-noise ratio are beneficial for all DCIP surveys. Thus, an implementation of a commercial system which makes use of a 100% duty cycle and measures IP during the on-time could have several practical benefits. For example, it may encourage operators to make use of 3D-measurements which generally can be time demanding, to make use of more stacks in noisy environments to get better data quality or to increase the on-time at field sites where long time-constants are expected for the IP decays (such as for example landfills) to get additional spectral information.

The 100% duty cycle and on-time IP measurements described in this paper could be implemented as routine use in DCIP instruments and processing procedures. To actualize this, the instrument used need to

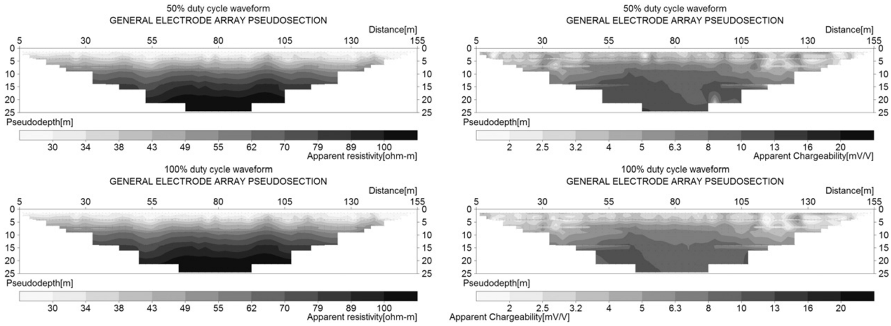

Fig. 3. DC pseudosections (A and C) and IP gate 5 (gate width of 143 ms and centre gate time of 376.5 ms) for the 50% (B) and the 100% (D) duty cycle waveform.

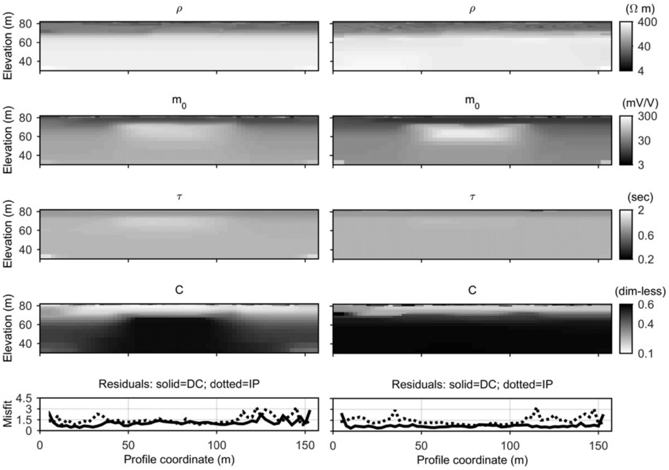

Fig. 4. Inverted sections and data misfit for field data acquired with the 50% (A) and 100% (B) duty cycle waveform.

be able to record full waveform information or be able to gate the data directly during the on-time. The instrument should also be able to keep a stable current waveform. If this is not possible, the waveform of the injected current needs to be fully described in the inversion software and included in the forward computations. These types of inversion software are also advantageous for comparing results from different waveforms (50% duty cycle versus 100% duty cycle).

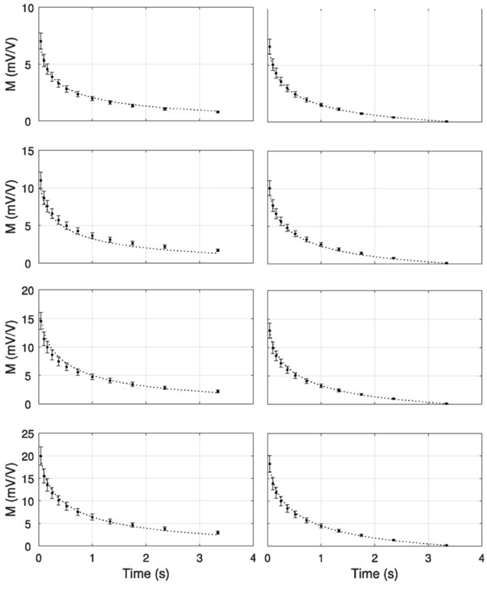

Fig. 5. IP data (points) with error bars (vertical lines) and corresponding forward response (dashed line) for the 50% (A) and 100% (B) duty cycle waveforms. Data shown represents the middle of the field array with increasing pseudo depth from top to bottom.

Acknowledgements

Funding for the work was provided by Swedish Research Council Formas — The Swedish Research Council for Environment, Agricultural Sciences and Spatial Planning, (ref. 2012-1931), BeFo — Swedish Rock Engineering Research Foundation, (ref. 331) and SBUF — The Development Fund of the Swedish Construction Industry, (ref. 12719). The project is part of the Geoinfra-TRUST framework (http://www.trust-geoinfra.se/).

References

Abem, 2011. Terrameter LS Product Leaflet [www document]. URL http://www.abem.se/support/downloads/technical-specifications/terrameter-ls-leaflet-20111116 (accessed 5.27.14).

Auken, E., Christiansen, A.V., Kirkegaard, C., Fiandaca, G., Schamper, C., Behroozmand, A.A., Binley, A., Nielsen, E., Effersø, F., Christensen, N.B., Sørensen, K., Foged, N., Vignoli, G., 2014. An overview of a highly versatile forward and stable inverse algorithm for airborne, ground-based and borehole electromagnetic and electric data. Explor. Geophys. http://dx.doi.org/10.1071/EG13097.

Dahlin, T., 2000. Short note on electrode charge-up effects in DC resistivity data acquisition using multi-electrode arrays. Geophys. Prospect. 48, 181–187. http://dx.doi.org/10.1046/j.1365-2478.2000.00172.x.

Dahlin, T., Leroux, V., 2010. Full wave form time-domain IP data acquisition, in: 16th European Meeting of Environmental and Engineering Geophysics. doi:http://dx.doi.org/10.3997/2214-4609.20144884

Dahlin, T., Leroux, V., 2012. Improvement in time-domain induced polarization data quality with multi-electrode systems by separating current and potential cables. Near Surf. Geophys. 10, 545–656. http://dx.doi.org/10.3997/1873-0604.2012028.

Dahlin, T., Zhou, B., 2006. Multiple-gradient array measurements for multichannel 2D resistivity imaging. Near Surf. Geophys. 4, 113–123. http://dx.doi.org/10.3997/1873-0604.2005037.

Doetsch, J., Fiandaca, G., Auken, E., Christiansen, A.V., Cahill, A.G., 2015a. Field-scale time-domain spectral induced polarization monitoring of geochemical changes induced by injected CO_2 in a shallow aquifer. Geophysics 16, 10294. http://dx.doi.org/10.1190/geo2014-0315.1.

Doetsch, J., Ingeman-Nielsen, T., Christiansen, A.V., Fiandaca, G., Auken, E., Elberling, B., 2015b. Direct current (DC) resistivity and induced polarization (IP) monitoring of active layer dynamics at high temporal resolution. Cold Reg. Sci. Technol. http://dx.doi.org/10.1016/j.coldregions.2015.07.002.

Fiandaca, G., Auken, E., Christiansen, A.V., Gazoty, A., 2012. Time-domain-induced polarization: full-decay forward modeling and 1D laterally constrained inversion of Cole–Cole parameters. Geophysics 77, E213–E225. http://dx.doi.org/10.1190/geo2011-0217.1.

Fiandaca, G., Ramm, J., Binley, A., Gazoty, A., Christiansen, A.V., Auken, E., 2013. Resolving spectral information from time domain induced polarization data through 2-D inversion. Geophys. J. Int. 192, 631–646. http://dx.doi.org/10.1093/gji/ggs060.

Gazoty, A., Fiandaca, G., Pedersen, J., Auken, E., Christiansen, A. V, 2012a. Mapping of landfills using time-domain spectral induced polarization data: the Eskelund case study. Near Surf. Geophys. 10, 575–586. doi:http://dx.doi.org/10.3997/1873-0604.2012046

Gazoty, A., Fiandaca, G., Pedersen, J., Auken, E., Christiansen, A. V, 2013. Data repeatability and acquisition techniques for time-domain spectral induced polarization. Near Surf. Geophys. 391–406. doi:http://dx.doi.org/10.3997/1873-0604.2013013

Gazoty, A., Fiandaca, G., Pedersen, J., Auken, E., Christiansen, A.V., Pedersen, J.K., 2012b. Application of time domain induced polarization to the mapping of lithotypes in a landfill site. Hydrol. Earth Syst. Sci. 16, 1793–1804. http://dx.doi.org/10.5194/hess-16-1793-2012.

Slater, L.D., Lesmes, D., 2002. IP interpretation in environmental investigations. Geophysics 67, 77. http://dx.doi.org/10.1190/1.1451353.

Tarantola, A., Valette, B., 1982. Generalized nonlinear inverse problems solved using the least squares criterion. Rev. Geophys. http://dx.doi.org/10.1029/RG020i002p00219.

Zhou, B., Dahlin, T., 2003. Properties and effects of measurement errors on 2D resistivity imaging surveying. Near Surf. Geophys. 1, 105–117. http://dx.doi.org/10.3997/1873-0604.2003001.

Zonge, K.L., Sauck, W.A., Sumner, J.S., 1972. Comparison of time, frequency, and phase measurements in induced polarization*. Geophys. Prospect. 20, 626–648. http://dx.doi.org/10.1111/j.1365-2478.1972.tb00658.x.

Zonge, K.L., Wynn, J., Urquhart, S., 2005. 9. Resistivity, induced polarization, and complex resistivity. Near-surface Geophysics, pp. 265–300 http://dx.doi.org/10.1190/1.9781560801719.ch9.

Paper II

Geophysical Journal International

Geophys. J. Int. (2016) **207,** 774–784 doi: 10.1093/gji/ggw260
Advance Access publication 2016 August 20
GJI Marine geosciences and applied geophysics

Doubling the spectrum of time-domain induced polarization by harmonic de-noising, drift correction, spike removal, tapered gating and data uncertainty estimation

Per-Ivar Olsson,[1] Gianluca Fiandaca,[2] Jakob Juul Larsen,[3] Torleif Dahlin[1] and Esben Auken[2]

[1] *Teknisk Geologi, Lunds Tekniska Högskola, P.O. Box 118, SE-22100 Lund, Sweden. E-mail: per-ivar.olsson@tg.lth.se*
[2] *HydroGeophysics Group, Department of Geoscience, Aarhus University, Denmark*
[3] *Department of Engineering, Aarhus University, Finlandsgade 22, 8200 Aarhus N, Denmark*

Accepted 2016 July 11. Received 2016 July 8; in original form 2016 April 26

SUMMARY

The extraction of spectral information in the inversion process of time-domain (TD) induced polarization (IP) data is changing the use of the TDIP method. Data interpretation is evolving from a qualitative description of the subsurface, able only to discriminate the presence of contrasts in chargeability parameters, towards a quantitative analysis of the investigated media, which allows for detailed soil- and rock-type characterization. Two major limitations restrict the extraction of the spectral information of TDIP data in the field: (i) the difficulty of acquiring reliable early-time measurements in the millisecond range and (ii) the self-potential background drift in the measured potentials distorting the shape of the late-time IP responses, in the second range. Recent developments in TDIP acquisition equipment have given access to full-waveform recordings of measured potentials and transmitted current, opening for a breakthrough in data processing. For measuring at early times, we developed a new method for removing the significant noise from power lines contained in the data through a model-based approach, localizing the fundamental frequency of the power-line signal in the full-waveform IP recordings. By this, we cancel both the fundamental signal and its harmonics. Furthermore, an efficient processing scheme for identifying and removing spikes in TDIP data was developed. The noise cancellation and the de-spiking allow the use of earlier and narrower gates, down to a few milliseconds after the current turn-off. In addition, tapered windows are used in the final gating of IP data, allowing the use of wider and overlapping gates for higher noise suppression with minimal distortion of the signal. For measuring at late times, we have developed an algorithm for removal of the self-potential drift. Usually constant or linear drift-removal algorithms are used, but these algorithms often fail in removing the background potentials present when the electrodes used for potential readings are previously used for current injection, also for simple contact resistance measurements. We developed a drift-removal scheme that models the polarization effect and efficiently allows for preserving the shape of the IP responses at late times. Uncertainty estimates are essential in the inversion of IP data. Therefore, in the final step of the data processing, we estimate the data standard deviation based on the data variability within the IP gates and the misfit of the background drift removal Overall, the removal of harmonic noise, spikes, self-potential drift, tapered windowing and the uncertainty estimation allows for doubling the usable range of TDIP data to almost four decades in time (corresponding to four decades in frequency), which will significantly advance the applicability of the IP method.

Key words: Time-series analysis; Fourier analysis; Numerical approximations and analysis; Tomography; Electrical properties.

1 INTRODUCTION

Recently, the interpretation and inversion of time-domain induced polarization (TDIP) data has changed as research is moving from only inverting for the integral changeability to also consider the spectral information and inverting for the full induced polarization (IP) response curves (Oldenburg 1997; Hönig & Tezkan 2007; Fiandaca *et al*. 2012, 2013; Auken *et al*. 2015). Several examples of spectral TDIP applications for different purposes have been presented (Gazoty *et al*. 2012a, 2013b; Chongo *et al*. 2015; Fiandaca *et al*. 2015; Johansson *et al*. 2015; Doetsch *et al*. 2015a,b). Furthermore, efforts have been made to achieve faster acquisitions and a better signal-to-noise ratio (SNR) by using a 100 per cent duty cycle current waveform, without current off-time (Olsson *et al*. 2015). However, drawbacks still remain for the spectral TDIP measurements, especially its limited spectral information content compared to, for example, laboratory frequency-domain spectral IP measurements (Revil *et al*. 2015). To date, only limited work has been done on increasing the spectral information content in TDIP measurement data even though recent developments in TDIP acquisition equipment have enabled access to full-waveform recordings of measured potentials and transmitted current (e.g. the Terrameter LS instrument by ABEM and the Elrec Pro instrument by Iris Instruments provide such data).

Two major limitations restrict the extraction of the spectral information of TDIP data in the field: (i) the difficulty of acquiring reliable early-time measurements in the millisecond range due to the presence of spikes and harmonic noise originating from anthropogenic sources and (ii) the self-potential background drift in the measured potentials distorting the shape of the late-time IP responses, in the second range.

Background drift in TDIP data can have multiple origins, for example, natural potential difference in the subsurface, electrochemical electrode polarization (if not using non-polarizable electrodes) and current-induced electrode polarization (if using the same electrodes for injecting current and measuring potentials). The current-induced electrode polarization drift can be orders of magnitude larger than the signal (Dahlin 2000), and thus it is crucial to compensate for this background drift in order to accurately retrieve the shape of the IP response and be able to extract the spectral IP information from TDIP measurement of the subsurface. The drift is traditionally corrected with a linear approximation (Dahlin *et al*. 2002; Peter-Borie *et al*. 2011), which for DC and integral chargeability measurements is often sufficient, but when evaluating the spectral IP information, a more accurate approximation is needed. This paper presents an improved background drift estimation method using a Cole–Cole model (Cole & Cole 1941; Pelton *et al*. 1978). This model is known accurately to describe polarization effects and it is capable of handling both linear (with long Cole–Cole time constants) and more complex non-linear drift cases such as the current-induced electrode polarization.

Spikes originating from anthropogenic sources such as electric fences for livestock management are registered by TDIP measurements. These spikes cause problems when extracting IP information, and especially spectral IP, from measured field data. This paper presents a novel and efficient processing scheme for enhancing and identifying the spikes with a series of filters applied to the raw potential signal and by implementing a flexible and data-driven threshold variable for spike identification.

Harmonic noise originates from the power supply sources oscillating at a base frequency (e.g. 50 Hz or 60 Hz) and harmonics of this base frequency. In TDIP processing today, this is handled by introducing hardware low-pass filters and/or applying rectangular gating over full period(s) of the known base frequency (e.g. 1/50 or 1/60 s). However, usage of low-pass filters or long gates cause a loss of early-time IP response information, making it difficult to resolve early-time and high-frequency spectral IP parameters. This is even more severe when the field measurements are conducted close to electric railways in countries (e.g. Austria, Germany, Norway, Sweden, Switzerland and USA) where the frequency of the power supply is even lower ($16\ ^2/_3$ or 25 Hz). This requires even longer gates to suppress the harmonic noise or a lower cut-off frequency of hardware, a low-pass filter. Deo & Cull (2015) suggested the use of a wavelet technique for de-noising TDIP data, but without retrieving IP response information at early times or high frequencies. This paper employs another method for handling the noise, which allows for use of these early times: for the first time in TDIP, a well-known method used in other geophysical disciplines for cancelling harmonic noise (Butler & Russell 1993, 2003; Saucier *et al*. 2006; Larsen *et al*. 2013) is successfully applied on full waveform data. This method models and subtracts the harmonic noise from raw full-waveform potential data. Hence, it is possible to use gate widths that are independent of the period of the harmonic noise. In reality, the earliest usable gate is then limited to when the transient electromagnetic (EM) voltage is negligible in relation to the IP voltage, considering that the EM effect is not usually modeled in the forward response. The duration of the EM effect depends on the electrode separation and the impedance of the subsurface (Zonge *et al*. 2005). Other studies have suggested methods for handling/removing the EM coupling effects (Dey & Morrison 1973; Johnson 1984; Routh & Oldenburg 2001) but this is not within of the scope of this study.

In addition to the improved background drift removal, spike removal and harmonic de-noising, this study also describes a tapered gating scheme, which is not conventional in IP applications, but has been used for decades in other geophysical methods (e.g. transient EM) for suppressing high-frequency noise (Macnae *et al*. 1984; Mccracken *et al*. 1986). Furthermore, an estimation of the data standard deviation (STD) based on the data variability within the gates and on the quality of the background drift removal is presented.

2 DATA ACQUISITION

Full-waveform data are very useful to facilitate digital signal processing. The required sampling rate for the full waveform depends mainly on the desired width of the shortest gate and how close it should be to the current switch off. Another consideration, which is related to the input and filter characteristics of the instrument, is that the sampling rate needs to be sufficiently high to avoid aliasing. All data presented were acquired with a 50 per cent duty cycle current waveform and 4 s on- and off-time using a modified ABEM Terrameter LS instrument for transmitting current and measuring potentials. The instrument operates at a sampling rate of 30 kHz and applies digital filtering and averaging (Abem 2011). We used a data rate of 3750 Hz, corresponding to approximately 0.267 ms per sample. Laboratory tests with frequency sweep of sinusoidal input signals showed that the in-built low-pass filter of the instrument was insufficient and would allow for severe aliasing at this sampling rate. Consequently, the instrument input filters were rebuilt by implementing fourth-order Butterworth filters with a cut-off frequency of 1.5 kHz. The instrument data rate was chosen for being able to have the first IP gate 1 ms after the turn-off of the current pulse considering that, depending on electrode separation and subsurface resistivity (Zonge *et al.* 2005), earlier gates would likely suffer from EM effects which are not within the scope of this study.

The TDIP data were acquired along a profile (74 m, 38 acid-grade stainless steel electrodes with spacing of 2 m) laid out on a grass field in the Aarhus University campus (Denmark), with presence of multiple noise sources common in urban environments. The power-line frequency is 50 Hz (corresponding to a fundamental period of 20 ms) in all examples.

3 SIGNAL PROCESSING

In the field, the measured potential is composed of the sum of multiple, known and unknown, sources. To get an accurate determination of the potential response u_{response}, it is essential to determine and compensate for as many of these sources as possible. This is expressed as:

$$u_{\text{measured}}(n) = u_{\text{response}}(n) + u_{\text{drift}}(n) + u_{\text{spikes}}(n) + u_{\text{harmonic noise}}(n) + u_{\text{random}}(n) \quad (1)$$

where, for each sample index n, u_{measured} is the measured potential, u_{response} is the potential response from the current injection, u_{drift} is the background drift potential, $u_{\text{harmonic noise}}$ is the harmonic noise from AC power supplies and u_{random} is the potential from other random and unknown sources. The component u_{random} represents random background noise and is most efficiently handled by gating and stacking. The known noise sources in eq. (1) (u_{drift}, u_{spikes} and $u_{\text{harmonic noise}}$) can be handled separately and removed in a sequential manner with the processing scheme described in this study. A method for estimating the uncertainty of the processed data is presented also. For continuity, the different parts of the signal processing scheme in this section are presented using one full-waveform potential (and current) recording acquired as described in the previous section. However, due to absence of anthropogenic spikes in this recording, another full waveform acquired in a rural area in western Denmark is used for the de-spiking example in Fig. 3.

3.1 Linear drift removal, stacking and rectangular gating

The recording of full-waveform data allows for stacking and gating of the data originating from different current pulses with any distribution of the IP gates after acquisition, the only limitation being the acquisition sampling rate. In this study, extraction of the potential response down to 1 ms after the current turn-off is desired. This is achieved by using a delay of 1 ms after the current turn-off and applying a log-increasing gating scheme, which compensates for changes of SNR throughout the IP response (Gazoty *et al.* 2013). When the gates are wide enough (i.e. equal to or wider than 20 ms) the gate widths are rounded off to multiples of the period of the harmonic noise (Table 1, seven gates per decade).

The stacking and gating procedure classically used for retrieving the IP responses from the full-waveform data is carried out according to:

$$u_{\text{IP,stacked}}(k) = \frac{1}{N_{\text{pulses}}} \sum_{j=1}^{N_{\text{pulses}}} (-1)^{j+1} u_{\text{processed}}(k + S_{\text{IP}}(j) - 1) \quad (2)$$

$$u_{\text{IP,gated}}(m) = \frac{1}{N_{\text{samples}}(m)} \sum_{i=1}^{N_{\text{samples}}(m)} u_{\text{IP,stacked}}\left(i + S_{\text{gate}}(m) - 1\right) \quad (3)$$

where $u_{\text{IP,stacked}}$ and $u_{\text{IP,gated}}$ are the stacked and gated potential respectively; k is the sample index of the stacked IP response; m is the gate index; N_{pulses} and $N_{\text{samples}(m)}$ are the number of pulses and gate samples, respectively; $u_{\text{processed}}$ represents the measured potential after some processing (typically after drift correction); $S_{\text{IP}}(j)$ is the first sample index of the IP signal for pulse number j and $S_{\text{gate}}(m)$ is the first sample index in gate m. Eq. (2) is thus the stacking procedure that makes use of the negative and positive signs of the pulses and eq. (3) defines rectangular gates on the signal.

In analogy to eq. (3), the DC potential, $u_{\text{DC,gated}}$ is averaged over all pulses and used for normalizing the IP response according to eq. (4):

$$u_{\text{IP,normalized}}(m) = \frac{u_{\text{IP,gated}}(m)}{u_{\text{DC,gated}}}. \quad (4)$$

Fig. 1 shows both the full-waveform acquisition (top) and the corresponding decay (bottom) for an exemplary recording of the data measured along the test profile at the Aarhus Campus. The full-waveform potential clearly shows the presence of u_{drift}, u_{spikes}, $u_{\text{harmonic noise}}$ and u_{random} superposed to u_{response}. In fact, the signal presents an overall increasing trend (the drift), big positive and negative variations at the current turn-on and turn-off, spikes (both in the potential and current recording) and fast oscillations that mask completely the IP response (harmonic and random noise).

Traditionally, the drift is removed using synchronous detection designed so it either removes static shifts, or if a bit more advanced, linear trends (Dahlin *et al.* 2002; Peter-Borie *et al.* 2011), while the other noise sources are handled by the stacking/gating procedure.

In Fig. 1 (bottom), two responses are shown: the resulting IP response (green) after gating and stacking the full-waveform potential according to eqs (3) and (4) and Table 1, as well as the IP response retrieved using the default gating in the instrument with gates multiple of 20 ms (magenta). In both cases, the signal is corrected for linear drift $u_{\text{drift}}(n) = a * n + b$. The re-gated IP response shows similar magnitude as the instrument supplied after approximately 60 ms, when the gates for both responses are multiples of 20 ms. Contrastingly, it exhibits an erratic behaviour until 60 ms since the gates are not 20 ms multiples and the harmonic noise is not suppressed. Clearly, the harmonic noise needs to be assessed in order to be able to use gates, which are shorter than 20 ms. Also note that the tail of both IP responses is increasing at the end. This paper will show that this is a result of poor performance of the background drift removal when applying a linear drift model.

3.2 Cole–Cole model-based drift removal

The background drift, u_{drift}, is made up of two components, self-potentials in the Earth (Dahlin *et al.* 2002) and electrode polarization (Dahlin 2000). While the linear drift removal works reasonably well for compensation of self-potentials, it is not optimal for compensation of potentials due to electrode polarization. The electrode polarization is typically attributed to charge buildup on the interface between the conducting metal of the electrode and the surrounding ground of less conductance. These effects can be orders of magnitude larger than the IP signal, when an electrode is used for transmitting current, and are clearly not linear (Dahlin 2000). Electrode polarization is hard to avoid due to difficulties of designing meaningful measurement sequences that do not use electrodes for potential measurements shortly after they have been

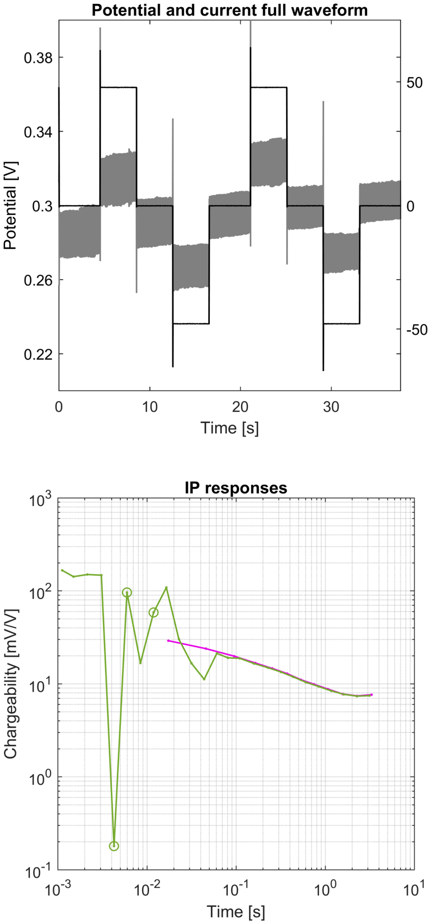

Figure 1. Top: 50 per cent duty cycle raw full-waveform potential data (grey) and transmitted current (black). Bottom: IP response binned with gates that are multiples of 20 ms and delay of 10 ms (magenta, instrument output) and re-gated IP response according to Table 1 and linear drift removal (green data points indicated by o-marker are negative). Note that the green response exhibits erratic behaviour in the beginning, while the gates are not multiples of the time period of the harmonic noise. Also note that the tail of both IP responses shows an increase in chargeability.

used for current injections. Electrode contact tests performed before initiating the TDIP measurements are also an important source for electrode polarization. Consequently, for compensating the background drift it is important to use a drift model that accounts for the polarization phenomenon at the electrodes. In this study, we use a drift model (eq. 5) based on the Cole–Cole model (Cole & Cole 1941; Pelton *et al.* 1978), because the Cole–Cole model well describes depolarization phenomenon and several tests on field data from different surveys proved the efficiency of the u_{drift} model of eq. (5) in removing the drift:

$$u_{\text{drift}}(n) = m_0 \sum_{j=0}^{\infty} (-1)^j \left(\frac{n}{\tau f_s}\right)^{jc} \Gamma(1+jc)^{-1} + d \qquad (5)$$

where n represents the sample index; d is an offset constant; f_s is the sampling frequency; m_0 is the drift amplitude; τ is the Cole–Cole relaxation time; c is the Cole–Cole frequency exponent and Γ is Euler's Gamma function $\Gamma(x) = \int_0^\infty y^{x-1} e^{-y} dy$. Thus, eq. (5) corresponds to the Cole–Cole model as described by Pelton *et al.* (1978) with an added offset constant d.

The fitting of the drift model parameters is conducted on a gated subset of the full-waveform signal (u_{subset}). The width of the gating window is set to a full period (e.g. 20 ms for 50 Hz) of the fundamental frequency of the power-line harmonic so that the harmonic oscillations are suppressed.

$$u_{\text{subset}}(i) = \frac{1}{N_{f0\ \text{samples}}} \sum_{j=1}^{N_{f0\ \text{samples}}} u_{\text{measured}}\left(S_{\text{subset}}(i) + j - 1\right) \qquad (6)$$

where $u_{\text{subset}}(i)$ is the ith datum of the drift subset, $N_{f0\ \text{samples}}$ is the number of samples corresponding to the time period of the fundamental frequency and $S_{\text{subset}}(i)$ represents the first sample index used for gating u_{measured} and retrieving $u_{\text{subset}}(i)$. For increased computing speed when fitting the u_{drift} model parameters, and since the drift is smoothly varying, the S_{subset} variable is selected so that u_{subset} only consists of 4–10 points per second.

Since the IP responses themselves create an offset from the drift baseline, the drift model fit is done on a subset of the gated signal (u_{subset}, eq. 6). This subset is taken from the end of the off-time period for the 50 per cent duty cycle (orange x-marker, Fig. 2) where the effect of the IP responses on the drift baseline is smaller. For the 100 per cent duty-cycle current waveform, the subset is taken at the end of the on-time period. Even if there is residual IP signal (u_{response}) in u_{measured} where the u_{subset} is taken, the alternating positive–negative character of the current pulses will cause also the IP offset to alternate around the drift baseline. Owing to this, the drift estimate method is not significantly sensitive to residual IP signal in the u_{subset} data, since the fit of u_{drift} goes in between the positive–negative residual IP signals.

For the drift subset data used in this paper, u_{subset} (orange x-marker, Fig. 2) corresponds to 4 points per second for the last 40 per cent of each off-time period, except for the first off-time period (before the first pulse) where it corresponds to the last 70 per cent.

Fig. 2 shows examples of estimated drift models, as well as the resulting IP responses after gating and stacking. In the drift model and full-waveform potential plot (Fig. 2, top), there is a significant difference between the linear fit model (green) and the data actually used for estimating the drift (orange x-markers). Clearly, the linear model is not sufficient for describing the drift accurately and it gives increasing chargeability values for the late gates (green line; Fig. 2, bottom). During the off-time, the potential should monotonically tend to 0 at late times independent of subsurface chargeability distribution in time and space. Contrastingly to the linear drift model, the Cole–Cole model (blue line; Fig. 2, bottom) shows a good fit of the drift and the resulting IP response does not show a chargeability increase at late times. Consequently, it is clear that a linear drift model gives incorrect IP responses at late times and that a more advanced drift model such as the Cole–Cole model is necessary. It is also clear that especially the gates at late times, with low 'signal-to-drift' ratios, are affected by the drift model accuracy.

Table 1. Duration of delay time and IP gates for the processed field data corresponding to seven gates per decade. Note that gates from 13 and higher have widths which are multiples of 20 ms.

Gate number	**Delay**	**1**	**2**	**3**	**4**	**5**	**6**	**7**	**8**	**9**	**10**	**11**	**12**
Width (ms)	1	0.26	0.53	0.80	1.06	1.33	2.13	2.93	4	5.33	7.46	10.4	14.4
Gate number	**13**	**14**	**15**	**16**	**17**	**18**	**19**	**20**	**21**	**22**	**23**	**24**	**25**
Width (ms)	20	20	40	60	60	120	120	180	300	360	540	780	1020

3.3 Removal of spikes

De-spiking of the signal is done for two reasons. The first reason is that potential spikes can result in a shifted average value of a given gate. Since the spikes normally last for a fraction of a millisecond, and have an average close to zero (bipolar spikes), this problem is not so pronounced for long gates where all samples of an individual spike fall within the gate. However, for short gates consisting of a few samples, only parts of the spike might fall within the gate and thus the spike has a large effect on the average value. The second reason for eliminating the spikes is related to the subsequent modelling of the harmonic noise, which is known to be sensitive to spikes in the data (Dalgaard *et al.* 2012).

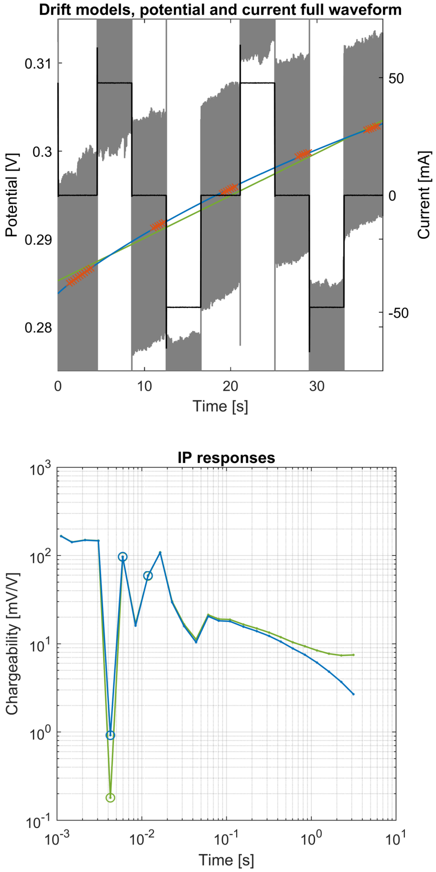

Figure 2. Top: 50 per cent duty cycle raw full-waveform potential data (grey) and transmitted current (black), subset of the signal used for finding the drift model (orange x-marker) and different types of background drift models (green: linear model and blue: Cole–Cole model). Bottom: resulting gated IP response curves (green: linear model and blue: Cole–Cole model. Negative values are marked with o-markers). Note that the resulting shapes of the IP responses are highly dependent on the used drift model at the later gates.

Before the de-spiking can be carried out, an accurate and robust method for identifying the spikes is needed. Our method uses several steps to enhance the spikes in the signal and defines a data-driven, automatic threshold to determine if a sample index (n) is to be considered as spike or not:

(1) A simple first-order high-pass filter (eq. 6) is applied on the full-waveform potential ($u_{\text{measured}}(n)$, shown in the top panel in Fig. 3) for removing signal offset and enhancing spike visibility:

$$u_2(n) = u_{\text{measured}}(n) - u_{\text{measured}}(n-1). \tag{7}$$

(2) The spikes are further enhanced by applying a non-linear energy operator, which is known to give a good estimate of signal energy content (Kaiser 1990; Mukhopadhyay & Ray 1998) on the output from step 1 (u_2, mid panel in Fig. 3) and by taking the absolute value (eq. 7):

$$u_3(n) = abs\left(u_2(n)^2 - u_2(n-1)\, u_2(n+1)\right). \tag{8}$$

(3) The signal u_3 (black line, lower panel in Fig. 3) is downsampled by taking the maximum value within 20 ms segments.

(4) A Hampel filter (Davies & Gather 1993; Pearson 2002) is applied on the output from step 3. The Hampel filter computes the median of the sample and its neighbour samples (four on each side in our examples) and estimates the STD by a mean absolute deviation. If the sample value differs more than 3 STDs from median, the sample value is replaced with the median.

(5) The output from step 4 is interpolated with linear interpolation for each sample index in u_3.

With these steps, an automatic data-driven threshold for spikes is defined, as shown in Fig. 3 (lower panel, orange curve). All the samples above the threshold are flagged as spikes (Fig. 3, orange o-marker) and are neglected when performing the harmonic de-noising procedure, thereafter the de-spiking is done based on the harmonic de-noised signal.

The de-spiking is done as a last step of the overall signal processing, after the cancelling of harmonic noise, by replacing spike-flagged sample values with the median of its eight neighbouring samples (four on each side) in the processed potential ($u_{\text{processed}} = u_{\text{measured}} - u_{\text{drift}} - u_{\text{harmonic noise}}$). The routine identifies spikes during both the on- and off-time of the current injections (Fig. 3, orange o-marker) as well as spikes originating from when the current is switched (Fig. 3). The current switch spikes, often originating from EM effects, are considered as spikes for the succeeding harmonic de-noising, but they are not included when replacing the values of the spike samples as described in previous section.

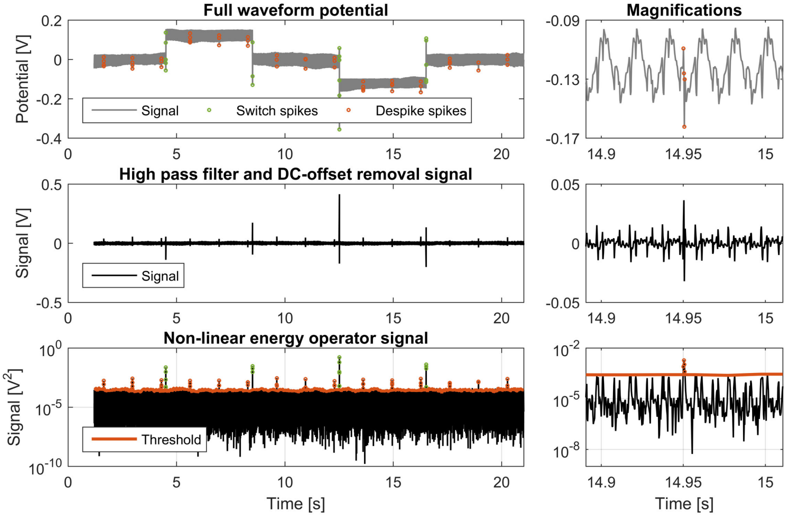

Figure 3. Top: identified spike samples of a full-waveform potential signal. Mid: output from applied high-pass and offset removal filter. Bottom: output from non-linear energy operator filter, spike samples and threshold value (bottom). Samples marked as 'switch spikes' corresponds to spikes identified at discontinuities from current switches while 'despike spikes' corresponds to other identified spikes in the signal. Magnifications of the 11th identified de-spike–spike (from 14.891 to 15.011 s) are shown on the right.

However, the current switch spike information is used in this paper for full rejection of IP gates that contains samples flagged as switch spikes.

3.4 Model-based cancelling of harmonic noise

We have adapted the approach for harmonic noise removal as presented for magnetic resonance soundings by Larsen *et al.* (2013) and seismoelectrics by Butler & Russell (1993). Typical harmonic noise originates from the power distribution grid or from AC train power distribution. The method describes the harmonic noise in terms of a sum of harmonic signals having frequencies given by a common fundamental frequency (f_0) multiplied with an integer (m) but with independent amplitudes (α_m and β_m) for each harmonic m:

$$u_{\text{harmonic noise}}(n) = \sum_m \left(\alpha_m \cos\left(2\pi m \frac{f_0}{f_s} n\right) + \beta_m \sin\left(2\pi m \frac{f_0}{f_s} n\right)\right). \tag{9}$$

By accurately determining the harmonic parameters f_0, α_m and β_m, it is possible to describe precisely the harmonic noise component of the measured potential and to subtract it from u_measured. However, the parameters f_0, α_m and β_m are not constant for the timescale (seconds to minutes depending on acquisition settings) of a TDIP measurement and the frequency can generally vary up to ±0.1 Hz in such a time frame in Nordic countries (Li *et al.* 2011). It has been shown that the fundamental frequency needs to be estimated with an accuracy of a few millihertz (Larsen *et al.* 2013). This accuracy is obtained by dividing the signal into shorter segments assuming the variation of the fundamental frequency in each segment is negligible. Butler & Russell (1993) show that the error of the harmonic parameters decreases with increasing segment length and that the best parameters are achieved when the segment length is a multiple of the period of the fundamental frequency (e.g. 20 ms multiples for $f_0 = 50$ Hz). Experience from processing several different TDIP data sets has shown that a segment length including overlap in the range of 200–300 ms is suitable for achieving good estimates and harmonic parameters, while a segment length of 220 ms with an overlap of 20 ms was used in this paper.

After segmenting the full-waveform potential, the noise model parameters are found by minimizing the residual E_residual after subtracting a temporary harmonic noise model from the drift-corrected full-waveform potential segment (ignoring identified spike samples):

$$E_\text{residual} = \sum_n \left(u_\text{measured}(n) - u_\text{drift}(n) - u_\text{harmonic noise}(n)\right)^2. \tag{10}$$

The minimum residual for each segment is determined with an iterative approach using golden section search and parabolic interpolation (Forsythe *et al.* 1977) for minimizing E_residual by changing the fundamental frequency within a given interval around the expected frequency (e.g. 50 ± 0.2 Hz). For processing efficiency, a subset of the harmonics is used for the noise model when determining fundamental frequency. This subset is chosen by taking the m_high harmonics with the highest estimated power spectral density energy (green o-marker in Fig. 4 where $m_\text{high} = 10$) compared to the baseline energy (general energy trend if ignoring the peaks). Finally, after identifying the fundamental frequency for a segment, the α_m and β_m parameters are recalculated for all harmonics up to $f_s/2$, that is, half of the sampling frequency (Fig. 5, showing α_1 and β_1).

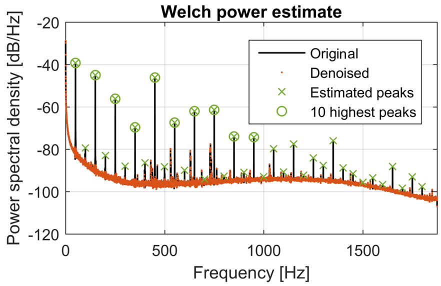

Figure 4. Welch power estimate of a full recording of potential for one quadruple: original signal (black), residual signal after noise cancellation (orange). The green markers show identified energy peaks (cross marker) and harmonics used for finding the fundamental frequency (circle marker). There is a clear reduction of the energy at 50 Hz and its harmonics after the processing and the energy level is reduced to the baseline. The remaining energy peaks represent frequencies that are not harmonics of the 50 Hz.

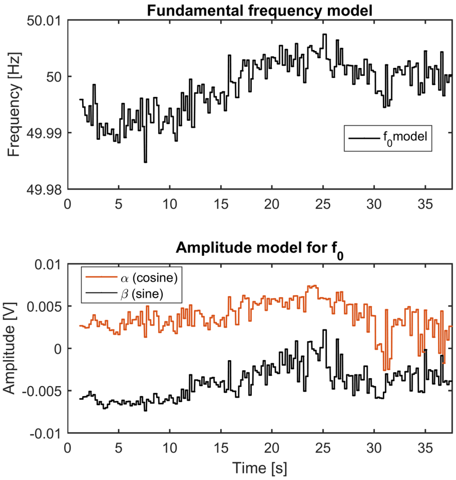

Figure 5. Top: example of parameters for a harmonic noise model, showing the model for the fundamental frequency. Bottom: amplitude models for α and β for the fundamental frequency corresponding to eq. (8) with $m = 1$.

Fig. 4 shows the Welch power spectral density estimate (Welch 1967), which gives an estimate of the signal power for different frequencies, for a full-waveform potential recording before and after applying the harmonic de-noising. The original signal (black line) exhibits distinct peaks of energy at 50 Hz and integer multiples of this frequency corresponding to the harmonics. In the corresponding energy estimate after the harmonic de-noising (orange line), the energy peaks have been reduced to the baseline energy as a result of modelling and subtracting the harmonic noise. The remaining energy peaks after harmonic de-noising (e.g. at approximately 430, 630 and 780 Hz) represent frequencies that are not harmonics of the 50 Hz.

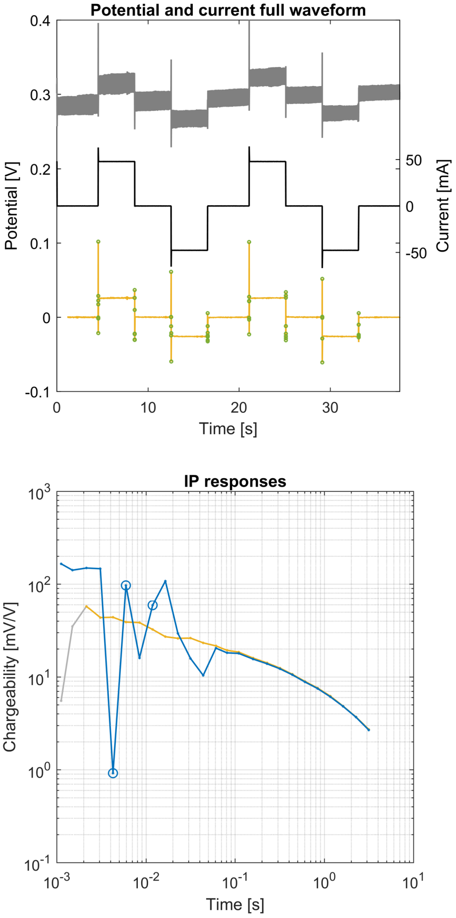

Figure 6. Top: full-waveform current (black) and potential before (grey) and after (yellow) drift removal and cancelling of harmonic noise. Switch spike samples are indicated by green o-marker. Bottom: resulting IP responses with harmonic denoising (yellow line, gates associated with indicated switch spikes are shown in grey) and without (blue line).

Fig. 6 shows the data from Fig. 2, but now corrected for Cole–Cole drift, spikes and harmonic noise according to eqs (3) and (4) ($u_{\text{processed}} = u_{\text{measured}} - u_{\text{drift}} - u_{\text{spikes}} - u_{\text{harmonic noise}}$). The resulting IP response with harmonic de-noising (Fig. 6, bottom, yellow line) shows a clear improvement compared to the IP response without the harmonic de-noising (blue line). The erratic behaviours for early gates are absent and the IP response shows a decaying shape, as it is expected for a survey on a generally homogeneous media (see Section 4). These improvements extend the first usable spectral IP information to around 2 ms after the current pulse. The first two gates (grey line) show an unexpected behaviour with increasing values also after applying the harmonic de-noising. This behaviour

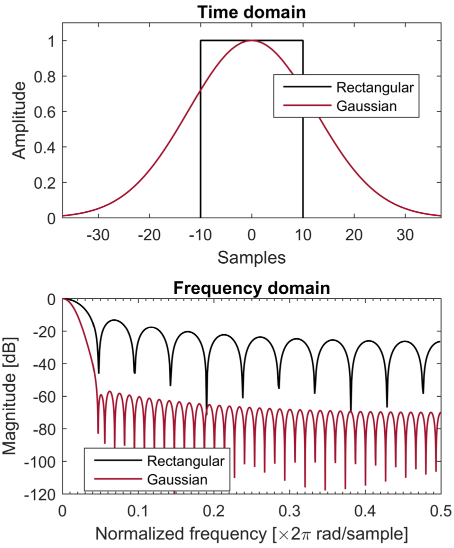

Figure 7. Time-domain (top) and frequency-domain (bottom) representations of rectangular (21 samples) and Gaussian ($N_{\text{window}} = 75$ samples and $\alpha = 3$, i.e. 3 standard deviations contained in the window) windows. Note that in frequency domain, the side lobes have Fourier transform magnitudes approximately 40 dB lower for the Gaussian window.

is due to a presence of spikes in the measured voltage (yellow line and green o-marker, Fig. 6 top) in these gates and thus these gates are rejected by the processing.

3.5 Tapered gate design and error estimation

Today, the standard procedure for gating IP is to average the data within the pre-defined IP gates, corresponding to a discrete convolution with a rectangular window. In other geophysical methods (e.g. transient EMs) different kinds of tapered windows have been used for decades for gating data (Macnae *et al*. 1984; Mccracken *et al*. 1986). One reason for using tapered window functions is that the suppression of high-frequency noise is superior in comparison with the rectangular one. Furthermore, the tapered windows allow the use of wider and overlapping gates, which have higher noise suppression, with minimal distortion of the signal. An example of this effect is seen in Fig. 7 where the filter characteristic of a rectangular window (black line) is compared with a wider (3.5 times) Gaussian window (red line) in time and frequency domains. The Gaussian window coefficients w_m for gate m are given by (Harris 1978):

$$w_m(i) = e^{-\frac{1}{2}\left(\alpha \frac{i}{(N_{\text{window}}(m)-1)/2}\right)^2};\ |i| \le \left(N_{\text{window}}(m) - 1\right)/2 \qquad (11)$$

where i is window sample index, $N_{\text{window}}(m)$ is total number of window samples for gate m and α is the number of STDs contained in the window ($\alpha = 3$ in our example, i.e. 3 STDs contained in the window).

In the frequency domain, the main lobe of both windows cuts at approximately the same normalized frequency (because of the increased width of the Gaussian window, otherwise the Gaussian window would cut at higher frequencies), but the side lobes of the Gaussian window are around 40 dB smaller. Thus, the Gaussian window is superior in reducing the high-frequency noise contribution (u_{random}) compared to the rectangular window. Consequently, we have chosen to implement the tapered gates using overlapping Gaussian-shaped windows which are 3.5 times wider than the gate widths of Table 1 ($N_{\text{window}}(m) = 3.5 * N_{\text{samples}}(m)$), but with the same centre times. However, in this study, the tapered gating is not used directly for signal estimation: a more sophisticated approach is developed for better estimating both the signal itself and its uncertainty from the data variability within the gates.

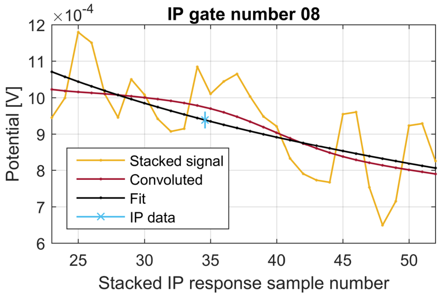

Figure 8. The different steps involved in tapered gating and error estimation for gate number 8 of the processing example. Final IP gate datum with corresponding STD estimate of the gating uncertainty is shown in light blue.

Uncertainty estimation of the data for individual IP gates cannot be retrieved by directly comparing the individual IP stacks since, for the finite number of pulses used in field surveys, each individual pulse response is different due to superposition from previous pulses (Fiandaca *et al*. 2012), hence other approaches are needed. The variability of the signal within the gates is a valuable option, and it is also desirable that the uncertainty estimate makes use of the actual window function used when gating the data. With sufficient gates per decade used for gating the data, the signal variability is almost linear within the gates and for IP signals the linearity is more evident in lin–log space (corresponding to exponential in lin–lin space), except for the presence of noise. Thus, it is possible to convolve the signal within the gates with the Gaussian windows (eq. 11) for suppressing the noise and to use the misfit of an exponential fit of the convoluted data in for estimating the gate uncertainty.

Fig. 8 shows the different steps for estimating the signal and its gating uncertainty using the eighth gate of the response of Fig. 6 as an example:

- First, the $u_{\text{IP,stacked}}$ signal is computed from the full-waveform data processed with Cole–Cole drift removal, de-spiking and harmonic de-noising according to eq. (2) (yellow line).
- After stacking, the convolution for gate number m, $u_{\text{IP,conv}(m)}$ of the stacked potential, $u_{\text{IP,stacked}}$ is determined according to eq. (11) (red line):

$$u_{\text{IP,conv}(m)}(j) = \frac{1}{w_m} \sum_{i=-\frac{N_{\text{window}}(m)-1}{2}}^{\frac{N_{\text{window}}(m)-1}{2}} u_{\text{IP,stacked}}\left(j + S_{\text{gate}}(m) - 1 - i\right) w_m(i) \qquad (12)$$

where *j* denotes sample index within the gate *m*.

- An exponential fit of convoluted signal is done in lin—lin space (denoted $u_{\mathrm{IP,fit}(m)}$, black line).
- The IP value for the gate is retrieved by evaluating the exponential fit at the log-centre time of the gate (light blue x-marker).
- Last, the gating STD on the value, $\mathrm{STD}_{\mathrm{gating}}(m)$ (light blue error bar) is computed in terms of misfit between convoluted data and exponential fit for all the gate samples ($N_{\mathrm{samples}}(m)$), as follows in eq. (12):

$$\mathrm{STD}_{\mathrm{gating}}(m) = \sqrt{\frac{1}{N_{\mathrm{samples}}(m)} \sum_{i=1}^{N_{\mathrm{samples}}(m)} \left(u_{\mathrm{IP,conv}(m)}(i) - u_{\mathrm{IP,fit}(m)}(i)\right)^2}. \tag{13}$$

This estimate gives a measure of the noise content within the gate after the convolution. In fact, whenever the noise level is low and enough gates per decade are used (i.e. normally 7–10), the misfit is negligible. Contrastingly, if random or residual harmonic noise or both are present, the misfit between the convoluted signal and the exponential fit represents a measure of the gating uncertainty. By using the convoluted gate signal for estimating the uncertainty, the measure takes into account the convolution used in the processing.

The STD computed from the data gating is not the only uncertainty estimation linked to the processing scheme presented in this study. As shown in Fig. 2, also the background drift removal can have a large impact on the resulting IP responses and the fit of the drift model gives a useful measure of the remaining drift uncertainty. Similarly to the estimation of gating uncertainty, the drift uncertainty ($\mathrm{STD}_{\mathrm{drift}}$) is estimated from the sum of misfit between drift subset data (u_{subset}, orange x-marker in Fig. 2) and Cole–Cole drift fit (u_{drift}, blue line in Fig. 2) for all drift subset data samples (N_{subset}) according to eq. (13)

$$\mathrm{STD}_{\mathrm{drift}} = \frac{1}{N_{\mathrm{subset}}} \sqrt{\sum_{i=1}^{N_{\mathrm{subset}}} \left(u_{\mathrm{subset}}(i) - u_{\mathrm{drift}}(n_{\mathrm{drift}}(i))\right)^2} \tag{14}$$

where $n_{\mathrm{drift}}(i)$ gives the global sample index *n* for drift subset data point *i*.

The total uncertainty ($\mathrm{STD}_{\mathrm{total}}$) for any IP gate is computed by summing up the gating, drift and a uniform STD according to eq. (14)

$$\mathrm{STD}_{\mathrm{total}}(m) = \sqrt{\mathrm{STD}_{\mathrm{gating}}(m)^2 + \mathrm{STD}^2_{\mathrm{drift}} + \mathrm{STD}^2_{\mathrm{uniform}}} \tag{15}$$

Finally, Fig. 9 shows the processed IP response in terms of values and relative total STDs (with 5 per cent of uniform STD) in comparison with the IP response as supplied by processing of the instrument. The STD error bars increase at early times since the shorter gates give higher $\mathrm{STD}_{\mathrm{gating}}$, while at late times the drift uncertainty increases and $\mathrm{STD}_{\mathrm{drift}}$ contributes more to the total gate $\mathrm{STD}_{\mathrm{total}}$. Note that error bars with the total error captures the fluctuations in chargeability. The two first gates are artefacts created by the potential spikes at the polarity switches of the pulses and rejected by the processing for containing switch spikes (Figs 2 and 6). Nevertheless, the first reliable gate (gate number 3) corresponds to approximately 2 ms after the current pulse, compared to 20 ms for the instrument output.

The presented processing scheme includes assumptions that are not always fulfilled in field applications. In particular, the parameters of the harmonic noise model are assumed to be constant within each segment in which the signal is subdivided and rapidly varying parameters are not entirely compensated. However, the proposed uncertainty estimation takes into account the performance of the processing scheme and ineffective harmonic de-noising or drift removal will be reflected in the data error bars.

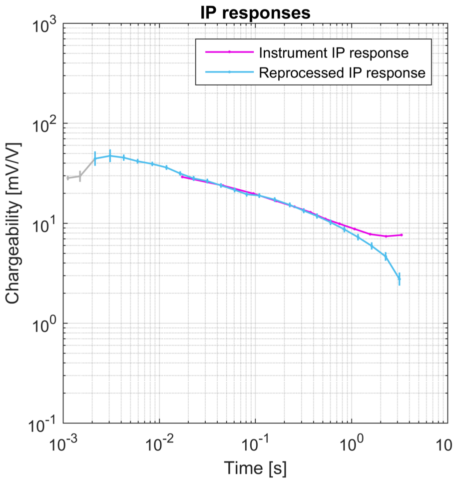

Figure 9. IP responses from instrument processing (magenta, instrument output) and from the full-processing scheme presented by this paper (light blue) with error bars corresponding to one STD (vertical lines). The first two gates are greyed out because they contain current switch spikes. In total, six new gates are retrieved by the processing at early times (almost one decade in time), thanks to the harmonic de-noising, and five gates are now usable at late times, thanks to the improved drift removal.

4 FULL-FIELD PROFILE PROCESSING EXAMPLE

Fig. 10 shows the pseudo-sections for a full data set (364 quadrupoles, multiple gradient protocol) acquired on the same profile from which the previous IP response example (except Fig. 3) was measured. It shows IP gates 3, 9, 18 and 25 from IP responses generated by the full-signal processing routine and corresponding pseudo-sections for the same gates, but only applying the linear background drift removal. For the early gates, which are not a multiple of the time period of the harmonic noise (gates 3 and 9), there is a remarkable improvement with much smoother pseudo-sections from gate 3 (centre gate time 2.2 ms) and higher. This suggests that with some minor visual inspection and manual filtering, IP data can be used already 2.2 ms after the current pulse is turned off (or changes polarity with 100 per cent duty-cycle acquisition), thus moving the first gate approximately one decade closer to the pulse compared to the traditional IP processing. Contrastingly, IP gate number 18, which is a multiple of the time period of the harmonic noise, shows very similar pseudo-sections for the two processing examples. However, the pseudo-sections for the last IP gate (25), which is known to be affected by the applied drift model, again show differences. Here, the improved processing with Cole–Cole model drift estimate shows a smoother variation in the pseudo-section, especially for the left side of the pseudo-section. In total, 23 usable gates are achieved with the processing described by this paper: compared to the instrument IP response, six gates are gained

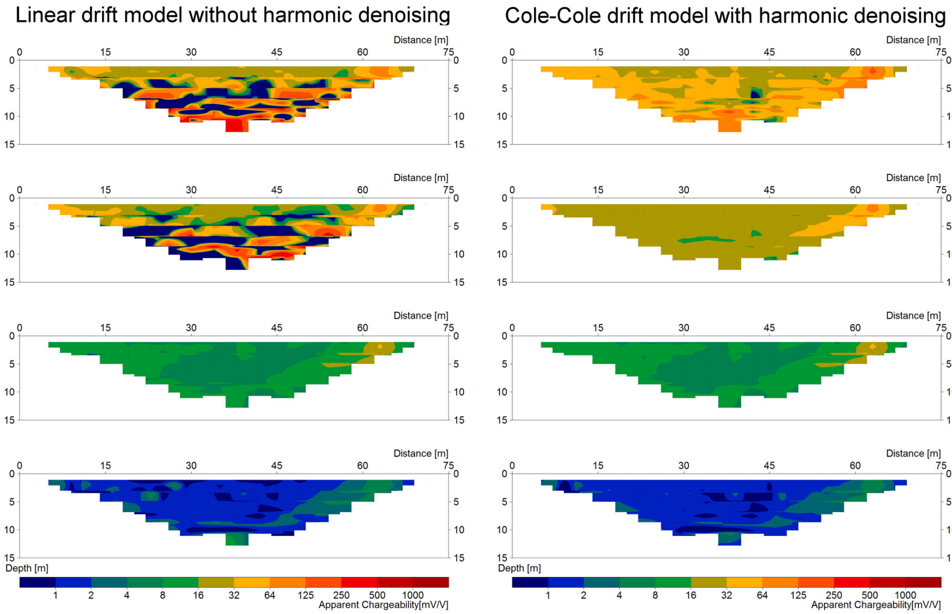

Figure 10. Pseudo-sections for IP gates 3, 9, 18 and 25 (from top to down) for processed data without harmonic de-noising and linear drift removal (left) and with harmonic de-noising and Cole–Cole drift removal (right).

at early times and five gates at late times. Altogether, the proposed processing scheme doubles the spectral content of the reprocessed response compared to the instrument processing. The results are just shown for this example profile, but have been confirmed and reproduced on several field surveys carried out in Denmark and Sweden both in urban and rural environments (e.g. Johansson *et al*. 2016).

5 CONCLUSIONS

The TDIP signal processing scheme described in this paper significantly improves the handling of background drift, spikes and harmonic noise superimposed on the potential response in the measured full-waveform potential. For cases, where electrodes are used for both transmitting and subsequently receiving, the Cole–Cole background drift removal substantially increases the accuracy of the drift model and recovers the shape of the IP response at late times with significantly reduced bias. In addition, the model-based harmonic de-noising and the data-driven de-spiking give access to early IP response times down to a few milliseconds, which are impossible to retrieve with classic IP processing. Furthermore, the overall SNR is increased by applying tapered and overlapped gates. Finally, data-driven uncertainty estimates of the individual IP gate values are retrieved.

The full-processing scheme presented by this paper has been successfully applied on different datasets from both urban and rural field sites with substantial improvements in spectral information content, data reliability and quality. The increased data reliability and the doubling of the usable range of TDIP data to almost four decades in time will significantly advance the science and the applicability of the spectral TDIP method. In particular, it is a promising development for researchers linking together lab and field measurements, and also for extending the use of the spectral TDIP method as a standard tool outside the research community.

ACKNOWLEDGEMENTS

Funding for the work was provided by Formas—The Swedish Research Council for Environment, Agricultural Sciences and Spatial Planning (ref. 2012-1931), BeFo—Swedish Rock Engineering Research Foundation (ref. 331) and SBUF—The Development Fund of the Swedish Construction Industry (ref. 12719). The project is part of the Geoinfra-TRUST framework (Transparent Underground Structure). Further support was provided by the research project GEOCON, Advancing GEOlogical, geophysical and CONtaminant monitoring technologies for contaminated site investigation (contract 1305-00004B). The funding for GEOCON is provided by The Danish Council for Strategic Research under the programme commission on sustainable energy and environment. Finally, additional funding was provided by Hakon Hansson foundation (ref. HH2015-0074) and Ernhold Lundström foundation.

REFERENCES

Abem, 2011. Terrameter LS Product Leaflet [WWW Document]. Available at: http://www.abem.se/support/downloads/technical-specifications/terrameter-ls-leaflet-20111116, last accessed 27 May 2014.

Auken, E. *et al.*, 2015. An overview of a highly versatile forward and stable inverse algorithm for airborne, ground-based and borehole electromagnetic and electric data, *Explor. Geophys.,* **46**(3), 223–235.

Butler, K.E. & Russell, R.D., 1993. Subtraction of powerline harmonics from geophysical records, *Geophysics,* **58**(6), 898–903.

Butler, K.E. & Russell, R.D., 2003. Cancellation of multiple harmonic noise series in geophysical records, *Geophysics,* **68,** 1083–1090.

Chongo, M., Christiansen, A.V., Fiandaca, G., Nyambe, I.A., Larsen, F. & Bauer-Gottwein, P., 2015. Mapping localised freshwater anomalies in the brackish paleo-lake sediments of the Machile–Zambezi Basin with transient electromagnetic sounding, geoelectrical imaging and induced polarisation, *J. appl. Geophys.,* **123**, 81–92.

Cole, K.S. & Cole, R.H., 1941. Dispersion and absorption in dielectrics: I. Alternating current characteristics, *J. Chem. Phys.,* **9**(4), 341–351.

Dahlin, T., 2000. Short note on electrode charge-up effects in DC resistivity data acquisition using multi-electrode arrays, *Geophys. Prospect.,* **48,** 181–187.

Dahlin, T., Leroux, V. & Nissen, J., 2002. Measuring techniques in induced polarisation imaging, *J. appl. Geophys.,* **50,** 279–298.

Dalgaard, E., Auken, E. & Larsen, J.J., 2012. Adaptive noise cancelling of multichannel magnetic resonance sounding signals, *Geophys. J. Int.,* **191,** 88–100.

Davies, L. & Gather, U., 1993. The Identification of Multiple Outliers, *J. Am. Stat. Assoc.,* **88,** 782–792.

Deo, R.N. & Cull, J.P., 2015. Denoising time-domain induced polarisation data using wavelet techniques, *Explor. Geophys.,* **47**(2), 108–114.

Dey, A. & Morrison, H.F., 1973. Electromagnetic coupling in frequency and time-domain induced-polarization surveys over a multilayered earth, *Geophysics,* **38,** 380–405.

Doetsch, J., Fiandaca, G., Auken, E., Christiansen, A.V. & Cahill, A.G., 2015a. Field-scale time-domain spectral induced polarization monitoring of geochemical changes induced by injected CO_2 in a shallow aquifer, *Geophysics,* **80**(2), WA113–WA126.

Doetsch, J., Ingeman-Nielsen, T., Christiansen, A.V., Fiandaca, G., Auken, E. & Elberling, B., 2015b. Direct current (DC) resistivity and induced polarization (IP) monitoring of active layer dynamics at high temporal resolution, *Cold Reg. Sci. Technol.,* **119,** 16–28.

Fiandaca, G., Auken, E., Christiansen, A.V. & Gazoty, A., 2012. Time-domain-induced polarization: full-decay forward modeling and 1D laterally constrained inversion of Cole-Cole parameters, *Geophysics,* **77,** E213–E225.

Fiandaca, G., Doetsch, J., Vignoli, G. & Auken, E., 2015. Generalized focusing of time-lapse changes with applications to direct current and time-domain induced polarization inversions, *Geophys. J. Int.,* **203,** 1101–1112.

Fiandaca, G., Ramm, J., Binley, A., Gazoty, A., Christiansen, A.V. & Auken, E., 2013. Resolving spectral information from time domain induced polarization data through 2-D inversion, *Geophys. J. Int.,* **192,** 631–646.

Forsythe, G.E., Malcolm, M.A. & Moler, C.B., 1977. *Computer Methods for Mathematical Computations,* Prentice-Hall.

Gazoty, A., Fiandaca, G., Pedersen, J., Auken, E., Christiansen, A.V. & Pedersen, J.K., 2012a. Application of time domain induced polarization to the mapping of lithotypes in a landfill site, *Hydrol. Earth Syst. Sci.,* **16,** 1793–1804.

Gazoty, A., Fiandaca, G., Pedersen, J., Auken, E. & Christiansen, A.V., 2012b. Mapping of landfills using time-domain spectral induced polarization data: the Eskelund case study, *Near Surf. Geophys.,* **10,** 575–586.

Gazoty, A., Fiandaca, G., Pedersen, J., Auken, E. & Christiansen, A.V., 2013. Data repeatability and acquisition techniques for time-domain spectral induced polarization, *Near Surf. Geophys.,* **11**(4), 391–406.

Harris, F.J., 1978. On the use of windows for harmonic analysis with the discrete Fourier transform, *Proc. IEEE,* **66,** 51–83.

Hönig, M. & Tezkan, B., 2007. 1D and 2D Cole-Cole-inversion of time-domain induced-polarization data, *Geophys. Prospect.,* **55,** 117–133.

Johnson, I.M., 1984. Spectral induced polarization parameters as determined through time-domain measurements, *Geophysics,* **49,** 1993–2003.

Johansson, S., Fiandaca, G. & Dahlin, T., 2015. Influence of non-aqueous phase liquid configuration on induced polarization parameters: conceptual models applied to a time-domain field case study, *J. appl. Geophys.,* **123,** 295–309.

Johansson, S., Sparrenbom, C., Fiandaca, G., Lindskog, A., Olsson, P.-I., Dahlin, T. & Rosqvist, H., 2016. Investigations of a Cretaceous limestone with spectral induced polarization and scanning electron microscopy, *Geophys. J. Int.,* submitted.

Kaiser, J.F., 1990. On a simple algorithm to calculate the "energy" of a signal, in *International Conference on Acoustics, Speech, and Signal Processing,* pp. 381–384, IEEE.

Larsen, J.J., Dalgaard, E. & Auken, E., 2013. Noise cancelling of MRS signals combining model-based removal of powerline harmonics and multichannel Wiener filtering, *Geophys. J. Int.,* **196,** 828–836.

Li, Z.W., Samuelsson, O. & Garcia-Valle, R., 2011. Frequency deviations and generation scheduling in the nordic system, in *2011 IEEE Trondheim PowerTech.,* pp. 1–6, doi:10.1109/PTC.2011.6019176.

Macnae, J.C., Lamontagne, Y. & West, G.F., 1984. Noise processing techniques for time-domain EM systems, *Geophysics,* **49,** 934–948.

Mccracken, K.G., Oristaglio, M.L. & Hohmann, G.W., 1986. Minimization of noise in electromagnetic exploration systems, *Geophysics,* **51,** 819–832.

Mukhopadhyay, S. & Ray, G.C., 1998. A new interpretation of nonlinear energy operator and its efficacy in spike detection, *IEEE Trans. Bio-Med. Eng.,* **45,** 180–187.

Oldenburg, D.W., 1997. Computation of Cole-Cole parameters from IP data, *Geophysics,* **62,** 436–448.

Olsson, P.-I., Dahlin, T., Fiandaca, G. & Auken, E., 2015. Measuring time-domain spectral induced polarization in the on-time: decreasing acquisition time and increasing signal-to-noise ratio, *J. appl. Geophys.,* **123,** 316–321.

Pearson, R.K., 2002. Outliers in process modeling and identification, *IEEE Trans. Contr. Syst. Technol.,* **10,** 55–63.

Pelton, W.H., Ward, S.H., Hallof, P.G., Sill, W.R. & Nelson, P.H., 1978. Mineral discrimination and removal of inductive coupling with multifrequency IP, *Geophysics,* **43,** 588–609.

Peter-Borie, M., Sirieix, C., Naudet, V. & Riss, J., 2011. Electrical resistivity monitoring with buried electrodes and cables: noise estimation with repeatability tests, *Near Surf. Geophys.,* **9,** 369–380.

Revil, A., Binley, A., Mejus, L. & Kessouri, P., 2015. Predicting permeability from the characteristic relaxation time and intrinsic formation factor of complex conductivity spectra, *Water Resour. Res.,* **51,** 6672–6700.

Routh, P.S. & Oldenburg, D.W., 2001. Electromagnetic coupling in frequency-domain induced polarization data: a method for removal, *Geophys. J. Int.,* **145,** 59–76.

Saucier, A., Marchant, M. & Chouteau, M., 2006. A fast and accurate frequency estimation method for canceling harmonic noise in geophysical records, *Geophysics,* **71,** V7–V18.

Welch, P., 1967. The use of fast Fourier transform for the estimation of power spectra: a method based on time averaging over short, modified periodograms, *IEEE Trans. Audio Electroacoust.,* **15,** 70–73.

Zonge, K.L., Wynn, J. & Urquhart, S., 2005. Resistivity, induced polarization, and complex resistivity, *Near Surf. Geophys.,* **9,** 265–300.

Paper III

Paper III is intentionally omitted from this version.

Paper IV

Paper IV is intentionally omitted from this version.

Paper V

Near Surface Geophysics, 2017, **15**, 657-667 doi: 10.3997/1873-0604.2017058

Mapping geological structures in bedrock via large-scale direct current resistivity and time-domain induced polarization tomography

Matteo Rossi[1*], Per-Ivar Olsson[1], Sara Johanson[1], Gianluca Fiandaca[2], Daniel Preis Bergdahl[3] and Torleif Dahlin[1]

[1] *Division of Engineering Geology, Lund University, Box 118, 221 00 Lund, Sweden*
[2] *HydroGeophysics Group, Department of Geoscience, Aarhus University, 8000 Aarhus, Denmark*
[3] *Department of Geology, Lund University, Box 118, 221 00 Lund, Sweden*

Received August 2017, revision accepted November 2017

ABSTRACT

An investigation of geological conditions is always a key point for planning infrastructure constructions. Bedrock surface and rock quality must be estimated carefully in the designing process of infrastructures. A large direct-current resistivity and time-domain induced-polarization survey has been performed in Dalby, Lund Municipality, southern Sweden, with the aim of mapping lithological variations in bedrock. The geology at the site is characterised by Precambrian granitic gneisses and amphibolites, which are intensely deformed, fractured, and partly weathered. In addition, there are northwest-trending Permian dolerite dykes that are less deformed.

Four 2D direct-current resistivity and time-domain induced-polarization profiles of about 1-km length have been carefully pre-processed to retrieve time-domain induced polarization responses and inverted to obtain the direct-current resistivity distribution of the subsoil and the phase of the complex conductivity using a constant-phase angle model. The joint interpretation of electrical resistivity and induced-polarization models leads to a better understanding of complex three-dimensional subsoil geometries. The results have been validated by lithological descriptions from several drillings. In addition, direct-current resistivity and time-domain induced-polarization logging has been carried out in two different boreholes, showing a good match with the results of the surface direct-current resistivity and time-domain induced-polarization profiles.

The direct-current resistivity and time-domain induced-polarization methodology proved to be a suitable technique for extensively mapping weathered zones with poor geotechnical characteristics and tectonic structures, which can lead to severe problems for infrastructure construction and/or constitute risk zones for aquifer contamination.

INTRODUCTION

Knowledge of geological conditions is needed in order to plan infrastructure construction work of, for example, building foundations or underground facilities and tunnels. The level of desired knowledge varies between projects and ranges from simple estimations of bedrock surface topography to detailed estimations of rock quality in terms of stability and hydraulic properties (CEN 2004). Identification of highly permeable zones is also critical from a groundwater resources management and environmental risk assessment point of view, as they control the behaviour of the flow system.

In order to provide spatially resolved variation of rock quality, the electrical resistivity tomography (ERT) method has been successfully employed in many field cases. During the construction of the Hallandsås Tunnel in southern Sweden, for example, the ERT profiles could predict challenging zones with highly fractured water-bearing or weathered unstable rock (Dahlin, Bjelm and Svensson 1999; Danielsen and Dahlin 2009). Similarly, fractured zones in bedrock have been detected with ERT in several other field cases, e.g., tunnel projects in Italy (Cavinato *et al.* 2006) and Norway (Ganerød *et al.* 2006; Rønning *et al*. 2014). A large-scale application of ERT to investigate bedrock geology is shown by Storz, Storz and Jacobs (2000), where the authors detected electrically conductive fault zones in the metamorphic crystalline basement.

---

[*] matteo.rossi@tg.lth.se

The induced polarization (IP) mechanism can be described as a charge-up effect, which can be measured simultaneously with direct-current (DC) resistivity in time-domain ERT surveys. Clay weathering in bedrock fractures has been shown to give rise to anomalies in IP, which makes these features distinguishable from non-weathered fractures (e.g., Marescot, Monnet and Chapellier 2008; Magnusson, Fernlund and Dahlin 2010). It is also well known that certain conductive minerals, e.g., sulphide minerals, give rise to large IP anomalies (e.g., Pelton *et al.* 1978). The combination of resistivity and IP measurements can therefore give complementary information on different physical aspects of the investigated bedrock.

A DC resistivity and time-domain induced polarization (DCIP) survey was carried out along four lines at Dalby, Lund Municipality, southern Sweden. The purpose of the survey was to map lithological variations in bedrock as part of site investigations for a planned underground facility. The site is located in the tectonic structure known as Tornquist Zone (TZ), and the bedrock at the site consists of a complex and deformed stratigraphy of mainly granitic gneiss, amphibolite, and dolerite dykes. A large quarry, located immediately north of the investigated area, gives an excellent overview of the geological conditions that can be expected.

In this study, we aim at refining the characterisation of the bedrock by integrating resistivity and IP using recently developed data acquisition, processing, and inversion techniques (Fiandaca *et al.* 2012; Olsson *et al.* 2015; Olsson *et al.* 2016). The refined subsoil characterisation can potentially lead to a better description and understanding of bedrock materials, their quality, and geometrical distribution.

GEOLOGICAL SETTING

Regional geology

The crystalline basement in southern Sweden mainly consists of granitoid rocks in the western part and metamorphosed rocks with associated mafic intrusions in the eastern part (Figure 1). The giant felsic magmatic intrusions are part of the Transscandinavian Igneous Belt (TIB) dated at ca. 1.85–1.67 Ga (Högdahl *et al.* 2004). The TIB has been subsequently deformed and metamorphosed during both compressional and extensional events. The Hallandian orogeny was a compressional event, which occurred around 1.45 Ga ago when the Baltica tectonic plate presumably collided with an unknown southern continent (e.g., Hubbard 1975; Brander and Söderlund 2009). A second orogenic event, known as the Sveconorwegian orogeny (e.g., Johansson, Lindh and Möller 1991; Wahlgren, Cruden and Stephens 1994; Möller *et al.* 2002) occurred at 1.1–0.9 Ga.

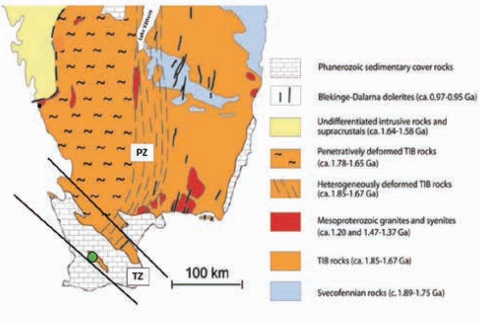

Figure 1 Simplified geological map of southern Sweden. Solid black lines delineate the northern part of the horst–graben system known as TZ. The grey dashed lines highlight the PZ. The green dot is the location of the study area in Dalby (modified from Söderlund *et al.* 2008).

The Protogine Zone (PZ) in south-central Sweden can be defined as a boundary of the deformation and metamorphism attributed to the Sveconorwegian orogeny; it is a lithological limit between the western gneisses and the almost unmetamorphosed eastern granites. The PZ is a structural zone, mainly elongated N–S, ca. 25–30 km wide, south of Lake Vättern. It is pervasively deformed with a variety of strike–parallel geological features: shear and fault zones (Wahlgren *et al.* 1994); several generations of dolerite dykes (Söderlund and Ask 2006); and mineralisation in hydrothermal systems under low-pressure conditions (Geisler and Schleicher 2000). The intrusions along the PZ have undergone various degrees of re-working and deformation.

The second prominent structural zone in southern Sweden is the horst–graben system of the TZ, a system of generally NW–SE trending faults and shear zones that cross Europe from the North Sea to the Black Sea. It has been active from ca. 300 Ma ago with alternating stages of compression and extension resulting in faulting and intrusion of fracture-parallel diabase dykes dated ca. 280 Ma (Klingspor 1976). The horsts consist of Precambrian gneisses and amphibolites, whereas in the grabens, Palaeozoic era sedimentary rocks cover the crystalline basement.

Study area

The study area is situated in the municipality of Lund (southern Sweden), southwest of the Dalby quarry (Figure 2). A geological survey at the quarry, where there is extensive exposure of the bedrock, gives a preview of the expected lithological setting in the area investigated by geophysical surveying (Figure 3).

The crystalline basement consists mainly of granitic gneiss, which can be variably weathered and fractured. The study area is located at the intersection between the PZ and the TZ and is therefore affected by at least two overlapping deformation events. The PZ in the southern part of Sweden is deformed to an NE–SW direction. A system of mafic dykes, northeast trending like PZ, has been highly deformed and metamorphosed to amphibolite grade rocks by the Sveconorwegian orogenic event. Locally, these dykes are severely weathered and altered to clay.

A second system of dykes, related to the TZ deformation, has its main trend to the northwest, parallel to the faults that create the horst–graben morphology. These diabase dykes are mainly

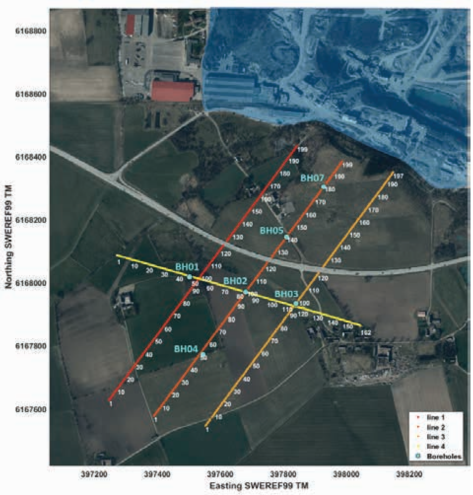

Figure 2 Location of the survey area (original orthophoto from Lantmäteriet 2015). Red to yellow lines represent the 2D layout of DCIP acquisitions. Light blue dots are the positions of the boreholes. The light blue shading marks out the location of the Dalby quarry.

sub-vertical and ca. 5–10 m thick. The basement rocks also show brittle deformation features that have been filled with mineralisation related to contact metamorphism and hydrothermal activities.

The bedrock is covered by glacial sediments (till) of a thickness of 5–25 m, here referred to as moraine deposit. The water table depth, measured in the available boreholes (Figure 2) during the year after the geophysical survey, is around 15–30 m, depending on the location and on the seasonal variation.

METHODOLOGY

The area of interest has been investigated by four 2D DCIP profiles (Figure 2): three parallel lines oriented SW–NE and a quasi-orthogonal line oriented WNW–ESE. Lines 1 and 2 are 1005 m long with 199 electrodes; Line 3 is 995 m long with 197 electrodes; and Line 4 has 167 electrodes for a total length of 805 m. The electrode spacing is 5 m, with the exception of a few areas where it was not possible to install electrodes, i.e., the two-lane road crossing the first three profiles. To overcome the discontinuity of the road, a couple of horizontal drillings were performed to be able to pass beneath the road and link cables together. A layout with two separated and parallel multi-conductor cables has been used. The two parallel cables with 10-m spacing take-outs were laterally separated by about 1–1.5 m and shifted along the line of 5 m to obtain an electrode spacing of 5 m. By using this configuration, we obtain two separate current and potential circuits, which reduces capacitive coupling in long multi-core electrode cables (Dahlin and Leroux 2012).

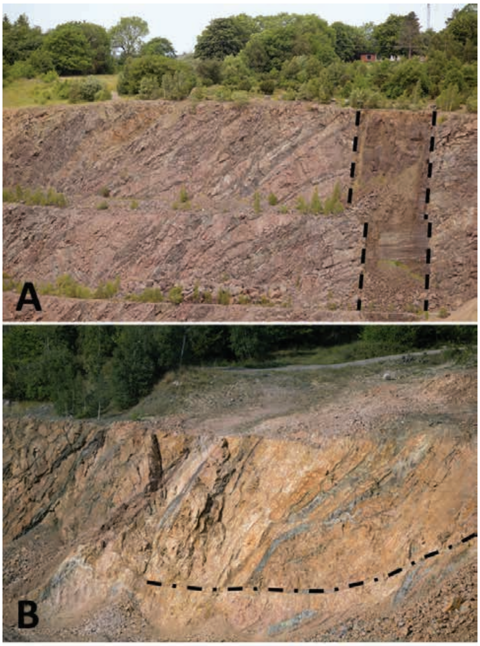

Figure 3 Examples of the crystalline bedrock from pictures taken at the Dalby Quarry. Gneiss is clearly visible in brown–red–grey colour, intensively pervaded by deformed amphibolite rocks, i.e., dark grey alignments dipping toward the left. In A, the black dashed lines mark the boundaries of a sub-vertical diabase dike, whereas in B, the dot-dashed black line highlights the presence of a brittle structure.

Data were collected with an ABEM Terrameter LS Instrument using a multiple-gradient nested array in a roll-along procedure to cover the entire length of the profiles. Each roll-along moved the lines 200 m further, with an overlapping section of 605 m with the previous acquisition. The gradient array protocol has parameter *s* in the range of 6 to 7 in the majority of the data and few added with larger *s*; whereas parameter *a* has the following values: 5, 10, 20, 40, 60, and 80 (Dahlin and Zhou 2006). Parameter *a* is the separation of the potential dipole as the number of electrodes between the measurement points, whereas parameter *s* is the distance of the current dipole, counted as a multiple of *a*.

The current injections are characterised by a 100% duty cycle, 4-second pulse length, and 3-cycle stacking waveform. Full waveforms for the transmitted current and the measured potentials were recorded at a sampling rate of 3750 Hz. The full-waveform recordings were processed as described by Olsson *et al.* (2016) to obtain reliable IP response information. This processing scheme is divided in four main steps, dealing separately with background drift, spikes, harmonic noise, and

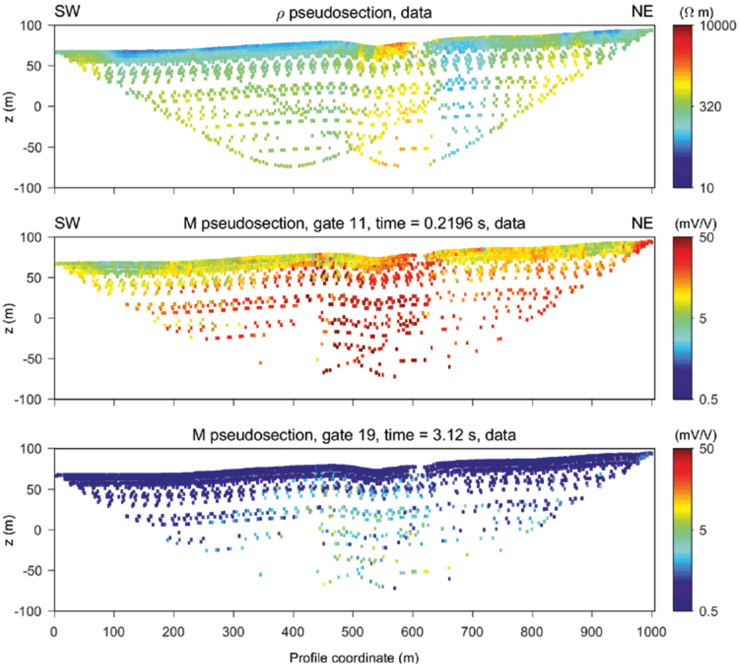

Figure 4 Example of pseudosections for Line 2: apparent resistivity data (on top) and apparent chargeability for two different time gates (at 219.6 and 3120 ms).

random noise. The first part of the processing scheme includes the removal of background potential drift. The drift is frequently present in full-waveform data as a shift of the measured electrical potentials over time, and it is mainly caused by ground self-potential and current-induced polarization of stainless-steel electrodes (Dahlin 2000). The drift often follows a Cole–Cole behaviour, and thus, this model is used for estimating and removing the background drift (Olsson *et al.* 2016). The second step involves filtering of potential spikes, usually seen in full-waveform data measured in rural environments with electrical fences for livestock management. The third processing step is the filtering of harmonic noise originating from household power supply lines (50 Hz in Sweden) and railway electrification system (16.67 Hz in Sweden), which can significantly mask part of the signal. The last step involves tapered gating of the waveform stacks into 24 time gates with logarithmically increasing gate widths, in the range from 1 to 3210 ms. This is necessary to obtain IP responses with a reduced number of samplings, starting from the full-waveform sampled at 3750 Hz, that cannot be used in the inversion procedure.

Further manual processing of resistivity and response curves was performed with the aim of removing the noisiest measurements or the noisiest time gates. The main part of the datasets shows responses from ground electromagnetic induction at earlier time gates of the response curves (from 1 to 7 ms), which can be regarded as noise when analysing IP signals. The final datasets contain between 3982 and 4045 quadripoles (89%–94% of the total amount of data), with the exception of the shorter Line 4 with 3241 quadripoles (97%). Figure 4 shows an example of a pseudosection of the raw data of Line 2 plotted as measured apparent resistivity values and apparent chargeability values of the same profile. The pseudosections show two of the 24 integrated time gates (at 219.6 and 3120 ms) to give a brief overview of the pre-processed IP response curves.

The 2D inversions (Figure 5) were carried out with the Aarhusinv software (Fiandaca *et al.* 2012) using a constant-phase angle (CPA) model (Binley *et al.* 2005), which assumes a constant phase of the complex resistivity for all frequencies. Model parameterisation is defined in terms of the DC resistivity and the phase of the complex conductivity (i.e., conductivity instead of resistivity, hence the phase is defined positive), as described in detail by Johansson, Fiandaca and Dahlin (2015). The standard deviation (STD) error of the apparent resistivity data was set to 1%, and the STD error for each IP time window was set to 10%; on top of this fixed STD error, a voltage-dependent error was added with a threshold of 0.1 mV (Olsson *et al.* 2015). The residual error of the final models, calculated as the chi statistical operator (χ), is 2.1±0.5. The simulated response curves assuming a CPA model fit the measured IP responses with small residuals. We also inverted the data using a different model with a Cole–Cole parameterisation, retrieving similar data misfit, but decided to use the simplest model that can describe the shapes of the IP response curves, which is, in this case, the CPA model.

The depth-of-investigation (DOI) computation is based on a cumulative sensitivity approach that differs from the method proposed by Oldenburg and Li (1999). The actual method is built on an approximated covariance analysis applied to the model output from the inversion while considering the data STDs (Fiandaca *et al.* 2015). The 2D inverted section is subdivided in columns where the elements of the Jacobian are summed downwards for each parameter of the model as a function of depth, and the corresponding STD factor is computed. The DOI value is then defined by imposing a threshold value of the STD factor for each parameter and each column. A DOI threshold value of 2 means that the model below the DOI is resolved within a factor of two.

Seven percussion boreholes, with relative drilling logs to a depth of 175–250 m, are present at the site, located along the

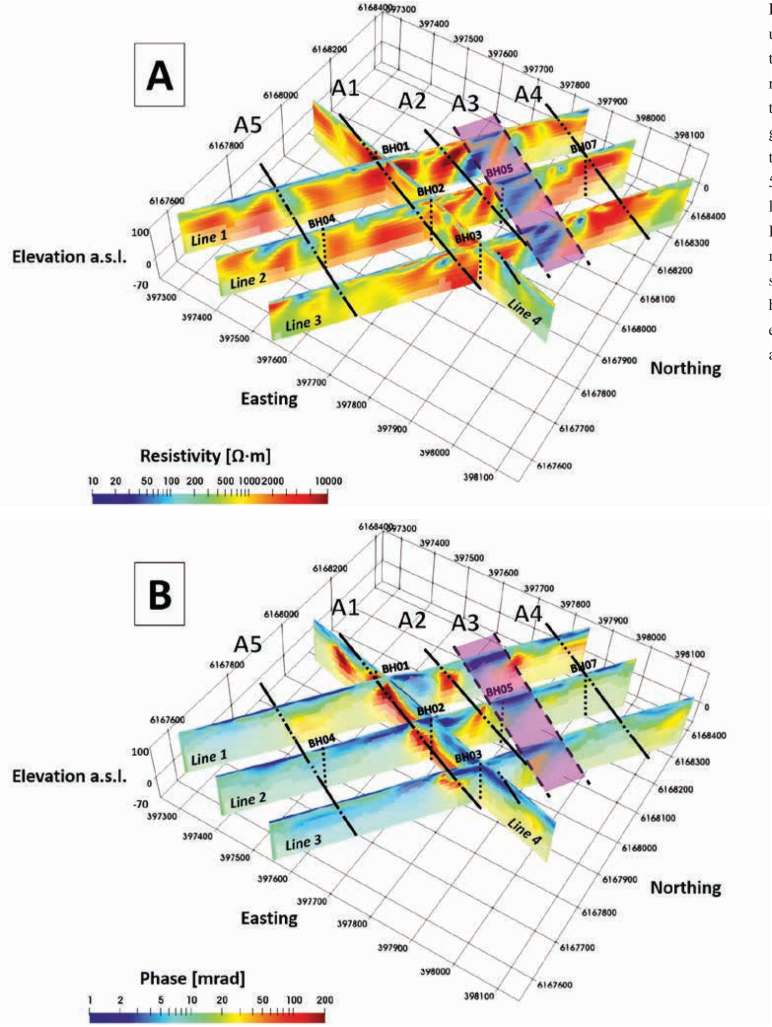

Figure 5 Three-dimensional visualisation of the inverted 2D sections. Figure A shows electrical resistivity imaging and Figure B the phase distribution. The light grey shadings represent the threshold of the DOI above 2 and 5 (respectively). Black dashed lines are the borehole positions. Black lines (A1, A2, A4, and A5) mark the presence of WNW–ESE structures. The purple area (A3) highlights a large anomaly in the electrical properties. Coordinates are Sweref99 TM (in metres).

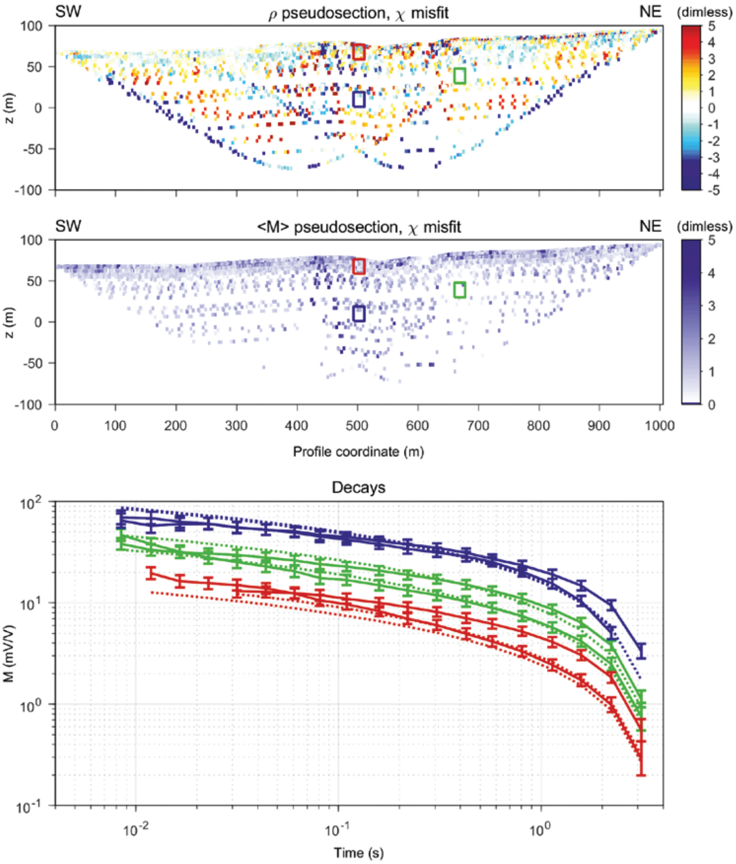

Figure 6 Example of chi misfit pseudosections for Line 2: (top) apparent resistivity and (middle) apparent chargeability. The apparent chargeability misfit is expressed in terms of summed absolute chi misfit for the full IP response. Examples of six response curves extracted from positions marked with rectangles are shown in the bottom figure; (solid lines) each different colour is the measured response after processing with STD for each gate; dashed lines are the corresponding forward models.

DCIP lines (Figure 2). The drillings took place several months after the geophysical survey; no boreholes with metal casing were present at the site during the DCIP acquisitions. The lithological description and the classification of alteration into five classes were visually estimated by the drilling company. Two boreholes, BH02 and BH05, were logged with DCIP measurements using a resistivity logging probe, i.e., a modified version of SASLOG 200, ABEM Instrument AB. As usual, the instrument acquires two standard borehole configurations, namely, short normal (SN) and long normal (LN). The modifications are the exclusion of the long lateral configuration, the addition of three different pole–dipole arrays, and the possibility to use four internal channels simultaneously to achieve time-efficient surveys. In the shallower portion of the boreholes, a metal casing has been used to prevent collapse of the sediments, and as a consequence, the logging survey has been conducted only in the deeper uncased part of the borehole.

RESULTS AND DISCUSSION

In Figure 5, the inverted DCIP profiles are plotted in a 3D view: Figure 5A represents the distribution of electrical resistivity (Ωm), whereas Figure 5B shows the phase of the complex conductivity of the CPA model (mrad). The shaded areas mask the lower reliability of the inverted electrical parameters, represented as thresholds of the DOI, fixed at 2 (low shading) and 5 (high shading). At lower values of the DOI (shallower part), the matching of the 2D profiles at the crossing points is quite consistent for both resistivity (ρ) and phase (ϕ). This aspect indicates limited 3D heterogeneity effect during the acquisition of the 2D profiles.

Figure 6 shows pseudosections of the chi misfit between modelled and measured apparent resistivity (top) and chargeability (middle) responses. In general, the apparent resistivity and chargeability misfits are low and evenly distributed throughout the pseudosection. However, at around 450 m, there are slightly increased misfits for both parameters. In addition, for the lowest pseudo-depths in the apparent resistivity misfit, the misfit is mainly negative but still within a deviation of a few percentage. Figure 6 also shows examples of response curves and their corresponding forward responses for the inversion model (bottom). There is generally a good fit between measured and modelled IP responses for the CPA parameterisation. The fact that a CPA model matches the measured data is relevant knowledge: the same out-of-phase response can be assumed for a time window from 7 to 3000 ms. It is clear that not all the response curves can be fitted with the present model even if the majority of the measured responses can be described by a forward CPA model.

The inverted resistivity has a broad range of variation from about 10 to a maximum of about 20000 Ωm (Figure 5). The most resistive areas can be identified as fresh bedrock, i.e., with a limited degree of alteration and fractures, whereas the conductive portions are related to the quaternary fluvio-glacial sediments on top and anomalies in the crystalline basement. The inversion of IP signals shows clear and well-defined transitions in the phase angle values in a broad range (1–200 mrad).

The inverted sections show a complex and heterogeneous underground. The intricate distribution of the electrical properties can be easily justified by the local geology (Figure 3), where structures and fractures can have different mineral composition, water content, and degrees of weathering. In trying to summarise the heterogeneous image of the subsoil, it is possible to recognise a trend of aligned anomalies. The presence of quasi-parallel features, delineated by a distribution of electrical properties in the WNW–ESE direction, can be recognised. The different portions of subsoil, named as A1, A2, A3, A4, and A5, can be related to structures of the TZ as they are aligned in the same direction.

Principally for two reasons, the main features of the PZ that are oriented NE–SW in the study area, almost orthogonal to TZ, are not expected to be detected. The first is that Lines 1–2–3 are in the same direction of PZ structures and a single profile (Line 4) is not sufficient to detect orthogonal 2D structures. The second reason is related to the typology of PZ features, mainly of metamorphic origin with complex geometries at a metric scale, which are portrayed as almost homogeneous at the mean resolution of the DCIP profiles (decametric scale).

Comparisons between the lithological logs from drillings and the inverted DCIP profile are shown in Figures 8 to 10. Each Figure shows the electrical properties of a DCIP profile together with the lithological logs; hence, some of the borehole descriptions are repeated in the images. The 1D distributions of electrical properties (ρ and ϕ) are extracted from the DCIP inverted profiles, exactly where the boreholes are located. Two different values of DOI are plotted as horizontal lines, both for ρ and ϕ: solid line as low DOI with threshold 5 and dashed line as high DOI with threshold 2. The DOI may help in the comparison of the results, avoiding an over-interpretation in areas where the resolution of the inverted parameters is too low. A rough lithological description obtained from the percussion drillings is plotted together with an estimation of the degree of alteration in a qualitative scale from 1 to 5 (overlapping black dashed line). As the drillings have been performed with a percussion technique, the alteration index describes both weathering and pervasive fractures.

Table 1 summarises the values of the electrical quantities that characterise the different parallel lineaments, highlighted in Figure 5. A1 and A2 are characterised by high phase angles and high resistivity values; A3 and A5 are the opposite, defined by low IP and resistivity values; and A4 shows modest phase angles and high resistivity.

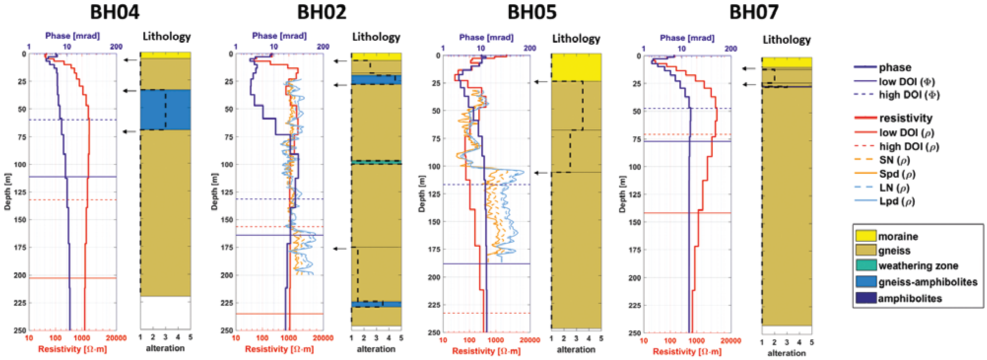

Figure 7 Borehole comparison for Line 2. Blue and red thick solid lines represent phase angle and resistivity, respectively, extracted as 1D profiles from 2D inverted DCIP tomography. Thin dashed and solid horizontal lines are the DOI depths for two different thresholds, i.e., 2 and 5, respectively. Orange and light blue lines (solid and dashed) are the results of the resistivity borehole logging. In the columns describing the lithology, a black dashed line shows the degree of alteration of the rock.

Table 1 Summary of the mean electrical properties (ϕ and ρ) of the four parallel lineaments in Figure 5.

Subsoil lineament	**Phase [mrad]**	**Resistivity [Ωm]**	**Possible interpretation**
A1	> 50	> 2000	Amphibolite
A2	> 50	> 3000	Mafic dike?
A3	< 10	< 200	Fracture zone
A4	< 10	>2000	Fresh gneiss
A5	< 10	< 200	Fracture zone

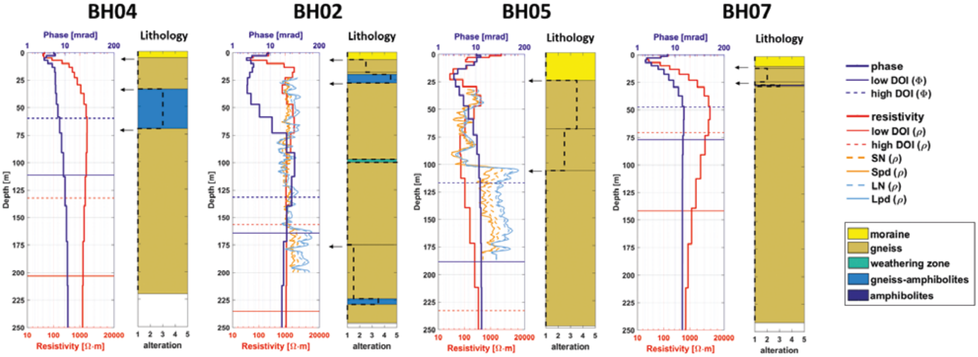

Figure 8 Borehole comparison for Line 3. See caption of Figure 7.

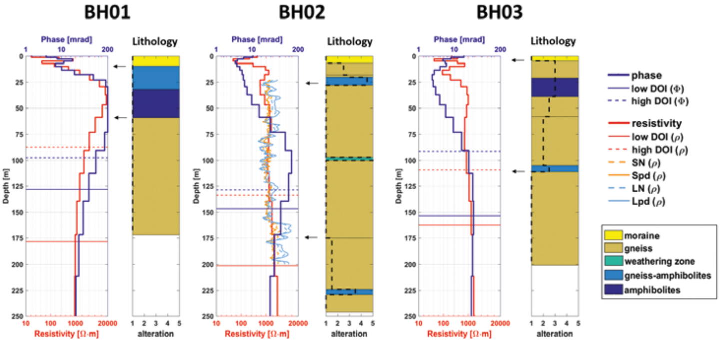

Figure 9 Borehole comparison for Line 4. See caption of Figure 7.

Anomaly A3 is characterised by a structure, i.e., 150–200 m broad from surface to the investigated depth, with deviant electrical properties: resistivity is lower than 200 Ωm and the IP response is restrained with a phase angle inferior to 10 mrad. Anomaly A5 is similar to A3 in character but narrower. The electrical properties of A3 and A5 may indicate weak zones in the bedrock. Some features linked to TZ tectonic activities, e.g., a fault or a fracture zone, may increase the secondary permeability of the basement, with the consequence of increased water content and larger specific surfaces prone to mineral alteration. An increase in clay minerals and of bulk moisture content reduces the electrical resistivity. The phase of the complex conductivity usually increases with rock alteration, except if a significant amount of interconnected clay minerals is acting as a conductor (Slater and Lesmes 2002). However, the phase can also be lowered by a larger degree of volumetric water content, as has been shown by laboratory experiments (e.g., Titov *et al.* 2004; Cassiani *et al.* 2009). Borehole BH05 has been drilled on the southern edge of A3, and the lithological log proves the presence of strongly weathered gneiss to a depth of 107 m from the topographic surface (Figure 7). Similarly, borehole BH04 has been drilled next to the northern edge of A5, and the lithological log proves the presence of strongly weathered gneiss–amphibolites from 34 to 70 m from the topographic surface (Figure 7).

The remaining linear features (A1, A2, and A4) are less univocal in the interpretation. A1 and A2 are characterised by an alignment of IP features, with a phase higher than 50 mrad. These features may represent tectonic structures such as fractures filled by hydrothermal mineralisation that can increase the IP response or mafic dikes that contain polarizable minerals with a heterogeneous alteration, leading to a non-uniform resistivity distribution. In particular, A1 is a clear lineament of very high IP response (up to 200 mrad) that crosses BH01. The lithology of BH01 suggests that high resistivity and phase are due to a thick zone of amphibolite rocks (Figure 9), likely related to the inner curvature of a fold, where usually amphibolite migrates during metamorphic processes (see example in Figure 3). A4 is characterised by high resistivity that can be explained by resistive fresh gneiss with moderate IP response, as shown in the geological logging of borehole BH07 (Figure 7).

The sediment cover shows low values of ρ and ϕ, as it is expected for moraine deposits in this geological environment. Regarding the crystalline basement, the changes in resistivity are more likely correlated with the degree of weathering of the rock, marked out in Figures 7 to 9 with black arrows.

Two boreholes are located exactly at the crossing point between DCIP lines: BH02 for Lines 2 and Line 4; BH03 for Line 3 and Line 4. The values of the extracted electrical properties are not exactly the same even if they are mainly similar above the DOI. The discrepancy can be caused by some reduced 3D effect that is not taken into account in the 2D assumption of the inversion procedure. Nevertheless, even if the values are slightly different, the 1D profiles have the same shape and trend of variation.

The presence of amphibolite is documented in two boreholes, i.e., BH01 and BH03 (Figure 9). This geological feature is linked with a high phase angle for BH01, as aforementioned, whereas a very low IP response is recorded nearby BH03. This difference can be caused by a narrower amphibolite layer in BH03 (>20 m) than the layer of rock with mafic intrusions in BH01 (about 50 m). Moreover, BH03 shows a high degree of alteration (up to class 3) that can degrade the composition of mafic minerals.

Boreholes BH02 and BH05 were logged for a resistivity profile in the saturated zone: the dashed orange line is the SN configuration; the orange solid line is a pole–dipole array with 1-m spacing between potential electrodes (Spd); the light blue dashed line is the LN configuration; and the light blue solid line is a pole–dipole array with 5-m spacing between potential electrodes (Lpd). Larger logging arrays as LN and Ldp are consistent with the resistivity profiles from surface measurements above the DOI. In particular, Ln and Lpd acquisitions along BH02 show good agreement with both Line 2 (Figure 7) and Line 4 (Figure 9). In BH05, below 100-m depth, the logging configurations with a shorter spacing (SN and Spd) show lower ρ values. This deficiency is due to a poor penetration of these arrays into the rock mass, with the consequence that the fluid resistivity of the water-filled borehole dominates the response. Care must be taken in interpreting the results of resistivity loggings aimed at lithological and rock quality descriptions since the investigated volume of rock for each electrode configuration is not known. Furthermore, in BH05 below 100-m depth, there is a mismatch between resistivity from logging and surface measurements where the surface measurements strongly underestimate the resistivity. This is likely to be an effect of reduced resolution with depth from the surface measurements (not the case for DCIP logging).

IP signals cannot be directly linked to bedrock classification as the signal can be related to different unknown parameters of the geological materials. The phase of the complex conductivity is influenced by several parameters of the rock lithology, for example, pore space geometry (Weller and Slater 2015), presence of disseminated ores (Wong 1979), degree of saturation (Ulrich and Slater 2004), and salinity (Weller *et al.* 2011). An integrated interpretation of the IP results with electrical resistivity sections and drilling logs can facilitate the classification of the subsoil and the detection of lithological features. In this work, the combined interpretation of the electrical properties leads to the detection of quasi-parallel geological structures that follow the lineaments of the TZ tectonic zone. Moreover, a clear description of the crystalline basement in terms of mineralogy, tectonic structures, and rock alteration is obtained from the adjacent quarry (Figures 2 and 3); this constrains the interpretation of the geophysical results to some reliable geological features. It must be mentioned that BH01 on Line 4 (Figure 9) shows a relatively high phase angle, up to 200 mrad, coinciding exactly with layers rich in amphibolite that contain polarizable mafic minerals.

CONCLUSIONS

We have presented a case study where DCIP methodology has been performed on a large-scale survey with four 2D profiles that cover a planar space of about 1 km × 0.8 km. The goal was to map bedrock structures and material properties that are relevant from an engineering geological as well as environmental management perspective, by integrating electrical resistivity and IP data.

The results demonstrate that DCIP data can be successfully acquired and processed on a relatively large scale relevant for standard surveying for engineering and environmental applications. The majority of the acquired data are of sufficiently good quality to allow IP inversion despite the relatively large layouts and dipole spreads. The inverted geophysical parameters are consistent between the investigated lines for the electrical resistivity and the IP model sections. The variation of geophysical quantities is also consistent with borehole information, and the results show that DCIP surveys make a useful tool for mapping geological structures and specifically structural zones in the crystalline basement. The integration of IP models is a valuable tool for delineating geological structures that sometimes can be misinterpreted by using resistivity imaging only. In the case presented here, the main features related to TZ tectonic structures, trending WNW–ESE, are identified and classified according to weathering conditions and geophysical properties.

This kind of 3D geometries is often very difficult to recognise merely using drilling techniques, which must always be complementary to geophysical surveys. Possible weak zones related to regional geological settings can be mapped by the DCIP method. This knowledge provides a basis for adequate and appropriate design for constructions. Moreover, this information can suggest risk areas from a groundwater hydraulic point of view or can point out areas where further geotechnical and/or geophysical investigations need to be carried out.

ACKNOWLEDGEMENTS

Funding that made this work possible was provided by BeFo; Swedish Rock Engineering Research Foundation (ref. 314 and 331) and SBUF, The Development Fund of the Swedish Construction Industry (ref.12718 and 12719); and Formas, The Swedish Research Council for Environment, Agricultural Sciences and Spatial Planning (ref. 2012-1931), as part of the Geoinfra-TRUST framework (*http://www.trust-geoinfra.se/*). Furthermore, funding was provided by the Danish Council for Strategic Research as part of the GEOCON project (ref. 1305-00004B). The authors would like to specially thank Skanska for funding the field survey and allowing them to publish the results, especially Benjamin Andersson and Robert Sturk. Furthermore, they would like to thank Mathias Ronczka, Cécilie Finco, Elisabeth Lindvall, and Erik Warberg for their enthusiastic efforts in the field crew. The authors are also grateful to the team from SWECO, especially Bo Bergman and Mattis Johansson, for fruitful collaboration in connection with logistical organisation and providing reference data.

REFERENCES

Binley A., Slater L.D., Fukes M. and Cassiani G. 2005. Relationship between spectral induced polarisation and hydraulic properties of saturated and unsaturated sandstone. *Water Resources Research* **41**, W12417.

Brander L. and Söderlund U. 2009. Mesoproterozoic (1.47-1.44 Ga) orogenic magmatism in Fennoscandia; Baddeleyite U-Pb dating of a suite of massif-type anorhosite in S. Sweden. *International Journal of Earth Sciences* **98**, 499–516.

Cassiani G., Kemna A., Villa A. and Zimmermann E. 2009. Spectral induced polarization for the characterization of free-phase hydrocarbon contamination of sediments with low clay content. *Near Surface Geophysics* **7**(5–6), 547–562.

Cavinato G.P., Di Luzio E., Moscatelli M., Vallone R., Averardi M., Valente A. *et al.* 2006. The new Col di Tenda tunnel between Italy and France: integrated geological investigations and geophysical prospections for preliminary studies on the Italian side. *Engineering Geology* **88**(1), 90–109.

CEN. 2004. Basis of geotechnical design. In: *Eurocode 7: Geotechnical Design—Part 1: General Rules,* Section 2, pp. 19–37. London, UK: British Standards Institution.

Dahlin T. 2000. Short note on electrode charge-up effects in DC resistivity data acquisition using multi-electrode arrays. *Geophysical Prospecting* **48**, 181–187.

Dahlin T., Bjelm L. and Svensson C. 1999. Use of electrical imaging in site investigations for a railway tunnel through the Hallandsås Horst, Sweden. *Quarterly Journal of Engineering Geology and Hydrogeology* **32**(2), 163–173.

Dahlin T. and Zhou B. 2006. Multiple-gradient array measurements for multichannel 2D resistivity imaging. *Near Surface Geophysics* **4**(2), 113–123.

Dahlin T. and Leroux V. 2012. Improvement in time-domain induced polarization data quality with multi-electrode systems by separating current and potential cables. *Near Surface Geophysics*, 545–565.

Danielsen B.E. and Dahlin T. 2009. Comparison of geoelectrical imaging and tunnel documentation. *Engineering Geology* **107**, 118–129.

Fiandaca G., Ramm J., Binley A., Gazoty A., Christiansen A.V. and Auken E. 2012. Resolving spectral information from time domain induced polarization data through 2-D inversion. *Geophysical Journal International* **192**(2), 631–646.

Fiandaca G., Ramm J., Binley A., Gazoty A., Christiansen A.V. and Auken E. 2015. Depth of investigation for multi-parameters inversions. *Proceedings of the Near Surface Geoscience 2015*, 21st European Meeting of Environmental and Engineering Geophysics, Turin, Italy.

Ganerød G.V., Rønning J.S., Dalsegg E., Elvebakk H., Holmøy K., Nilsen B. *et al.* 2006. Comparison of geophysical methods for subsurface mapping of faults and fracture zones in a section of the Viggja road tunnel, Norway. *Bulletin of Engineering Geology and the Environment* **65**(3), 231–243.

Geisler T. and Schleicher H. 2000. Composition and U–Th-total Pb model ages of polygenetic zircons from the Vånga granite, south Sweden: an electron microprobe study. *Geologiska Föreningens i Stockholm Förhandlingar (GFF)* **122**, 227–235.

Högdahl K., Andersson U.B., Eklund O. (eds) *et al.* 2004. The Transscandinavian Igneous Belt (TIB) in Sweden: a review of its character and evolution. Special Paper 37. Espoo, Finland: Geological Survey of Finland.

Hubbard F.H. 1975. The Precambrian crystalline complex of south-western Sweden. The geology and petrogenetic development of the Varberg Region. *Geologiska Föreningens i Stockholm Förhandlingar (GFF)* **97**, 223–236.

Johansson L., Lindh A. and Möller C. 1991. Late Sveconorwegian (Grenville) high-pressure granulite facies metamorphism in southwest Sweden. *Journal of Metamorphic Geology* **9**, 283–292.

Johansson S., Fiandaca G. and Dahlin T. 2015. Observed and conceptual influence of non-aqueous phase liquids on spectral induced polarization parameters. *Journal of Applied Geophysics* **123**, 295–309.

Klingspor I. 1976. Radiometric age-determinations of basalts, dolerites and related syenite in Skåne, southern Sweden. *Geologiska Föreningens i Stockholm Förhandlingar (GFF)* **98**, 195–216.

Lantmäteriet©. 2015. GSD-Ortophoto 1m raster resolution. *https://www.lantmateriet.se/*. Last access: December 2015.

Magnusson M.K., Fernlund J.M.R. and Dahlin T. 2010. Geoelectrical imaging in the interpretation of geological conditions affecting quarry operations. *Bulletin of Engineering Geology and the Environment* **69**(3), 465–486.

Marescot L., Monnet R. and Chapellier D. 2008. Resistivity and induced polarization surveys for slope instability studies in the Swiss Alps. *Engineering Geology* **98**(1–2), 18–28.

Möller A., O'Brien P.J., Kennedy A. and Kröner A. 2002. Polyphase zircon in ultrahigh-temperature granulites (Rogaland, SW Norway): constraints for Pb diffusion in Zircon. *Journal of Metamorphic Geology* **20**, 727–740.

Oldenburg D.W. and Li Y. 1999. Estimating depth of investigation in DC resistivity and IP surveys. *Geophysics* **64**, 403–416.

Olsson P.-I., Dahlin T., Fiandaca G. and Auken E. 2015. Measuring time domain spectral induced polarization in the on-time: decreasing the acquisition time and increasing the signal levels. *Journal of Applied Geophysics* **123**, 316–321.

Olsson P.-I., Fiandaca G., Juul Larsen J., Dahlin T. and Auken E. 2016. Doubling the spectrum of time-domain induced polarization by harmonic de-noising, drift correction, spike removal, tapered gating and data uncertainty estimation. *Geophysical Journal International* **207**(2), 774–784.

Pelton W.H., Ward S.H., Hallof P.G., Sill W.R. and Nelson P.H. 1978. Mineral discrimination and removal of inductive coupling with multifrequency IP. *Geophysics* **43**(3), 588–609.

Rønning J.S., Ganerød G.V., Dalsegg E. and Reiser F. 2014. Resistivity mapping as a tool for identification and characterisation of weakness zones in crystalline bedrock: definition and testing of an interpretational model. *Bulletin of Engineering Geology and the Environment* **73**, 1225–1244.

Slater L.D. and Lesmes D. 2002. IP interpretation in environmental investigations. *Geophysics* **67**(1), 77–88.

Söderlund U. and Ask R. 2006. Mesoproterozoic bimodal magmatism along the Protogine Zone, S Sweden: three magmatic pulses at 1.56, 1.22 and 1.205 Ga, and regional implications. *Geologiska Föreningens i Stockholm Förhandlingar (GFF)* **128**(4), 303–310.

Söderlund U., Karlsson C., Johansson L. and Larsson K. 2008. The Kullaberg peninsula—a glimpse of the Proterozoic evolution of SW Fennoscandia. *Geologiska Föreningens i Stockholm Förhandlingar (GFF)* **130**(1), 1–10.

Storz H., Storz W. and Jacobs F. 2000. Electrical resistivity tomography to investigate geological structures of the earth's upper crust. *Geophysical Prospecting* **48**, 455–471.

Titov K., Kemna A., Tarasov A. and Vereecken H. 2004. Induced polarization of unsaturated sands determined through time domain measurements. *Vadose Zone Journal* **3**, 1160–1168.

Ulrich C. and Slater L. 2004. Induced polarization measurements on unsaturated, unconsolidated sands. *Geophysics* **69**(3), 762–771.

Wahlgren C.-H., Cruden A.R. and Stephens M.B. 1994. Kinematics of a major fan-like structure in the eastern part of the Sveconorwegianorogen, Baltic Shield, south-central Sweden. *Precambrian Research* **70**, 67–91.

Weller A., Breede K., Slater L. and Nordsiek S. 2011. Effect of changing water salinity on complex conductivity spectra of sandstones. *Geophysics* **76**(5), F315–F327.

Weller A. and Slater L. 2015. Induced polarization dependence on pore space geometry: Empirical observations and mechanistic predictions. *Journal of Applied Geophysics* **123**, 310–315.

Wong J. 1979. An electrochemical model of the induced-polarization phenomenon in disseminated sulfide ores. *Geophysics* **44**(7), 1245–1265.

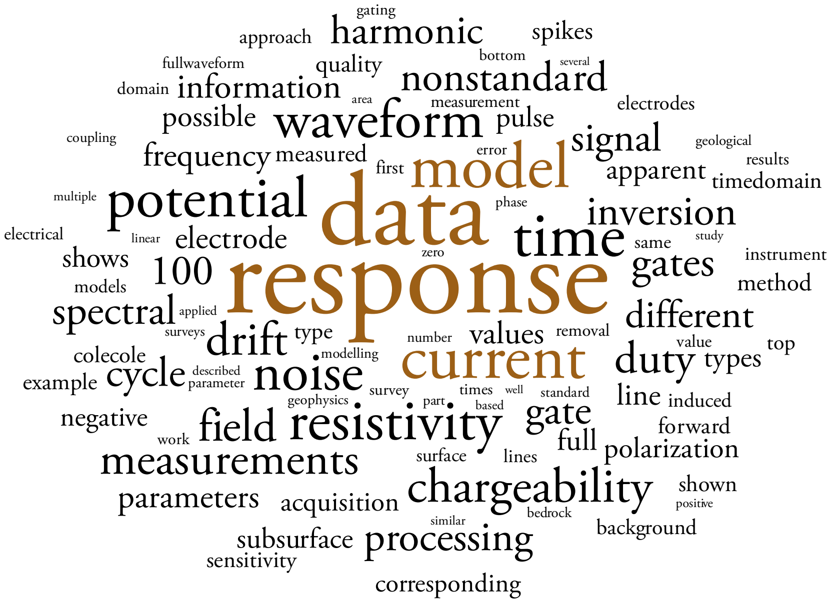

LUND UNIVERSITY

Faculty of Engineering
Engineering Geology

ISBN 978-91-7753-850-9
ISRN LUTVDG/(TVTG-1041)/1-167/(2018)

Printed by Media-Tryck, Lund 2018 NORDIC SWAN ECOLABEL 3041 0903